Parametric studies of breeding blanket thickness of a HELIAS stellarator using Monte Carlo neutron transport code Serpent2

Master's Thesis, 31.1.2023

Author:

Tommi Lyytinen

Supervisor:

Taneli Kalvas
Antti Snicker (Aalto University)

UNIVERSITY OF JYVÄSKYLÄ
DEPARTMENT OF PHYSICS

Abstract

Lyytinen, Tommi
Parametric studies of breeding blanket thickness of a HELIAS stellarator using Monte Carlo neutron transport code Serpent2
Master's thesis
Department of Physics, University of Jyväskylä, 2023, 97 pages.

This thesis presents tritium breeding and neutron flux calculations for a HELIAS reactor using Serpent2 Monte Carlo particle transport code. It is shown that complex HELIAS geometries including non-planar magnetic field coils can be directly imported from CAD to Serpent2 using STL file format. 72° and 360° CAD models of HELIAS generated by the parametric HeliasGeom tool have been benchmarked with the corresponding constructive solid geometry (CSG) models simulated with MCNP6 code. Moreover, a parametric study of the tritium breeding ratio (TBR) and neutron shielding of the coils has been carried out by varying the thickness of the breeding blanket. The neutron flux benchmark resulted an average absolute relative neutron flux difference of less than 1 % in 1.6×10^4 geometry cells. The TBR target 1.15 was achieved with constant breeding zone (BZ) thicknesses of 45 cm and 26 cm using homogenized material compositions of dual-coolant lithium lead (DCLL) and helium-cooled pebble ped (HCPB) breeding blankets. The material composition of DCLL was found to have better neutron shielding of the coils, since the fast neutron flux was below the limit 1×10^9 1/cm^{2}s in all coils using a blanket configuration BZ = 50 cm and BSS = 42.5 cm.

Keywords: Neutronics, HELIAS, Serpent, Parametric modeling

Tiivistelmä

Lyytinen, Tommi
Parametriset tutkimukset HELIAS-stellaraattorin hyötökerroksen paksuudesta Monte Carlo neutronien kuljetuskoodilla Serpent2
Pro gradu -tutkielma
Fysiikan laitos, Jyväskylän yliopisto, 2023, 97 sivua

Tässä tutkielmassa esitetään tritiumin hyötö- ja neutronivuolaskelmat HELIAS-reaktorille käyttäen Serpent2 Monte Carlo hiukkasten kuljetuskoodia. Osoitetaan, että monimutkaisia HELIAS geometrioita, jotka sisältävät ei-tasomaiset magneettikenttäkelat voidaan tuoda suoraan CAD:sta Serpent2-koodiin käyttäen STL-formaattia. HELIAS-reaktorin 72° ja 360° CAD mallit on luotu käyttäen parametrista HeliasGeom-työkalua, joille on suoritettu vertailuanalyysi vastaavien MCNP6-koodilla simuloitujen konstruktiivisten kiinteän kappaleen geometriamallien kanssa (engl. constructive solid geometry, CSG). Lisäksi, tritium hyötösuhdetta (TBR) ja kelojen neutronisuojausta on tutkittu parametrisesti vaihtelemalla hyötökerroksen paksuutta. Neutronivuon vertailuanalyysi johti keskimääräiseen vuon suhteelliseen poikkeamaan, joka oli alle 1 % 1.6×10^4 geometriasolussa. TBR-tavoite 1.15 saavutettiin vakioilla hyötökerroksen paksuuksilla 45 cm ja 28 cm käyttäen homogeenisia DCLL (DCLL, engl. dual-coolant lithium lead) ja HCPB (HCPB, engl. helium-cooled pebble ped) hyötökerrosmallien materiaalikoostomuksia. DCLL-mallilla havaittiin olevan parempi kelojen neutronisuojaus, sillä nopea vuo oli alle rajan 1×10^9 1/cm^{2}s kaikissa keloissa hyökerroksen ja sen takatukirakenteen paksuuksilla 50 cm ja 42.5 cm.

Avainsanat: Neutroniikka, HELIAS, Serpent, Parametrinen mallintaminen

Preface

This work was carried out in the Fusion and Plasma physics group of Aalto University during 2022. However, the foundation for this work was already built in the research internship in 2021 in the same group. The biggest thanks goes to my immediate supervisor Antti Snicker from Aalto, who offered the opportunity to continue the work as a thesis project. He was not only a great help in this project, as he taught me many other important skills of a researcher by his own example. I also want to thank my supervisor Taneli Kalvas from University of Jyväskylä for providing important perspectives for the thesis at different stages of the project. Moreover, Simppa Äkäslompolo and Lucia Sanchis from Aalto helped me a lot with simulations especially in the early stage. This project also required cooperation between different institutes and universities from abroad. Big thanks to Iole Palermo from CIEMAT, Javier Alguacil et al. from UNED for carrying out the benchmark calculations with MCNP, and Felix Warmer from TU/e for being supportive and providing the platform for this whole project. All in all, this project has been the first step for me in research carried out as an international collaboration, in which it has been a pleasure to be involved.

Jyväskylä January 31, 2023

Tommi Lyytinen

Contents

1 Introduction

Thermonuclear fusion is a process in which two light nuclei are brought together to form a heavier nucleus. This happens as the nuclei are heated to kinetic energies high enough to overcome their repulsive electrostatic potential. With the help of quantum mechanical tunneling, the nuclei reach the binding potential of the strong interaction and fuse into a heavier nucleus. The resulting nucleus has slightly less mass than the fusing nuclei, so energy is released in the process. The isotopes of hydrogen, deuterium (D) and tritium (T) are planned to be used as fuel in future fusion power plants. DT fusion produces a 3.5 MeV alpha particle together with a 14.1 MeV neutron. The optimal conditions to reach a burning DT plasma is achieved by heating the plasma up to 100 million degrees [1], at which point the ions are ionized and the neutral gas turns into ionized gas, i.e. plasma. Moreover, to obtain this burning fusion plasma, the density, temperature, and confinement time of the fusion triple product must exceed the Lawson criterion [1]. This leads to different confinement approaches to meet the criterion by the triple product.

The two main approaches to confine the plasma are magnetic and inertial confinement. Magnetic confinement fusion is the more advanced of the approaches, where tokamaks and stellarators are the main reactor concepts. A tokamak uses extrenal field coils and induced plasma current to create a helical total field with a component in toroidal and poloidal directions. However, because of the induction principle, the tokamak operation is pulsed in nature. Moreover, the plasma current itself drives instabilities that can perturb the plasma confinement. A stellarator is an alternative reactor concept that does not apply the plasma current. The total field is created only by magnetic field coils, which allows steady-state reactor operation. Therefore, the stellarator avoids by design both the current-driven instabilities and the challenges brought by the pulsed operation. However, at the same time other challenges arise. The plasma configuration changes from two-dimensional to three-dimensional. A more complex coil system is needed to generate the confining magnetic field, which brings several engineering challenges to the reactor design.

Despite the fact that the plasma is confined by magnetic fields, neutrons from fusion reactions can easily escape from the plasma as uncharged particles. Neutrons have 80 % of the fusion energy. The aim is to transfer their kinetic energy to a coolant in the blanket system. The heat of the coolant can be then utilized for electricity production. The blanket system surrounds the plasma and is integrated into the first wall (FW), where it also acts as a shield, reducing the heat and neutron loads to the surrounding structures. Moreover, the blanket and neutrons play a very important role in the breeding of tritium. Deuterium is an abundant isotope of hydrogen that can be extracted from seawater. In turn, tritium is radioactive and it has a very low natural abundance on Earth. Therefore, tritium is planned to be made by breeding reactions in the breeding blanket (BB) layer, where a lithium nucleus absorbs the incident neutron producing a new tritium together with an alpha particle. The new tritium can then be fed back to the plasma to cause new fusion reactions. A tritium self-sufficiency is achieved when more tritium is produced in the breeding blanket than is consumed in the plasma. This can be quantified by the tritium breeding ratio (TBR), which is the tritium production rate divided by the neutron source rate, i.e. the number of tritium ions produced on average per one fusion neutron. The current minimum TBR target is 1.15 [2] which covers the uncertainty factors related to the calculations, as well as the needs of the actual power plant tritium cycle.

In this thesis, neutrons are modeled for a HELIAS reactor design (Helical-Axis Advanced Stellarator). The HELIAS has an optimized magnetic field configuration for magnetohydrodynamic stability, to minimize pressure-driven currents and fast-ion losses. HELIAS 5-B is a specific next generation HELIAS design on its way to a realistic candidate as a fusion demonstration power plant (DEMO). The current development of the DEMO is more focused on the advanced tokamak concept but the HELIAS is being developed in parallel. In the DEMO, electricity production using DT fusion can only be demonstrated if tritium can be successfully bred in the blanket. To achieve this, extensive simulations, together with experimental validation, are necessary to gain trust that tritium self-sufficiency can be achieved. In addition to the challenge of tritium breeding, the limited space between the HELIAS plasma and field coils poses the risk of excessive neutron loading on the field coils. To this end, neutron flux calculations are essential to evaluate the design in order to meet sufficient neutron shielding and maintain the integrity of the field coils.

In this work, tritium breeding ratio and neutron flux are calculated with Serpent2 [3] which is a 3D Monte Carlo particle transport code developed by VTT Technical

Research Center of Finland. The neutron flux is benchmarked against Monte Carlo N-particle Transport Code (MCNP6) [4] calculations. MCNP is a well-validated Monte Carlo code whose development began at Los Alamos National Laboratory in the 1940s. It has been a widely used code in the field of fusion neutronics. However, new codes have entered the field. Serpent has an active development and community. Moreover, Serpent2 has the capability to include CAD models directly as triangle mesh geometry (STL file format). This is useful in fusion neutronics, where the implementation of complex reactor geometries with additional conversion tools can slow down the modeling and development process.

Fusion research has been carried out for more than 50 years. Initial ideas about magnetic confinement fusion concepts tokamak [5] and stellarator [6] were presented in the 1950s. The tokamak concept was invented in the Soviet Union by Andrei D. Sakharov and Igor E. Tamm and stellarator in the United States at Princeton University by Lyman Spitzer. Over the years, research has spread widely to Europe and Asia as well. Several large reactor facilities have been built and are currently being built. A great example of current projects is the ITER (latin translation "the way"), where the world's largest fusion reactor is built with the help of several different nations. In addition, recently several private fusion endeavors have arisen across the globe with the goal to achieve industrial-level (thermonuclear) fusion using a multitude of approaches.

Fusion energy is one of the possible solutions to climate change alongside renewable energy. Fusion fuel is also very abundant, and its resources are evenly distributed on Earth. As an advantage over renewables, fusion fuel has a higher energy density, and the fusion energy provides stable power production. Therefore, it is particularly useful in large urban industrial areas. Furthermore, compared to current nuclear fission energy, fusion does not have similar challenges with respect to safety and high level radioactive waste. However, fusion still has several technical issues to be solved before power plants are operated. In the past decades, fusion research has focused a lot on plasma physics and solving the confinement. At the same time, research on suitable reactor materials has grown rapidly. In this century, when we are slowly moving towards DEMO reactors and hopefully also to power plants, neutron modeling will become very central in solving problems related to neutron shielding and tritium self-sufficiency. Perhaps the biggest problem to be solved will be the integration of all the physics and engineering aspects into a functioning power plant.

2 Theoretical background

2.1 Fusion neutronics

Light nuclei can release energy by fusion reaction which is due to the fact that binding energy per nucleon increases as a function of the atomic mass up to iron. When moving to nuclei heavier than iron, energy can be released by fission which has been applied in energy production for more than 50 years. Nuclear fusion was discovered in 1919 by F.W Aston [7]. However, it took years before the first reactions were demonstrated in a laboratory. Mark Oliphant did the first successful fusion reaction experiment using deuterium nuclei in 1934 and found tritium at the same time [7]. Deuterium nuclei can fuse in the two following branches [7]:

$$ {}^{2}_{1}\mathrm{H} + {}^{2}_{1}\mathrm{H} \longrightarrow {}^{3}_{2}\mathrm{He}\,(0.82\,\mathrm{MeV}) + {}^{1}_{0}\mathrm{n}\,(2.45\,\mathrm{MeV}) \tag{1} $$

$$ {}^{2}_{1}\mathrm{H} + {}^{2}_{1}\mathrm{H} \longrightarrow {}^{3}_{1}\mathrm{H}\,(1.01\,\mathrm{MeV}) + {}^{1}_{1}\mathrm{p}\,(3.02\,\mathrm{MeV}). \tag{2} $$

The output and input nuclei of the reaction can also fuse with each other as follows:

$$ {}^{2}_{1}\mathrm{H} + {}^{3}_{1}\mathrm{H} \longrightarrow {}^{4}_{2}\mathrm{He}\,(3.52\,\mathrm{MeV}) + {}^{1}_{0}\mathrm{n}\,(14.06\,\mathrm{MeV}) \tag{3} $$

$$ {}^{2}_{1}\mathrm{H} + {}^{3}_{2}\mathrm{He} \longrightarrow {}^{4}_{2}\mathrm{He}\,(3.67\,\mathrm{MeV}) + {}^{1}_{1}\mathrm{p}\,(14.67\,\mathrm{MeV}). \tag{4} $$

The cross sections of the presented fusion reactions are shown as a function of energy in Figure 1 using the ENDF/B-VI nuclear data library [8]. Figure 1 shows that the DT fusion has the highest cross section at moderate energies (10–20 keV) [7]. Therefore, it is considered to be the most favorable reaction for future power plants. However, the high neutron energy of 14.1 MeV and the need to breed tritium are disadvantages of DT fusion. Energetic neutrons cause problems for neutron shielding and impose constraints on the materials used to avoid neutron activation. Compared to the U–235 fission reaction that releases a neutron of 2 MeV on average, the neutron from DT fusion can penetrate significantly deeper inside the materials and cause unwanted nuclear reactions that have threshold energies above 2 MeV. Examples of such reactions are neutron-induced gamma-ray production reactions with oxygen. The two dominating reactions in the incident energy region 7–10.5 MeV are:

$$ {}^{16}_{8}\mathrm{O} + {}^{1}_{0}\mathrm{n} \longrightarrow {}^{16}_{8}\mathrm{O} + {}^{1}_{0}\mathrm{n} + \gamma \tag{5} $$

$$ {}^{16}_{8}\mathrm{O} + {}^{1}_{0}\mathrm{n} \longrightarrow {}^{13}_{6}\mathrm{C} + {}^{4}_{2}\mathrm{He} + {}^{1}_{0}\mathrm{n} + \gamma, \tag{6} $$

where gamma rays between 3.09–7.12 MeV are produced [9].

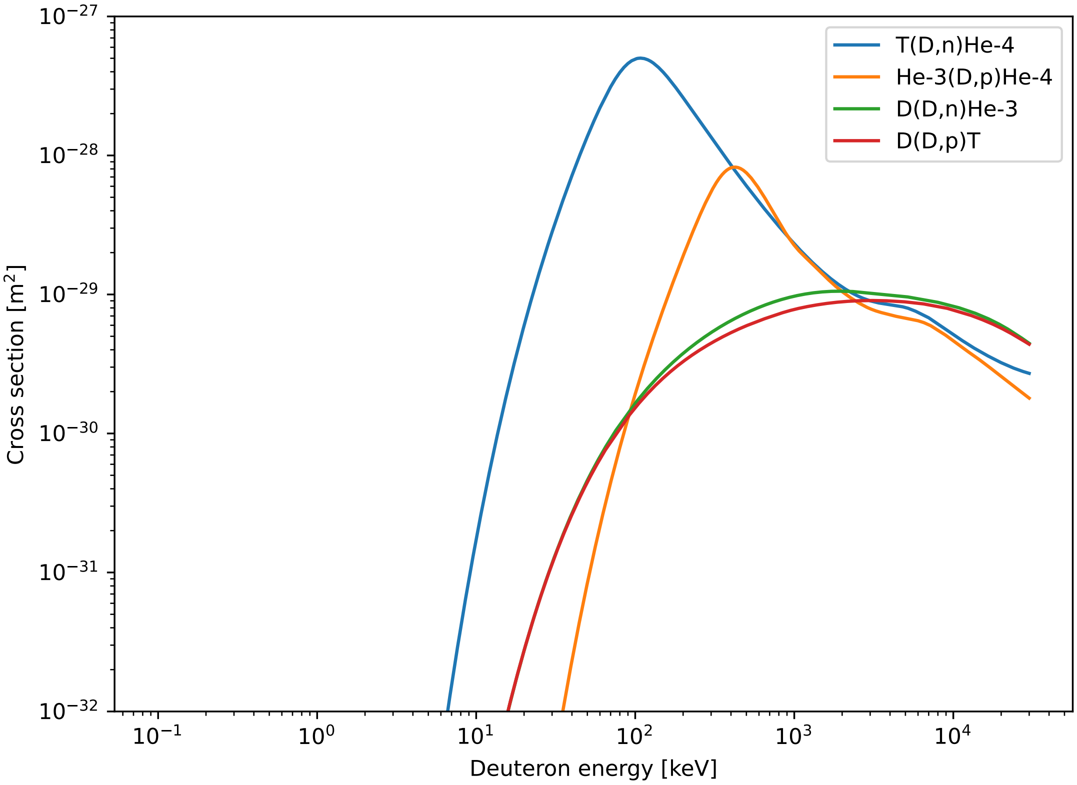

Figure 1. Cross section data of fusion reactions (1–4) shown as a function of deuteron energy.

In the DT fusion reaction, eq. 3, the neutron has 80 % of the released energy. The alpha particle has the remaining 20 % of the energy, which is used to sustain fusion reactions in the plasma. The kinetic energy of neutrons is transferred to the heat of a coolant in the blanket system surrounding the plasma. After this, the heat of the coolant can be transferred to water in the secondary circuit, as in traditional fission power plants. The vaporized water can then be directed to the turbines to generate electricity. The high thermal energy conversion efficiency of the blanket system is desired, which requires high temperature and pressure from the coolant. The thermal power conversion efficiency above 35 % can be achieved using conventional Brayton or Rankine cycles [10].

Tritium can be bred from the stable isotopes of lithium by the following two nuclear reactions:

$$
\begin{aligned}
{}^{6}_{3}\mathrm{Li} + {}^{1}_{0}\mathrm{n} &\longrightarrow {}^{3}_{1}\mathrm{H} + {}^{4}_{2}\mathrm{He} && (7)\\
{}^{7}_{3}\mathrm{Li} + {}^{1}_{0}\mathrm{n} &\longrightarrow {}^{3}_{1}\mathrm{H} + {}^{4}_{2}\mathrm{He} + {}^{1}_{0}\mathrm{n}. && (8)
\end{aligned}
$$

From the isotopes, the Li-7 is more abundant (92.41 %) than the Li-6 (7.59 %) [11], but the Li-6 has a higher reaction cross section when considering the entire energy range. The cross sections (n, Xt) of Li-6 and Li-7 are shown as a function of energy in Figure 2. These cross-sections demonstrate that the Li-7 cross section reaches zero around 3 MeV (3.1454 MeV)[8], while the Li6 cross section increases at lower energies. The energy of the neutrons is attenuated when penetrating the blanket. Moreover, tritium breeding is more effective with a higher cross section of Li-6. Therefore, Li-6 enrichment is required for the lithium composition of BB to absorb neutrons at lower energies. Moreover, part of the neutrons escape from the blanket system without interacting with lithium. In addition, some of the tritium is lost in the recycling process. Hence, neutron multipliers are used to produce more neutrons to overcome the deficit in tritium breeding that is caused by the neutron and tritium losses. In this way, tritium breeding can reach a self-sufficient level. Example reactions for neutron multiplication using lead and beryllium are [7]:

$$
\begin{aligned}
{}^{204}_{82}\mathrm{Pb} + {}^{1}_{0}\mathrm{n} &\longrightarrow {}^{203}_{82}\mathrm{Pb} + 2\,{}^{1}_{0}\mathrm{n} && (9)\\
{}^{9}_{4}\mathrm{Be} + {}^{1}_{0}\mathrm{n} &\longrightarrow {}^{4}_{2}\mathrm{He} + 2\,{}^{1}_{0}\mathrm{n} && (10)
\end{aligned}
$$

where two lower energy neutrons are emitted.

The self-sufficiency of tritium is evaluated by the unitless tritium breeding ratio

$$\mathrm{TBR} = \frac{\mathrm{TPR}}{\text{Source rate}}, \tag{11}$$

where TPR is the tritium production rate [1/s] and the source rate [1/s] is the rate at which the fusion reactions occur in the plasma i.e. the rate at which tritium is consumed. The source rate can be obtained from the fusion power and energy

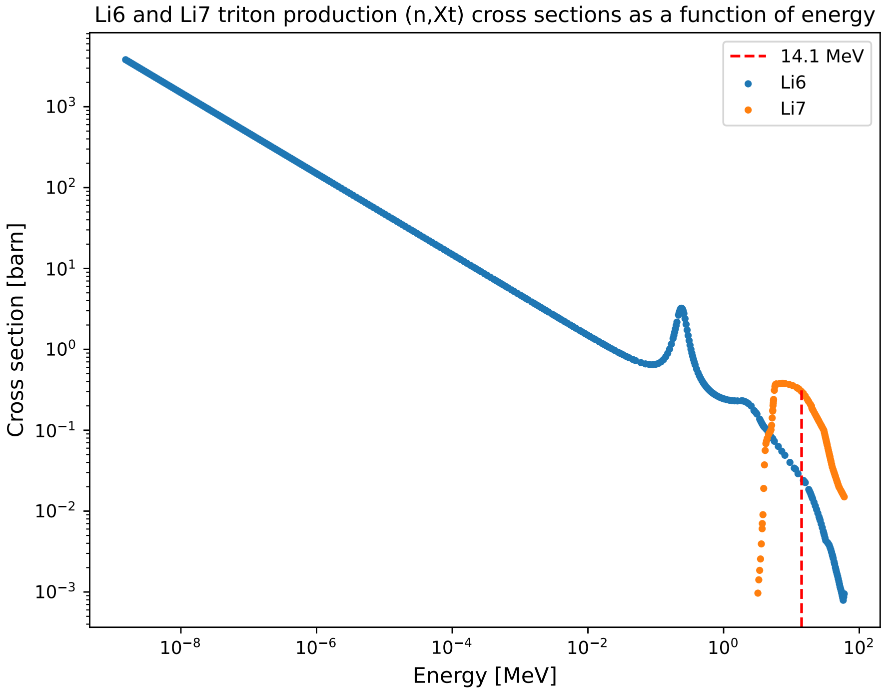

Figure 2. Li-6 and Li-7 neutron cross sections plotted from the ENDF nuclear reaction data library [8] (IRDFF-II). Li-7 cross section goes to zero with a neutron energy of 3.1454 MeV. Respectively, the Li-6 reaction cross section increases at lower energies.

released per fusion reaction

$$N_{fus} = \frac{P_{fus}}{E_{fus}} = 1.065 \times 10^{21} 1/\mathrm{s}, \tag{12}$$

where the fusion power $P_{fus} = 3000$ MW designed for the HELIAS 5-B [12] and the $E_{fus} = 17.58$ MeV is the total energy released per one DT fusion reaction. TBR ≥ 1.05 [2] is required for self-sufficiency in the fuel cycle based on the Direct Internal Recycling (DIR) concept [13]. It takes into account the losses of tritium in its processing and radioactive decay. In addition, a small surplus is required for interruptions in operation and follow-up power plants. However, TBR design target is set to ≥ 1.15 [2] for the European DEMO where uncertainties of the calculations and incomplete models have been taken into account.

Several blanket system candidates have been proposed for the DEMOs. Essentially, they vary in terms of coolant and breeder materials. Four candidates were selected for the Pre-Conceptual Design (PCD) phase of EU DEMO, the goal of which was to examine the different design options extensively by the year 2020. The candidates were WCLL (Water-Cooled Lithium-Lead) [14], HCPB (Helium-Cooled Pebble-Ped) [15], HCLL (Helium-Cooled Lithium-Lead) [16] and DCLL (Dual-Coolant Lithium-Lead) [17]. As the names imply, water and helium are used as coolants, while lithium-lead and pebble-ped describe the breeder materials. In the LiPb concepts, the breeder material is in liquid form. In contrast, the HCPB is a solid breeder concept, where the breeder material and neutron multiplier are both in form of pebble beds. The breeder material of the HCPB is ceramic Li_4SiO_4 and beryllium is used as neutron multiplier instead of lead. The DCLL concept differs from others in that liquid breeder material (LiPb) is also used as a coolant in the breeder zone. In other concepts, the cooling is performed entirely with water or helium. However, the cooling of the first wall and the stiffening grid is carried out with helium in the DCLL as well.

A schematic illustration of the DCLL blanket unit is shown in Figure 3. It consists of first wall (FW), breeding zone (BZ) including PbLi channels, and back-supporting structure (BSS) including channels for helium as well as the inlets and outlets for circulating PbLi. The structural designs of the other blanket candidates are presented in ref. [18]. The FW is plasma facing component of the blanket that must withstand high heat and particle loads. Tungsten is one of the main materials proposed for the armor of the FW. In addition, a martensitic steel called EUROFER has been developed with a reduced neutron activation for the structural material of the blanket system.

After the PCD phase, the new strategy has been to focus on the two most promising blanket candidates. WCLL and HCPB have been selected for further development for the EU DEMO, which are going to be tested in the ITER test blanket modules [19]. However, other candidates, such as the DCLL, are still being developed with limited activity as long-term approaches. A benefit in choosing the HCPB and WCLL candidates is that they represent both solid and liquid breeder concepts, as well as helium and water coolants. As a result, it is likely that a functioning blanket can be built with the strengths of at least one of the two candidates.

Neutron interactions with materials are predominantly based on neutron-nucleus interactions. Complex energy dependence especially at high energies is a characteristic of neutron interactions. The probability of interaction can vary greatly within short

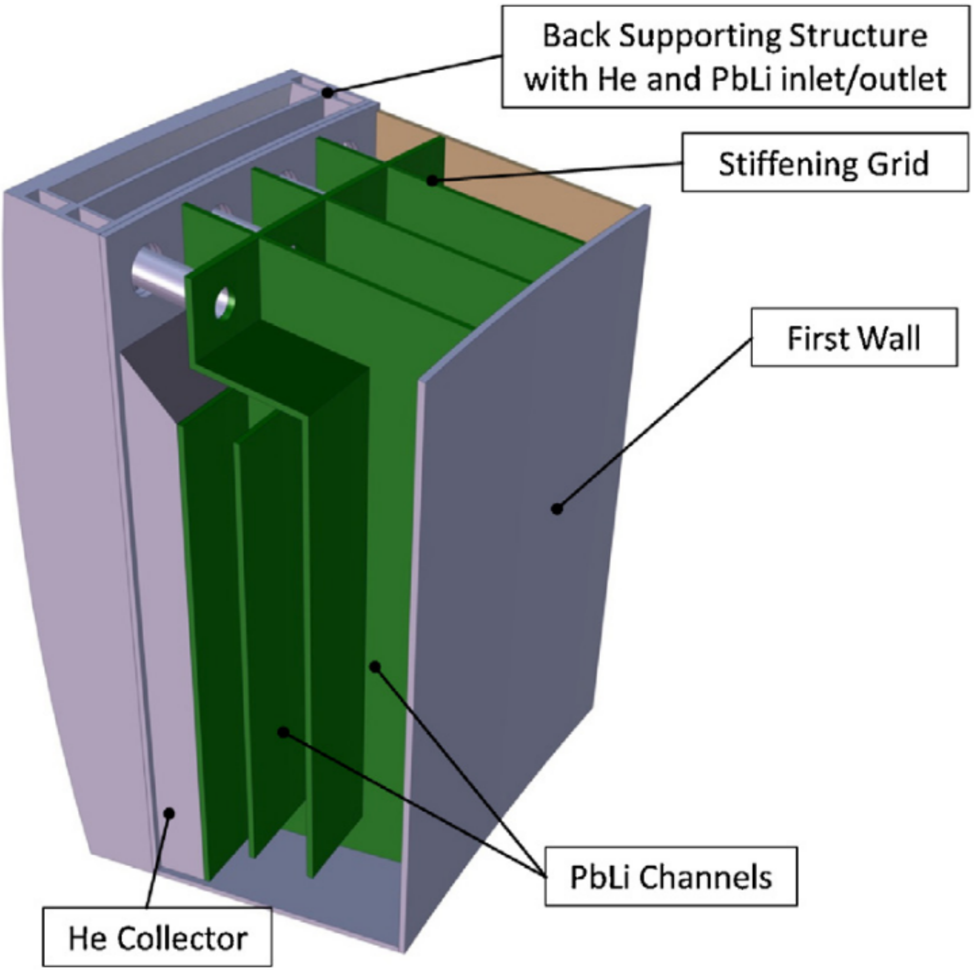

Figure 3. Schematic illustration of the DCLL blanket unit [18].

energy intervals, which can be seen as resonance peaks in cross-section spectra. At lower energies, the interaction probability is proportional to the neutron's time in the nuclear potential. As a result, the interaction probability is proportional to the inverse of the neutron speed. This property of neutron interactions is seen in tritium breeding reaction cross sections in Figure 2.

Neutron interactions with material nuclei can be divided to absorption and scattering reactions. In scattering reactions, one or more secondary neutrons are emitted with a new angle and energy after interacting with a nucleus. The momentum and kinetic energy of the system are conserved in elastic scattering. It is a two-body interaction, where the scattering angle and energy are coupled. In inelastic scattering, part of the kinetic energy is transferred to the internal energy of the nucleus. In this case, the incident neutron penetrates inside the target nucleus to interact with nucleons. The excited compound nucleus is formed, which can decay by emitting neutrons and γ-rays. In neutron absorption, the incident neutron can be captured, or it can induce fission. The incident neutron is lost, and the excited compound nucleus is formed in both reaction types. In the neutron capture, secondary neutrons are not emitted. The compound state can decay by emitting γ-rays or other secondary particles e.g. alpha particles and protons. In fission, the compound state decays energetically by splitting into two similar mass nuclei. At the same time, multiple high-energy neutrons can be emitted as well.

Neutron radiation can induce radioactivity in materials. This process is called neutron activation. Moreover, neutron collisions with nuclei can displace atoms from their lattice sites. This causes changes in the microstructure of materials that can result in degradation of material performance. The activation of materials and the deterioration of their performance are problems in fusion reactors. Therefore, it is important to model neutrons and neutron-induced reactions in detail to minimize radiation damage and exposure to materials. By minimizing the material damage, the long operating life time of components and reactor can be ensured. In addition, by avoiding the activation of the materials, the amount of radioactive waste can be minimized, which in turn improves financial competitiveness of DT fusion.

The interaction probability of a neutron is described by microscopic and macroscopic cross sections, which are energy-dependent quantities. The microscopic cross section describes the effective area of a target nucleus for an incident neutron. A larger effective area leads to a higher probability of interaction. In turn, the macroscopic cross section describes the interaction probability per path length traveled by the neutron. The macroscopic cross section of a nuclear reaction i is defined from the microscopic cross section

$$\sum\nolimits_i(\boldsymbol{r},E) = N(\boldsymbol{r})\sigma_i(E), \tag{13}$$

where $\sigma(E)$ is the microscopic cross section [m^2] and $N(\boldsymbol{r})$ is the atomic number density [$1/\mathrm{m}^3$] [20]. The macroscopic cross section could also have time-dependence, but it is omitted for simplicity. For a material consisting of several isotopes, the total macroscopic cross section is defined

$$\sum\nolimits_{tot,i}(\boldsymbol{r},E) = \sum_m N_m(\boldsymbol{r})\sigma_{m,i}(E). \tag{14}$$

2.2 Methods for solving neutron transport problems

There are two types of methods for solving neutron transport problems: deterministic and probabilistic Monte Carlo methods. While deterministic methods are based on solving the equations of neutron transport theory using numerical methods that discretize the continuous variables in the equations, Monte Carlo methods are based on sampling the free paths and interactions of neutrons from probability distributions. Monte Carlo results are obtained from the simulated discrete random events using statistical techniques. This is analogous to physical experiments. The full solution of the neutron transport equation (spatial, angular, and energy-dependent) is not obtained at any stage in Monte Carlo methods, which is a clear difference from deterministic methods. The general advantage of Monte Carlo methods is that complex transport problems can be solved with few approximations in the simulation geometry and interactions. However, this is typically computationally expensive since the statistical error is minimized using pure computing power.

The aim of the deterministic method is to determine the density function of neutrons by solving the neutron transport equation. The state of the neutron is described in the six-dimensional phase space $(\boldsymbol{r}, \boldsymbol{p})$ in the Cartesian coordinate system. However, the momentum is replaced by the unit direction vector and energy $(\boldsymbol{r},\hat{\boldsymbol{\Omega}}, E)$ in the neutron transport theory. The neutron population in the phase space can be described by the density functions such as the *angular neutron density* $n(\boldsymbol{r},\hat{\boldsymbol{\Omega}}, E)$ and *angular neutron flux* $\psi(\boldsymbol{r},\hat{\boldsymbol{\Omega}},E)$. For example, the angular neutron density describes the expected number of neutrons at position $\boldsymbol{r}$ with direction $\boldsymbol{\Omega}$ and energy E at time t per unit volume per unit solid angle per unit energy [n/cm^{3}sr] [7]. The balance of the neutron particle density within a differential volume element of the six-dimensional phase space is described by the time-dependent transport equation [20]:

$$\frac{1}{v}\frac{\partial}{\partial t}\psi(\boldsymbol{r},\hat{\boldsymbol{\Omega}},E) + \hat{\boldsymbol{\Omega}} \cdot \nabla\psi(\boldsymbol{r},\hat{\boldsymbol{\Omega}},E,t) + \sum\nolimits_t(\boldsymbol{r},E)\psi(\boldsymbol{r},\hat{\boldsymbol{\Omega}},E,t) = q(\boldsymbol{r},\hat{\boldsymbol{\Omega}},E,t), \tag{15}$$

where $\sum_t(\boldsymbol{r},E)$ is the total macroscopic cross-section of the medium, $q(\boldsymbol{r},\hat{\boldsymbol{\Omega}},E,t)$

is a general source term, and $\psi(\boldsymbol{r},\hat{\boldsymbol{\Omega}},E)$ is the angular neutron flux, the density function of the neutrons. The general source term consists of three parts which are the external, scattering, and fission sources. All of the terms have their own rigorous mathematical definitions that can be found in ref. [20]. There are various solution methods for the transport equation such as discrete ordinates methods and diffusion approximation methods, which are not a topic of this thesis [20]. The challenges of the solution are complex angular and energy dependencies in several terms of the transport equation that have to be discretized.

In terms of this thesis, it is more relevant to introduce the basis of Monte Carlo methods. Monte Carlo methods can be divided to analog and non-analog methods [21]. In analog methods, the simulation process is similar to the underlying physical process. Respectively, in non-analog methods, the simulation process deviates from the physical process. For example, the statistical weights of particles can be modified from unity, which can be used to improve the statistics of the simulation results. Despite the usefulness of non-analog methods, this introduction is limited to the basics of the analog methods. In general, the Monte Carlo method has its foundation in the fundamental laws of probability theory, such as the *law of large numbers* and the *central limit theorem* [22]. The law of large numbers states that the average obtained from the outcomes of the random event approaches the expected value by performing more events. In turn, the central limit theorem states that the sum of a large number of independent arbitrarily distributed random variables is itself a random variable following the normal distribution. The standard deviation of the normal distribution is proportional to $1/\sqrt{n}$, where n is the total number of random numbers. Therefore, to reduce the statistical error by a factor of two, four times more events must be performed. This describes the computational complexity of the Monte Carlo method to obtain a statistically valid result.

Solving a neutron transport problem by the Monte Carlo method can be thought of as containing at least the following four parts: 1) neutron source sampling from its probability distribution; 2) tracking of neutrons; 3) scoring (tallying), obtaining results from simulated events [7]. A neutron transport simulation begins with neutron source sampling. It consists of selecting an initial position, an emission direction, and an energy of a neutron from their appropriate probability distributions. In fusion neutronics, the initial positions of neutrons are often based on the plasma configuration and plasma physics calculations. The emission direction can be sampled from an isotropic distribution where the angle variables obey a uniform distribution. Various energy distributions are used in neutron transport in general. However, a simple monoenergetic source $E_0 = 14.1$ MeV is useful for studying DT fusion in fusion neutronics.

After the emission of a source neutron, the neutron tracking begins. The free path length of the neutron is sampled at the collision site. Then, sampling is performed to select the target nucleus from the material cell encountered and the nuclear reaction from the possible reaction channels. Depending on the sampled reaction, the neutron history may be terminated, new particles may be produced, or the incident neutron may be scattered. For the scattered neutrons, the energies and directions must be sampled from appropriate distributions. In elastic scattering, the scattering angle can be obtained by sampling the differential cross section [7]. The differential cross section $d\sigma/d\Omega$ relates the emission probability to the scattering angle. The energy of the scattered neutron is then calculated from the conservation of momentum and kinetic energy. The procedure is similar to elastic scattering, but the energy transferred to the target nucleus must be taken into account. In the fission reaction, the initial neutron history is terminated. The energy of the emitted neutrons is determined by the fission spectrum and the emission direction is sampled isotropically from the uniform distribution. Neutron histories are terminated in capture reactions in analog Monte Carlo and possible secondary particles are not tracked further in the conventional neutron transport simulation. However, there are Monte Carlo codes for solving coupled neutron-photon transport problems.

The following is an example of sampling the free path of a neutron. Let us assume that a neutron is traveling through a medium where the interaction probability is constant throughout the volume, the differential interaction probability for the distance dx can be defined as

$$dP = \sum\nolimits_{tot} dx, \tag{16}$$

where $\sum_{tot}$ is the total macroscopic cross-section that defines the interaction probability per distance traveled. The non-interacting probability $P_0(x)$ can be determined for a neutron that reaches a distance x from the origin without interacting. When a neutron moves the distance dx from x, it causes a decrease in non-interacting probability:

$$dP_0 = -P_0(x)dP = -P_0(x) \sum_{tot} dx. \tag{17}$$

The equation of non-interaction probability can be obtained by solving the differential equation (17) by the separation of variables:

$$P_0(x) = e^{-x \sum_{tot}}. \tag{18}$$

The mean free path of the neutron can be calculated from the non-interacting probability equation (18):

$$l = \int_0^\infty x e^{-x \sum_{tot}} = \frac{1}{\sum_{tot}}. \tag{19}$$

Using equations (18) and (16), the equation for the neutron that reaches the distance x without interaction and then interacts within the next dx can be formulated:

$$P_0(x)dP = P_0(x) \sum_{tot} dx = \sum_{tot} e^{-x \sum_{tot}} dx. \tag{20}$$

Thus, from the equation (20), the probability density function (PDF) of the free path length is

$$f(x) = \sum_{tot} e^{-x \sum_{tot}}, \tag{21}$$

which is an exponential distribution. The cumulative distribution function (CDF) is obtained from PDF by the integration:

$$F(x) = \int_0^x \left(\sum_{tot} e^{-x' \sum_{tot}} \right) dx' = 1 - e^{-x \sum_{tot}}. \tag{22}$$

When the probability distribution of the free path length is formulated for the neutrons, the next step is to select the actual values of the free path distance x from the exponential distribution. There are several methods for this task, such as the inversion method and the rejection techniques [21]. For the exponential distribution, the inversion method can be used since the inverse of CDF can be calculated in a closed form. In contrast, e.g. the inverse of Gaussian distribution cannot be solved in a closed form, but it can be calculated numerically. However, numerical calculations can be inefficient in some situations. Therefore, it can be more useful to apply rejection techniques where sampling is done only using the PDF.

In the inversion method, a random variable ζ distributed uniformly on the unit interval is needed. The inversion method produces pseudo-random numbers as the ζ is sampled using pseudo-random number generators (PRNGs). The PRNG sequences are not truly random in a sense, as they depend on the initial value. However, the numbers produced by the inversion method are sufficiently random for this sampling task [21]. PRNGs are found in common programming languages, and their theory is not essential in the scope of this thesis.

The random variable ζ is set equal to the CDF equation (22) in the inversion method. Thus, the free path length of a neutron can be calculated from the inverse of CDF:

$$F(x) = \zeta \Leftrightarrow x = F^{-1}(\zeta). \tag{23}$$

By combining the equations (23) and (22), the sampled distance is

$$x = -\frac{1}{\sum_{tot}} \ln(1-\zeta) = -\frac{1}{\sum_{tot}} \ln(\zeta), \tag{24}$$

where the last identity holds as the 1-ζ and ζ are similarly distributed.

In the sampling equation (24), the total macroscopic cross section is independent of position. In practice, also heterogeneous geometries are needed, of course. A straightforward approach is to divide the geometry into homogeneous cells. Hence, cells can have different interaction probabilities, so the free path length sampled in another cell is no longer valid. This means that neutrons must be stopped at each cell boundary and that the remaining free path must be adjusted or resampled for the next cell. This forms the foundation of the surface tracking method based on the ray-tracing algorithm, which is applied in many Monte Carlo neutron transport codes.

The surface-tracking method requires the distance to the nearest material cell in the neutron's direction of travel to determine the total remaining free path before the next collision site in the upcoming cell. Surfaces forming the boundaries of the cells are often of different types, e.g. planes and cylinders. As a result, the distance must be calculated for all neighboring cells from which the nearest is selected. Determining the surface distance can be complex and computationally demanding, as the distance depends on the position and flight direction of the neutron in addition to the surface parameters. The method becomes computationally inefficient especially if the mean free path of the neutron is long compared to the dimensions of the simulation geometry [23]. In this case, the surface distances has to be calculated many times before the actual collision.

The delta-tracking method of Woodcock [24] is an alternative to surface-tracking where the surface distances are not needed. The method uses rejection sampling, which is usually applied to situations where the inverse of the distribution cannot be calculated efficiently, even numerically. The concept of virtual collision is introduced to make the total interaction probability uniform in all material cells. Hence, neutrons can move freely across the material boundaries and do not need to be stopped. This avoids calculating distances to the surfaces of the nearest material cells, but at the same time, a new free path length must be sampled if a collision is rejected as a virtual [25].

After all the neutrons are tracked in the geometry and the interactions are sampled with the material isotopes, the next step is to collect the results from the simulated random discrete events. In the Monte Carlo simulation, this can be done separately from the neutron transport simulation. The Monte Carlo method is capable of obtaining statistical estimates for integrals [26] that describe the number of specific responses:

$$R = \int_t \int_V \int_{\hat{\boldsymbol{\Omega}}} \int_E f(\boldsymbol{r}, \hat{\boldsymbol{\Omega}}, E)\psi(\boldsymbol{r}, \hat{\boldsymbol{\Omega}}, E, t) dV d\hat{\boldsymbol{\Omega}} dE dt, \tag{25}$$

where $f(\boldsymbol{r}, \hat{\boldsymbol{\Omega}}, E)$ is the response function and $\psi(\hat{\boldsymbol{r}}, \boldsymbol{\Omega}, E, t)$ is the angular neutron flux. By setting the response function to reaction cross-section, the integral results total number of reactions in the integration domain. In addition, the response function can be set to unity when the integral results total number of neutrons. Reaction rates [1/s] and neutron flux [1/cm^{2}s] can be obtained by normalizing the integral in the time and spatial domains. In the transport simulation, the integral of the angular neutron flux eq. 25 is expressed by a sum over simulated events, e.g. collisions, track lengths, surface crossings [27].

2.3 Optimized stellarator as a fusion reactor candidate

Stellarators are potential candidates for magnetic confinement fusion reactors in addition to tokamaks. Their general advantage is the steady-state operation, where the confining magnetic field is produced by external field coils without induced toroidal plasma currents. In this way, the current disruptions and current-driven instabilities can be avoided. However, the stellarator concept has several downsides. Since in the absence of the plasma current, the helical field is produced using complex coils, the axisymmetry is lost. This will generate a genuine 3D plasma, which leads to more challenging particle confinement as e.g. neoclassical transport is higher than in axisymmetric tokamaks [10]. Moreover, the sophisticated coil system must be as close to the plasma as possible to generate an optimal magnetic field. This places limitations on the space between the plasma and the coils, which is crucial for blanket design. Therefore, the plasma conditions must be optimized together with the component design to have a feasible stellarator fusion reactor. However, the 3D configuration offers more degrees of freedom to find the optimal magnetic field configuration, but it can be a very time-consuming and costly process.

Currently, large-scale stellarators such as Wendelstein-7X (W7-X) and LHD (Large Helical Device) are operated in Germany and Japan. W7-X is an example of the drift-optimized HELIAS concept [28] in which a magnetic field is produced by superconducting modular field coils. In the design of modular field coils, there is no separation between poloidal and toroidal field coils. The advantage of modular coils is their flexibility in design. The shape of the coils as well as the toroidal periodicity and aspect ratio of the reactor, rotational transform, and magnetic shear of the field are the results of optimization criteria. In the W7-X, the optimization criteria have been based on 1) having high-quality magnetic surfaces 2) maintaining plasma equilibrium and MHD stability up to plasma beta of $\langle\beta\rangle = 4$–$5\ \%$ 3) Small neoclassical transport losses 4) fast ion (alpha particle) confinement 5) A suitable divertor concept for controlled particle and energy exhaust (e.g. island divertor) 6) feasible modular coils with realistic curvatures, strains and stresses [29].

When moving from the WX-7 to the next-step HELIAS reactor, the optimization criteria are developed. Physics and engineering questions for the next-step HELIAS have been presented in ref. [10]. Five-fold symmetry has been chosen for the development of the next-step reactor HELIAS 5-B, which has also been used in

WX-7. The B in the name refers to the technological state of the reactor. Three technological options for the next-step device have been introduced. Option A is the fast and cost-efficient reactor that would answer the remaining physics questions. On the contrary, option C would be similar to a DEMO with a complete blanket that could demonstrate the net power production of electricity. Option B is then a compromise between the two boundary options. Thus, there is still a lot of room for maneuvering in the design of the reactor.

Studies and operation of W7-X have shown that magnetic field and coils require more optimization to solve plasma physics issues by design [10]. For example, turbulent transport was not taken into account in the optimization of the W7-X. But it was later found that the transport of larger stellarators may actually be dominated by turbulence rather than neoclassical transport.Therefore, it must be included in the design of the next device. Moreover, there are lots of remaining engineering questions related to, e.g. maintenance of the components and the remote handling, heating and cooling system, divertor, and tritium processing. In addition, a stellarator-specific blanket system is one of the open questions, as many of the blanket concepts have been primarily developed for the tokamak DEMO. From the current main blanket candidates HCPB and WCLL, the HCPB could be more favorable for the HELIAS due to the reduced blanket thickness to achieve TBR self-sufficiency [18]. On the other hand, WCLL is observed to have superior neutron shielding performance [18]. Along with these, DCLL concept could be a long-term option. Double cooling can enable a wider design margin and a higher coolant temperature, leading to higher plant efficiency. Overall, the design of the next-step stellarator is still under discussion. However, it is planned to have a test environment for neutrons. In order to make educated decisions, a wide range of modeling capabilities, including neutron transport, need to be developed in the near future.

3 Simulation tool and input

3.1 Serpent

Serpent [3] is a C-written 3D Monte Carlo particle transport code from which the Serpent 2.1.32 version is used to simulate neutrons in this work. It was originally developed for burn-up calculations in fission reactors by the VTT Technical Research Center of Finland. However, it has also started to be applied in other fields of research, e.g. in fusion neutronics and radiation transport. One of the characteristics of Serpent2 is that it uses a combination of the delta- and surface-tracking methods in particle tracking [3]. The advantage of using delta tracking is that the distances to the nearest material cells do not have to be calculated. This can speed up the calculation when, e.g. the mean free path of the neutron is long compared to the dimensions of the simulation geometry [23].

Simulation geometries can be constructed in Serpent2 in several formats: constructive solid geometry (CSG), unstructured mesh-based geometry type, and CAD-based STL geometry [30]. The most common geometry type in Monte Carlo codes is the CSG. In the CSG format, the geometry is represented as cells, which are constructed from Boolean combinations of surfaces. However, the CSG format can be inefficient for modeling complex, rapidly evolving CAD designs of reactors. An additional conversion tool is required to convert CAD geometry to CSG format. In addition, geometries that contain thousands of surfaces and cells are difficult to manage and modify. Therefore, it can be more useful to work with CAD-based STL (Standard Triangle Language) geometries, where the geometry is represented as a triangle mesh. The reactor CAD models can be exported from the CAD software in STL format and included directly in the Serpent input. In this way, the usage of CAD-based STL geometry can simplify and speed up the modeling process.

The simulation process in Serpent is illustrated in Figure 4. The main part before running the simulation is to create the user input, which is then read by the code. It consists of defining, e.g. the neutron source, simulation geometry, materials, and detectors for scoring different reactions. Furthermore, the nuclear data must be specified for the simulation in ACE format. The Evaluated Nuclear Data File (ENDF) format library JEFF33 [31] was used in this work. When the user input and nuclear data are read and processed, the process proceeds to the actual transport simulation. After the transport cycle, the results are collected and written to output files for analysis.

The input data can be shared to parallel transport cycles. Serpent enables parallel computing using MPI [32] and OpenMP [33] technologies. OpenMP can be used when the simulation is limited to a single computing node. The calculation process is divided into multiple threads where the memory of the process is shared between the threads. In turn, in the MPI, there are multiple processes where the calculation can be separated into multiple nodes that are communicating with each other. However, in Serpent, the parallel tasks do not interact or transfer data until the main transport cycle is finished. This is possible due to the fact that neutrons do not affect each other's histories. MPI and OpenMP have been applied in combination in this work. In other words, multiple tasks (processes) have been utilized, and in each task, multiple computing threads have been used as well.

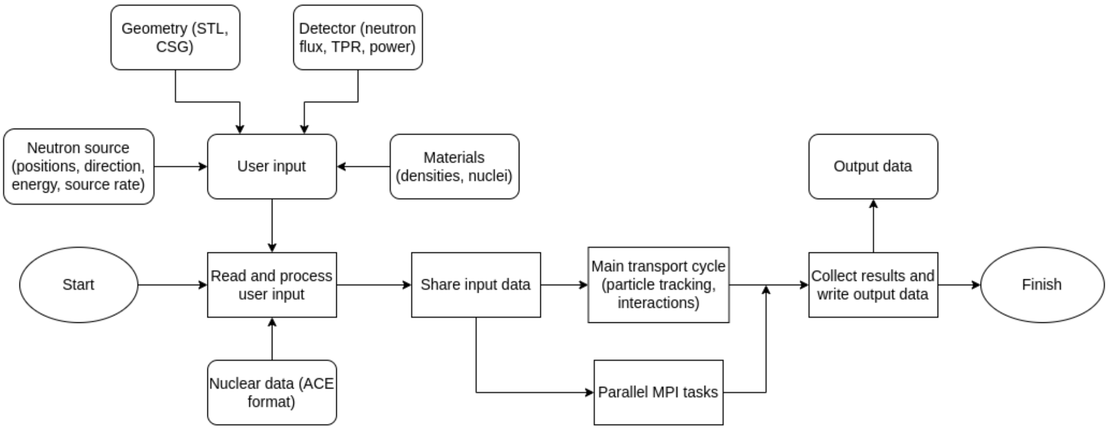

Figure 4. Illustration of simulation process in Serpent.

3.2 HELIAS reactor CAD models

The HELIAS reactor model used in this work is based on the design of the HELIAS 5-B reactor [12]. It has a 5-fold symmetry, i.e. the reactor consists of five 72° sectors that are similar to each other. The illustrative design of the reactor's magnet system and the vessel components is shown in Figure 5. Some of the essential reactor specifications are shown in Table 1, in which they are compared with those of ITER and EU DEMO1. From the reactor design parameters, HELIAS 5-B has the highest fusion power and major radius. In addition, it has the most complicated coil system with 50 non-planar field coils.

Table 1. HELIAS 5-B, ITER, and EU DEMO1 reactor specifications [12] [34].

Reactor	HELIAS 5-B	ITER	EU DEMO1
Major radius [m]	22	6.2	9
Average minor radius [m]	1.8	2.0	2.9
Plasma volume [m^3]	1407	837	2500
Number of coils	50	18	22
Average field on axis [T]	5.9	5.3	5.9
Fusion power [MW]	3000	500	2000

Different CAD models of HELIAS 5-B have been constructed for neutron simulations. A CAD model [35] that describes the 36° sector of HELIAS 5-B is shown in Figure 6.A. The 36° sector is called a half-module, whereas the 72° sector is called a full-module. The full-module is shown in figure 6.B. The CAD model consists of six radial layers: plasma, last-closed flux surface (LCFS), blanket, and three vacuum vessels (VV) (inner shell, shield, and outer shell). In addition, there is a CAD model of non-planar field coils [36] that is shown in Figure 6 as well. The coil system consists of five coils with unique shapes. The other five coils required for the symmetric 72° sector are made by mirroring and 180° roll. The coils consist of two structures, the winding pack and the jacket case. The winding pack consists of the actual conductive part including superconducting Nb_3Sn. The jacket case surrounds the winding pack and acts as a structural and radiation-shielding component of the coils.

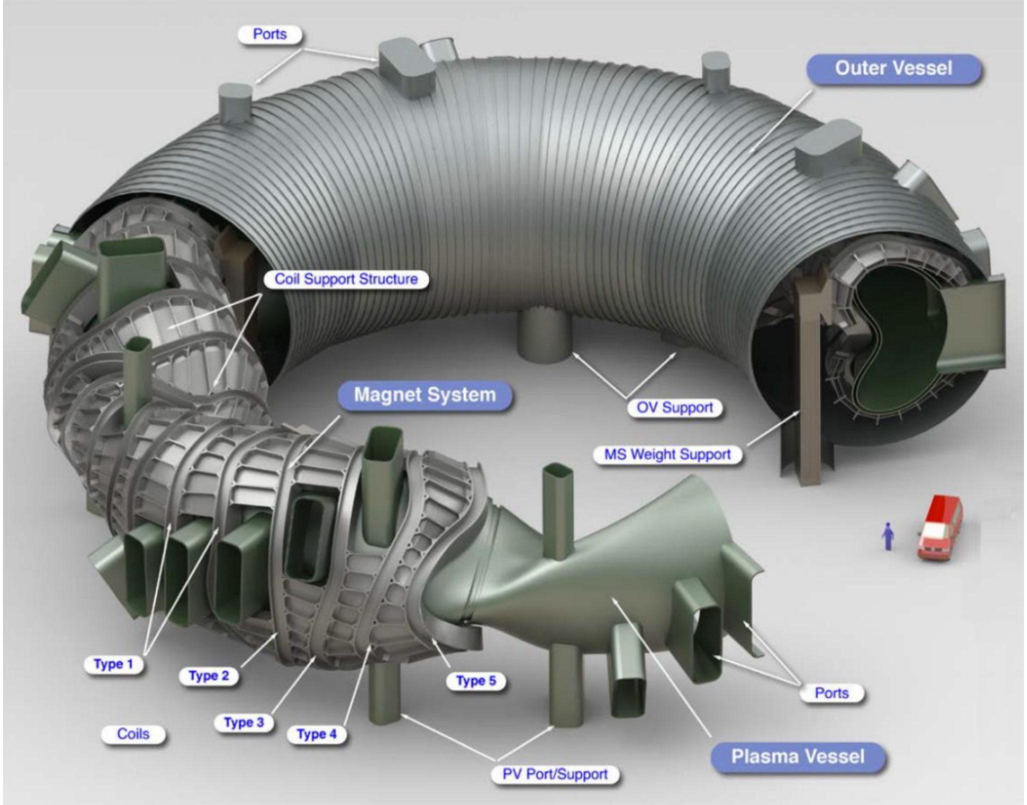

Figure 5. HELIAS 5-B reactor design visualized [12]. A magnet system containing 50 non-planar field coils is surrounding the plasma vessel. Various support structures and ports are illustrated in the reactor design. A car and a human on the right give a picture of the scale of the reactor. The major radius of the reactor is 22 m.

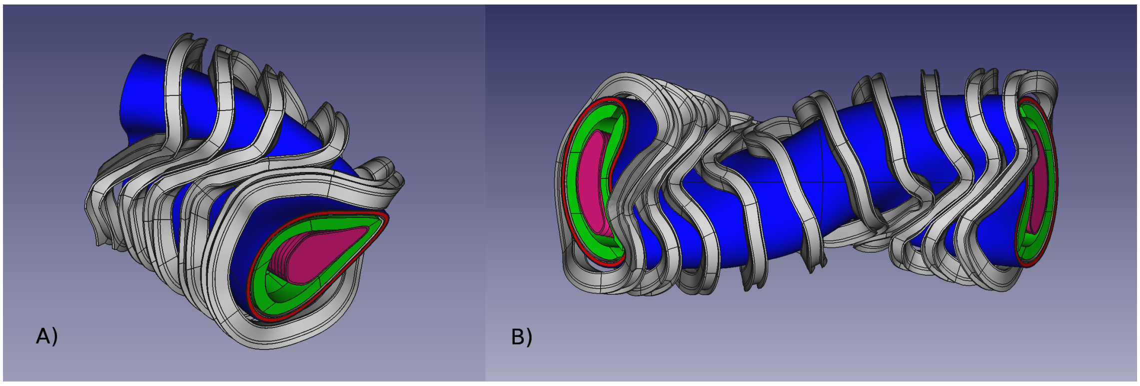

Figure 6. A) Half-module (36° sector) of the HELIAS 5-B reactor CAD model B) Full-module (72° sector) that has the 5-fold symmetry. There are 10 non-planar field coils in each full module, so the total number of coils is 50.

Another CAD model that describes HELIAS 5-B is the so-called parametric model, which is the focus of this work. It is constructed by the parametric geometry tool HeliasGeom [37] that enables specifying the toroidal sector of the geometry, e.g. 72° or 360°, toroidal and poloidal discretization, number and thickness of the layers. Parametric 72° model including seven layers with different thicknesses is shown in Figure 7. It must be noted that the constant thickness is a clear simplification of the HELIAS 5-B geometry, where, e.g. the thickness of the blanket varies between the inboard and outboard sides. Moreover, all layers follow the plasma shape with a user-defined distance, which is not the case in the HELIAS 5-B design either. In addition, the parametric model does not directly produce ports and space for the divertor. Therefore, the model can overestimate, e.g. tritium breeding and neutron shielding. Despite of these simplifications, the parametric tool provides an efficient way to construct several geometry models of the HELIAS for parametric studying and optimizing the layer thicknesses.

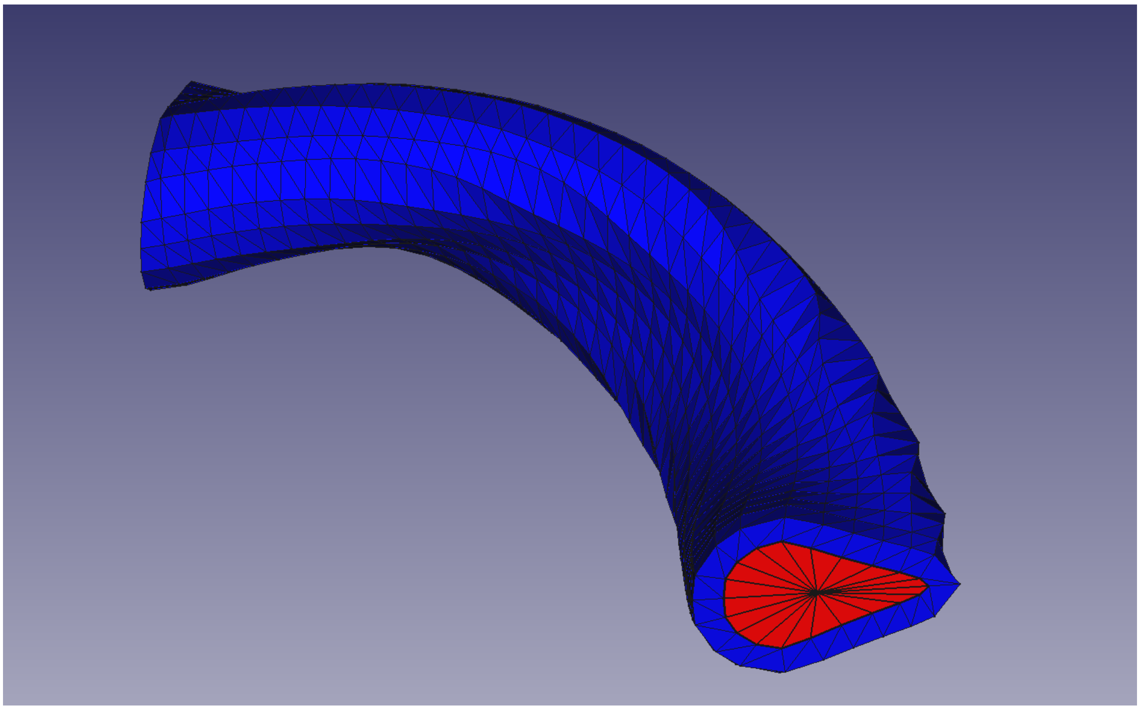

Figure 7. Parametric 72° CAD model of the HELIAS. Seven geometry layers with different thicknesses. 20 poloidal cells in each toroidal cross-section. 40 toroidal cross-sections.

3.3 From CAD models to Serpent input

Both CAD models presented in the previous section are produced in the STP/STEP file format (STEP, Standard for the Exchange of Product Model Data). To be included in the Serpent input, they had to be converted to the STL file format. For this task, the FreeCAD software was used. As the CAD models of HELIAS are large and complex, errors can occur in STL mesh conversion. Furthermore, Serpent2 ray test algorithms have been found to have issues not only due to inaccuracies in converted STL models, but also with floating point precision [30]. The most common issues with STL geometry are gaps between the edges of the adjacent facets. Another type of error in the STL format is a degenerate facet, in which all three points are located on the same line. Serpent2 has methods for tolerating these errors, which can be controlled by input parameters of the STL geometry definition. Errors do not necessarily prevent the use of the STL model, but they can also lead to the termination of the simulation.

In this work, the errors in the STL geometries were checked using the Serpent *checkstl* method. The method samples a number of random points in the STL geometry, and a number of rays are started from each point. The test rays give the same result if the triangle surfaces are intact. 1×10^4 points and ray directions were used to test the STL geometries in this work. STP CAD models were converted to STL meshes using *Create mesh from shape* in FreeCAD software. The Netgen meshing method with the finest parameters was found to be suitable for problematic parts such as the coil system. However, there were 14 parts from 4868 that had to be neglected. Respectively, the FreeCAD standard mesher was used for the module layers. Part objects were converted using the graphical user interface of FreeCAD. However, to export the meshes as separate STL files, the Python console of FreeCAD had to be used. An example of the conversion process is given in Appendix C. The CAD model of the coils was only for the 36° sector. The other five coils for the symmetric 72° sector had to be generated using rotations in the FreeCAD software. The example of the rotation procedure is found in Appendix C.

The fineness of the meshing affects the volume loss moving from the STP geometry to the triangulated geometry. Curved surfaces can be accurately modeled in the STP format, whereas in the faceting process, part of the volume is automatically lost. Volume losses are important to take into account when results from different geometry models are compared.

3.4 Parametric model inputs

The following sections describe the simulation inputs of the benchmark and parametric study. All input definitions are based on the Serpent Wiki [27].

3.4.1 Neutron flux benchmark

In the parametric model benchmark input, the volume-averaged neutron flux was calculated in all STL geometry cells. Along with the neutron flux simulation, a cell volume calculation was needed to obtain the flux result. The neutron flux tally [cm/s] is divided by the cell volume [cm^3] to produce the flux result [$1/\mathrm{cm}^2\mathrm{s}$]. Volume estimation was carried out using a Monte Carlo-based volume calculation routine *checkvolumes* in Serpent. The uncertainty of the neutron flux tally was combined with the uncertainty of the Monte Carlo volume estimation. The volume estimation takes a number of sampled random points in the simulation geometry as an input parameter. The method then checks the material associated with each point and gives an estimate of the material volume. An arbitrary volume test material was defined for each geometry cell.

The parametric model benchmark was performed for 72° and 360° models. The same discretization of geometry was used in the benchmark input, which is shown in Figure 7: 20 poloidal cells for each 40 toroidal cross sections, which equals 800 cells in total for each layer. There were 4 geometry layers: plasma, first wall armor, structural EUROFER steel, and LiPb breeding layer, which brings the total number of cells to 3200. In the 360° model, the corresponding number of cells was five times the number of cells in the 72 model, 16000 in total (4000 cells in each layer). The neutron flux was calculated in each volumetric cell by setting the cell name (index) as a parameter to the detectors.

Cell numbering starts from the innermost plasma layer and proceeds to the outermost LiPb breeding layer. Therefore, in the 72° geometry, cells 1–800 correspond to the plasma layer, and cells 3200–4000 to the LiPb breeding layer. The first and last 20 cells of the layers are on the edges of the 72° simulation sector. Cells of the layers are poloidally traversed. The cell numbers corresponding to the layers are shown in Table 2 in the 72° and 360° geometries.

Table 2. Cell numbers corresponding to layers in 72° and 360° geometries.

Model\Layer	Plasma	FW	EUROFER	LiPB	total count
72°	0–799	800–1599	1600–2399	2400–3199	3200
360°	0–3999	4000–7999	8000–11999	1200–15999	16000

The four geometry layers were specified by different thicknesses and material compositions. The layers had thicknesses with orders of magnitude differences, which could show the compatibility of the codes on different size scales. The first-wall armor was the thinnest 1 mm layer directly after the plasma. The structural layer was then 2 cm from the FW armor. Finally, the breeding layer was the thickest at 80 cm. In the material definitions, the plasma layer was set to void, the first-wall armor consisted mainly of tungsten, the structural layer consisted of EUROFER steel, and the breeding layer consisted of LiPb. In lithium, the enrichment of Li7 was 88.5 %. The exact material composition used in the simulation is shown in Appendix A.

The 72° model was simulated using the periodic boundary condition. The boundary condition was constructed using the *usym* method. Actual particle translations were used on the sector boundary instead of geometry translations. Both methods have been tested to produce similar results. Nevertheless, the actual particle translation method was chosen because it is used in MCNP as well. The simulation geometries of the 72° and 360° models are shown in Figure 8 using the Serpent plot tool.

Neutron source routine described in ref. [38] was used in all simulations in this work. Serpent2 performs user-defined neutron source subroutine, which takes neutron emission probabilities and sampling positions as an input. The positions and emission probabilities have been adopted from plasma physics simulations of the HELIAS. Neutron source points are sampled from the cumulative probability of emission probability using a random number generator. The source point corresponding to the cumulative probability is searched by binary search. The flight direction of the neutron is set to be isotropic and the neutron energy is monochromatic 14.1 MeV.

The full module neutron source file that contains the source positions and emission probabilities for the entire 72° sector was used in all simulations. In the 360° model simulation, random translations of the sampled source points were needed to sample neutrons throughout the geometry. Figure 9 shows the source rate plots in the 72° and 360° geometries.

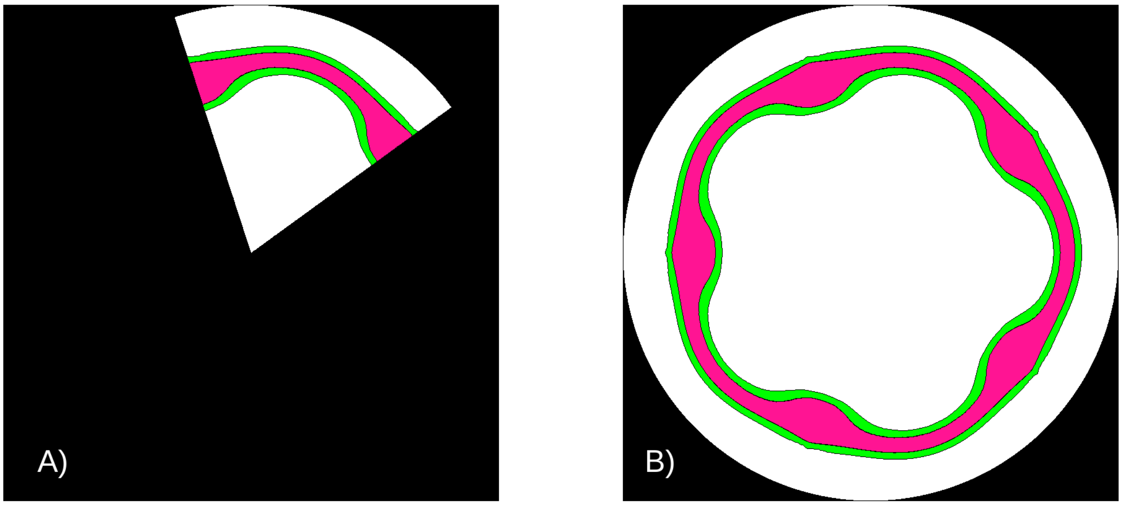

Figure 8. A) 72° model geometry input plotted in Serpent. Neutron transport is restricted to the 72° sector by particle translations on the sector boundary. B) 360° model geometry. Plasma layer is colored in pink and LiPb layer in green in both plots. Thin first-wall and structural layer are not visible in the plots. White color illustrates cylinder shaped cell in which the STL geometry is placed.

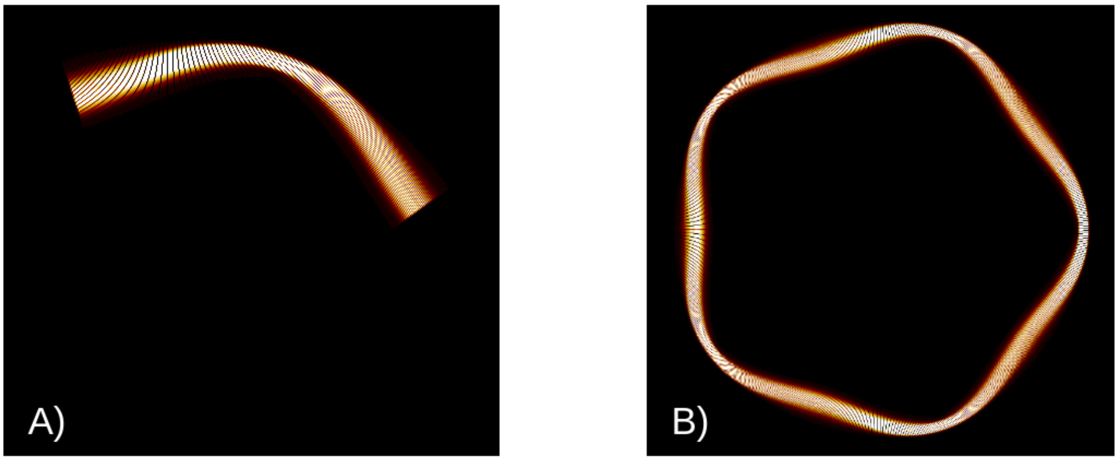

Figure 9. Neutron source rate plots for A) 72° and B) 360° simulations.

3.4.2 Tritium breeding ratio (TBR)

TBR was calculated with parameterized breeding zone thickness and two homogenized BZ compositions, DCLL and HCPB. Five thicknesses of breeding zone 25, 37.5, 50, 62.5, and 75 cm were selected based on the geometric constraints of HELIAS 5-B [10]. Figure 10 shows the maximum and minimum space in the inboard and outboard sides of the module. Breeding zone thickness of 50 cm has been studied for the different blanket concepts [18]. However, a wide range of BZ thicknesses was selected for this study. The breeding zone layers with the different thicknesses are shown in Figure 11 together with the limiting coil system.

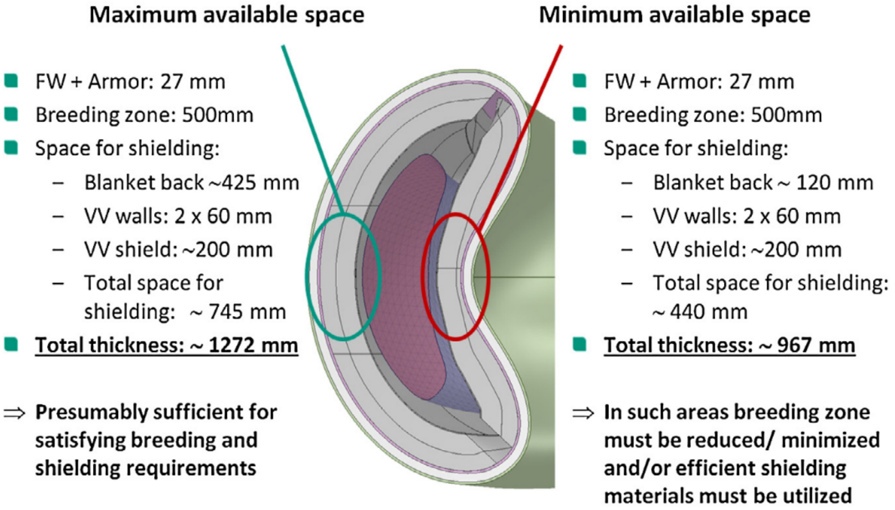

Maximum available space

- FW + Armor: 27 mm
- Breeding zone: 500mm
- Space for shielding:
  - Blanket back ~425 mm
  - VV walls: 2 x 60 mm
  - VV shield: ~200 mm
  - Total space for shielding: ~ 745 mm
- **Total thickness: ~ 1272 mm**

⇒ **Presumably sufficient for satisfying breeding and shielding requirements**

Minimum available space

- FW + Armor: 27 mm
- Breeding zone: 500mm
- Space for shielding:
  - Blanket back ~ 120 mm
  - VV walls: 2 x 60 mm
  - VV shield: ~200 mm
  - Total space for shielding: ~ 440 mm
- **Total thickness: ~ 967 mm**

⇒ **In such areas breeding zone must be reduced/ minimized and/or efficient shielding materials must be utilized**

Figure 10. HELIAS 5-B geometry constraints of inboard and outboard sides of the module [10].

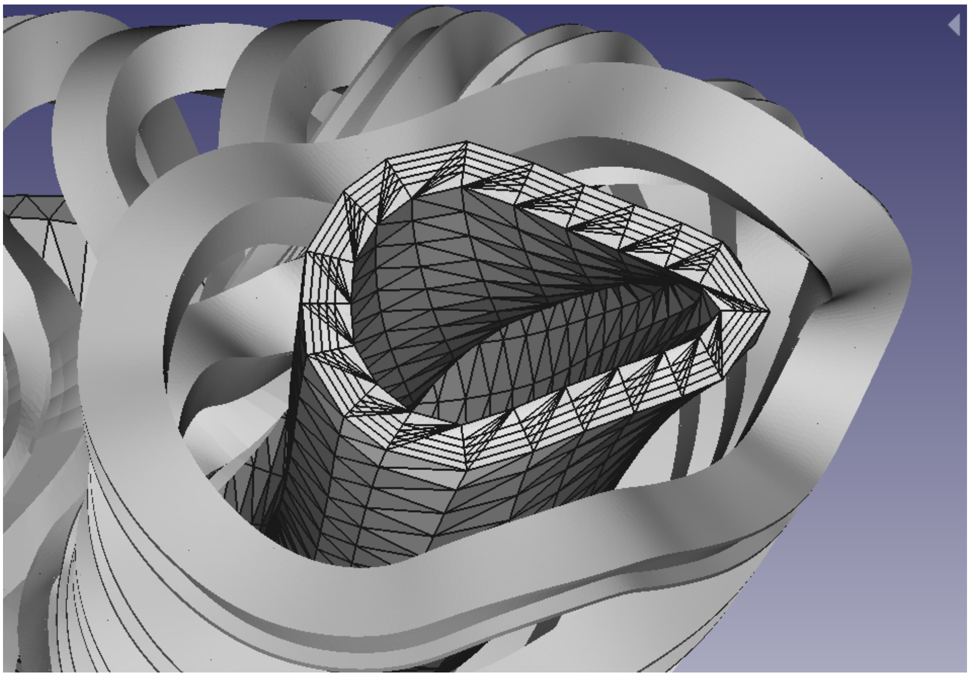

Figure 11. Breeding zone thicknesses from 25 cm to 72 cm illustrated together with the limiting coil system.

The geometry model consisted of 7 layers: armor, FW, BZ, back-support structure (BSS), and 3 vacuum vessels (inner shell, shield, outer shell). There was no defined intermediate space between the layers. The thickness of the other layers except the BZ was kept constant in the simulations. Only the radial starting point of the layers was changed with the varying BZ layer. Thicknesses of the layers were adopted from the [10] (Figure 10). The thickness of the BSS was chosen between the inboard and outboard thicknesses. The thickness of the BSS was set to a minimum (12 cm), because a BZ layer as thick as 75 cm was simulated.

DCLL and HCPB blanket compositions have the same tungsten armor, FW, and vacuum vessels in this study. Thus, the blanket concepts vary only in terms of BZ and BSS materials. The material compositions of BZ and BSS of HCPB were converted from the volume fractions of ref. [38]. The mass densities of the materials were needed for conversion, which are shown in Table 4. The selected densities are roughly defined under NTP conditions. Therefore, the designed temperatures and pressures of the HCPB blanket, e.g. 8 MPa, $T = 300–500°\text{C}$) for helium, were not taken into account in the densities. The material compositions of the vacuum vessels were obtained as MCNP material cards from HELIAS DCLL study [39]. The volume fractions of the HCPB material composition are shown in Table 3. The exact material composition is shown in Appendix B.

The material compositions of BZ (M24) and BSS (M71) [39] of DCLL were obtained as MCNP material cards. Tungsten was removed from the BZ composition (M24), as there was a separate tungsten armor layer. The volume fractions of the DCLL composition are shown in Table 5 and the exact material composition is found in Appendix B.

TBR simulations were performed using the 72° model with the same discretization as in the benchmark sec. 3.4.1. Tritium production was calculated using both microscopic (ENDF MT = 205) and macroscopic detectors (ENDF MT = -55). The tritium production using a microscopic detector was calculated separately for Li-6 and Li-7 in the BZ. In turn, the macroscopic detector was defined to calculate the total tritium production with all possible reaction channels in the BZ.

Table 3. Volume fractions [%] of the homogenized HCPB material composition.

Mat./Layer	Armor	FW	BZ	BSS	VV inn & out)	VV shield
W	100	0	0	0	0	0
EUROFER	0	64.91	9.85	60.61	100	0
S.S.316LN	0	0	0	0	100	60
He	0	35.09	38.61	39.39	0	0
Li_4SiO_4	0	0	14.91	0	0	0
H_2O	0	0	0	0	0	40
Beryllium	0	0	36.63	0	0	0

Table 4. Mass densities used to construct the material definition from volume fractions. Be, He, W densities from ref. [40] and Li_4SiO_4 from ref. [41]. EUROFER and LiPb densities taken from MCNP material inputs [39].

Material	mass density [g/cm^3]
Be	1.848
He	1.63×10^{-4}
W	1.93×10^{1}
LiPb	9.572
Li_4SiO_4	2.35
EUROFER	7.884

Table 5. Volume fractions [%] of the homogenized DCLL material composition.

Mat./Layer	Armor	FW	BZ	BSS	VV inn & out	VV shield
W	100	0	0	0	0	0
EUROFER	0	64.91	24.6	71.8	0	0
S.S.316LN	0	0	0	0	100	60
He	0	35.09	4.4	1.8	0	0
LiPb	0	0	70.8	26.4	0	0
Al_2O_3	0	0	0.16	0	0	0
H_2O	0	0	0	0	0	40

3.4.3 Neutron shielding calculations

Neutron shielding simulations consisted of the calculation of the fast neutron flux $E \in [0.1, 20]$ MeV in the full-coil system with different blanket thicknesses. In addition, radial neutron flux profiles were calculated until the end of the last VV layer. The coils were not included in the radial profile inputs. Figure 12 shows the numbered full coil system with a blanket configuration of BZ = 75 cm and BSS = 12 cm. There are 10 coils, where the numbering is from one to five for the original and rotated coil systems. Seven parts of the jacket case of the fifth coils had to be discarded due to the unsuccessful mesh conversion. Fast neutron flux detectors were determined for each coil cell. In addition, Monte Carlo volume estimation was performed on the coils for the neutron flux calculation.

Radial profiles were calculated on the outboard side of the module at a toroidal angle of 36° from the end of the sector. The location of the profile is shown in Serpent2 in Figure 13 with a BZ of 50 cm and a BSS of 12 cm. Cartesian mesh detectors were defined from $x = 2487.8$ cm to the end of the VV using 1–4 cm binning. The maximum radial distance was studied with BZ = 50 cm, BSS = 42.5 cm, where the total radial thickness was 127.2 cm. The simulation geometry was translated in Serpent2 so that the x-direction corresponded to the radial direction at the 36° angle as shown in Figure 13. The profiles were defined with different perpendicular areas in y- and z-directions from -5 to 5 cm, from -10 to 10 cm, and from -25 cm to 25 cm.

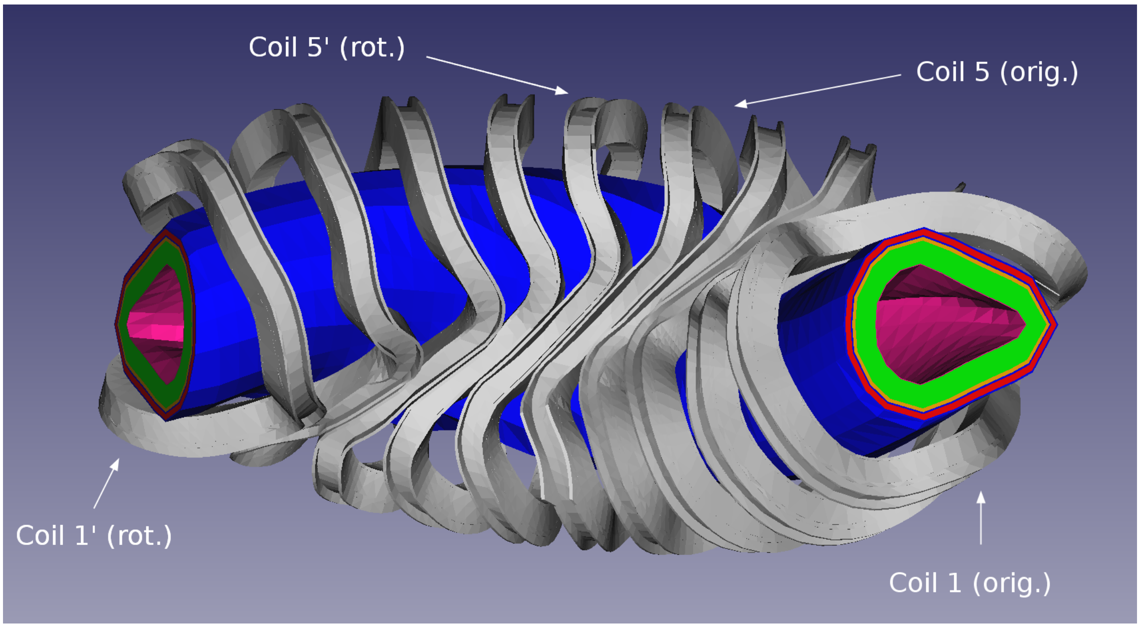

Figure 12. The numbered coil system of the 72° model, where the thickness of the BZ is 75 cm (green) and the thickness of the BSS layer is 12 cm (orange).

The material composition of the coils is shown in ref. [39]. MCNP material card was applied to Serpent. The volume fractions of the winding pack and the jacket case of the coils are shown in Table 6. The exact material composition is found in Appendix B.

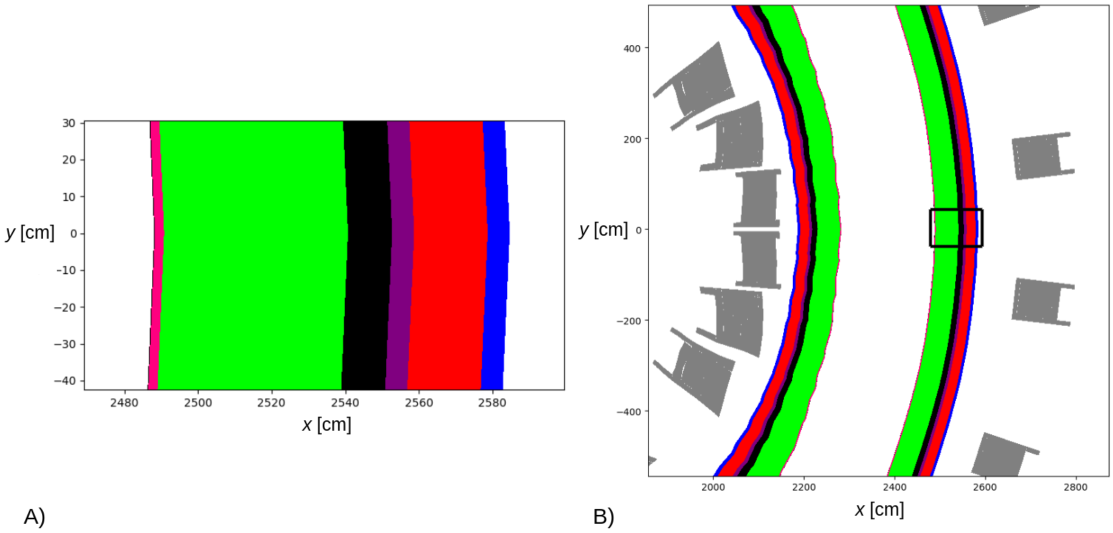

Figure 13. A) Location of the radial profile in xy-plane. B) A wider view of the location of the radial profile, which is shown as a black rectangle. The geometry corresponds to a blanket configuration: BZ = 50 cm (green), BSS = 12 cm (black).

Table 6. Volume fractions [%] of the coil system material composition.

Layer/Mat.	r-epoxy	Nb_3Sn	Bronze	Cu	He (liq)	S.S.316LN	Void
Winding pack	18	2.895	7.35	11.69	16.82	43.19	0.055
Jacket case	0	0	0	0	0	100	0

4 Results

4.1 Parametric model benchmark

The compatibility of Serpent2 and MCNP6 in the cell flux benchmark is evaluated using 1σ and 1.96σ statistical Monte Carlo error margins for neutron flux difference. In addition, the average and maximum of absolute relative difference of the flux are analyzed.

4.1.1 72 degree model

The relative difference in neutron flux between the codes was calculated for each geometry cell. The absolute value of the relative difference d_r is given as follows

$$|d_r| = \frac{|\phi_s - \phi_m|}{\phi_m} \times 100, \tag{26}$$

where the ϕ_s is the Serpent2 flux and ϕ_m is the MCNP6 flux. The average absolute relative difference $\overline{|d_r|}$ and the maximum absolute relative difference $\max(|d_r|)$ of the flux are shown in Figures 14 and 15. Three separate simulations were carried out in Serpent2 using different number of neutron histories: 10M, 100M, 500M. In the MCNP6, 1×10^9 histories were simulated. The average absolute relative difference in the total number of cells is less than 0.8 % at the three levels of statistical uncertainty. The average and maximum differences increase with increasing statistical uncertainty, i.e. by simulating fewer neutrons. The figures show that the average and maximum relative differences are the largest in the FW layer, which is the thinnest layer in the geometry.

Average and maximum absolute relative differences in the Monte Carlo cell volume estimation are shown in Figure 16. The average and maximum differences are the highest in the FW layer. Figure 17 shows the relative difference in cell volume as a function of cell number, where the statistical Monte Carlo error margin of 1σ was exceeded. 53.2 % and 81.2 % of the cell volumes are within the intervals 1σ and 1.96σ. If the results of the Monte Carlo volume estimation are normally distributed

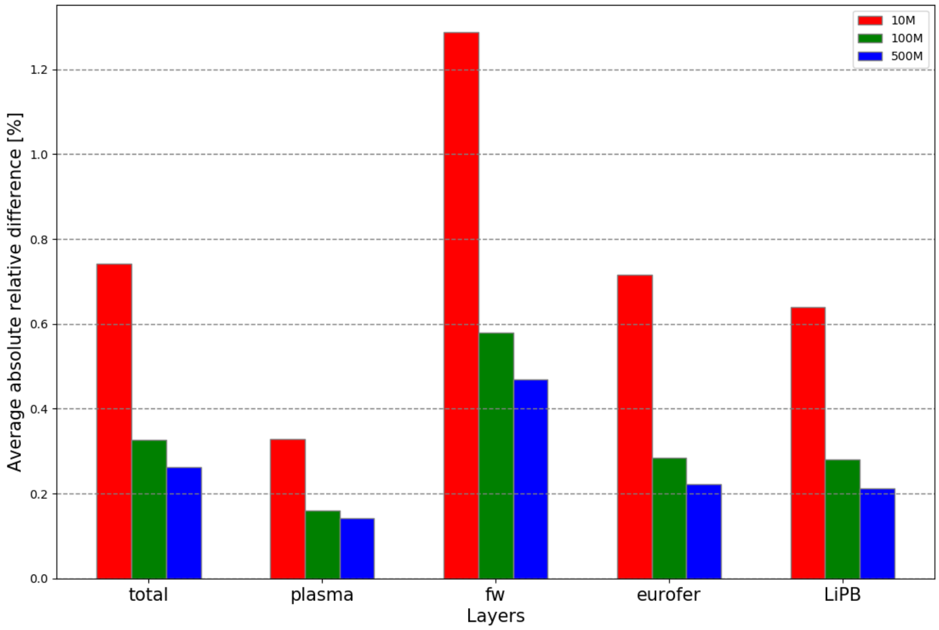

Figure 14. Average absolute relative differences of the neutron flux in the geometry layers of the 72° model with different levels of statistical uncertainty. 1×10^7, 1×10^8 and 5×10^8 neutron histories simulated.

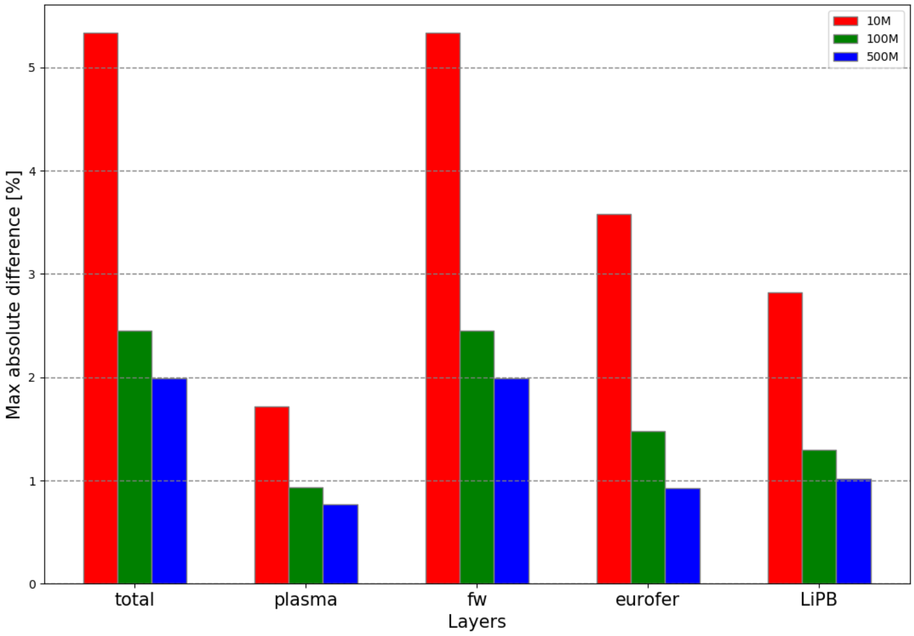

Figure 15. Maximum absolute relative differences of the flux in the geometry layers of the 72° model with different levels of statistical uncertainty.

according to the central limit theorem, then the expected number of cell volumes within 1σ and 1.96σ would be 68% and 95%. The expected result would mean that there are no systematic errors between codes or geometry inputs. However, in this case, the systematic volume error is most likely due to the different input geometry formats STL and CSG between Serpent2 and MCNP6.

Figure 18 shows the relative difference in neutron flux as a function of cells, in which the 1σ difference margin was exceeded. Thus, the white region around zero describes the statistical uncertainty level. The statistical errors of the neutron flux score and volume estimation have been combined in the error margin. In Figure 18, the three graphs show simulations performed with different amounts of neutron histories. The range of relative difference decreases by simulating more neutrons i.e. decreasing the statistical uncertainty level. However, with improved statistical accuracy, fewer cells are within the statistical error margins. This is shown in Table 7, which shows the percentage of cells within the combined error margins of 1σ and 1.96σ. In the simulation with 1×10^7 neutron histories, 93.3 % of the cells were within 1σ, while with 5×10^8 histories, the percentage was only 76.3 %. This indicates a systematic error between the simulations, which appears when the statistical margin of error is reduced.

Figure 18 shows an increase in relative difference in the ends of the simulation sector. The sector ends for each material layer have been visualized by vertical lines. At the vertical lines, the relative difference follows a spike-like pattern. Although the pattern attenuates by decreasing the statistical accuracy, it can still be identified from the 10M simulation graph. Therefore, this indicates a systematic error at the ends of the simulation sector.

Table 7. Percentages of the cells within the statistical error margins 1σ and 1.96σ in the 72° model. Three simulations with a different amount of neutron histories.

Neutron hist.\Err. margin	1σ	1.96σ
1×10^7	65.5 %	93.3 %
1×10^8	58.1 %	86.6 %
5×10^8	45.3 %	76.3 %

Figure 19 shows the Gaussian probability density functions of the standardized difference of the neutron flux with three levels of statistical uncertainty. The PDF

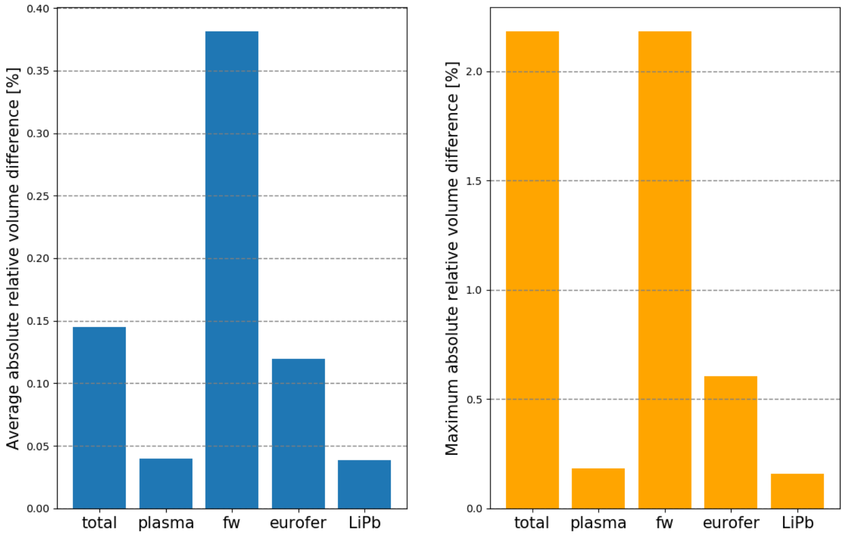

Figure 16. Average and maximum absolute relative differences of the Monte Carlo cell volume estimation in the geometry layers of the 72° model.

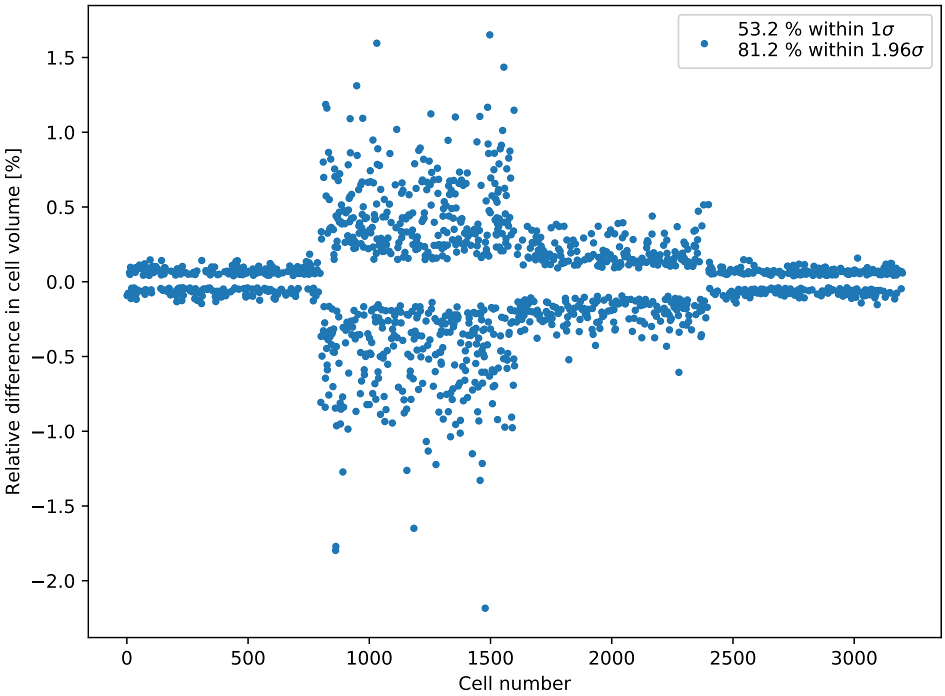

Figure 17. Relative differences in cell volumes between Serpent2 STL and MCNP6 CSG inputs in the 72° model. Only the cells that exceed the 1σ error margin have been plotted.

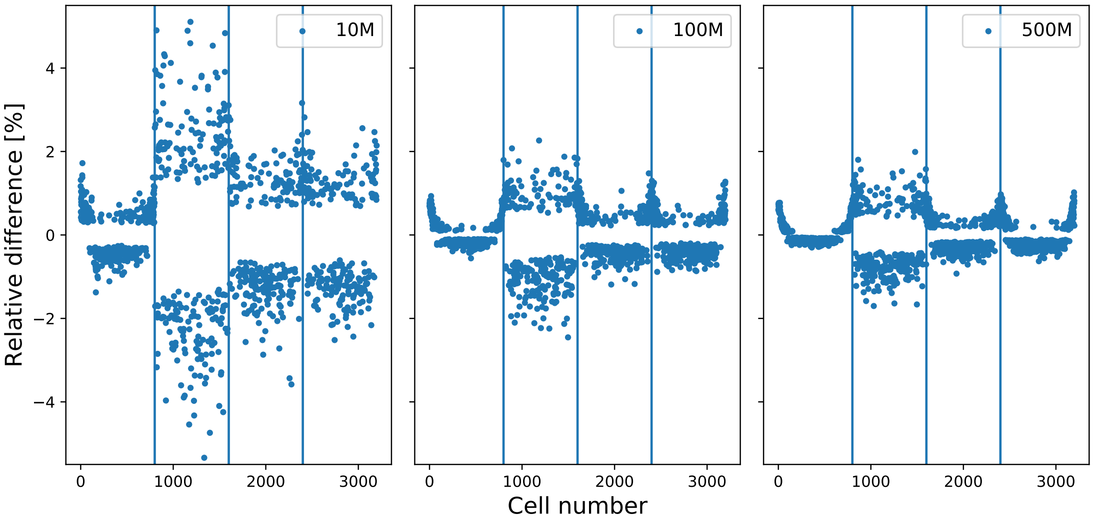

Figure 18. Relative neutron flux difference in cells exceeding the 1σ error margin. Vertical lines show 72° sector boundaries for the four material layers.

of the simulation with the highest statistical uncertainty has the best fit to the expected distribution. This is also seen in the distribution parameters, shown in Table 8. In the 10M simulation, the mean and standard deviation of the distribution are $\mu = 0.00$ and $\mu = 1.09$. When statistical accuracy increases, the mean value drifts to the right, and the standard deviation of the distribution increases. As seen in the 500M simulation, $\mu = 0.16$ and $\sigma = 2.04$. This is an additional sign that the two simulations have a systematic error.

Table 8. Parameters of the standardized distributions of the neutron flux difference.

	Expected	10M	100M	500M
μ	0	0.00	0.12	0.16
σ	1	1.09	1.50	2.04

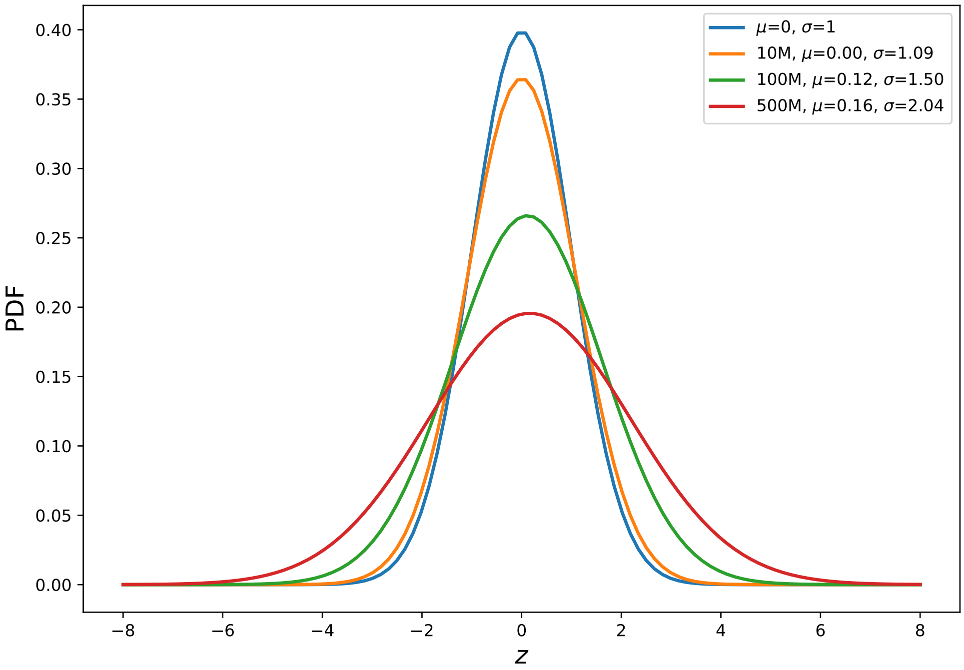

Figure 19. Gaussian probability density functions of the standardized difference of the neutron flux in the 72° model.

4.1.2 360 degree model

In this section, the discussion shifts to the results of the 360° model. Figure 20 shows the average and maximum relative differences in flux in the geometry layers. The differences are the highest in the FW layer, as in the 72° model benchmark. When average relative flux differences are compared to the 72° model results, the average differences settle in a similar range of 0.2 - 1.5 %. In this case, the comparison is done to the simulation with 1×10^7 neutron histories, since the statistical accuracy of the 72° simulation was roughly 5 times higher.

Figure 21 shows the average and maximum volume differences in the geometry layers. Similar to the 72° model, the average and maximum deviations are the largest in the thinnest layers, FW and EUROFER. Relative volume differences are shown as a function of cell number in Figure 22. The volumes of the 360° model fit better to the expected confidence intervals than the 72° model: 67.0 % and 94.6 % of cell volumes are within the 1σ and 1.96σ intervals.

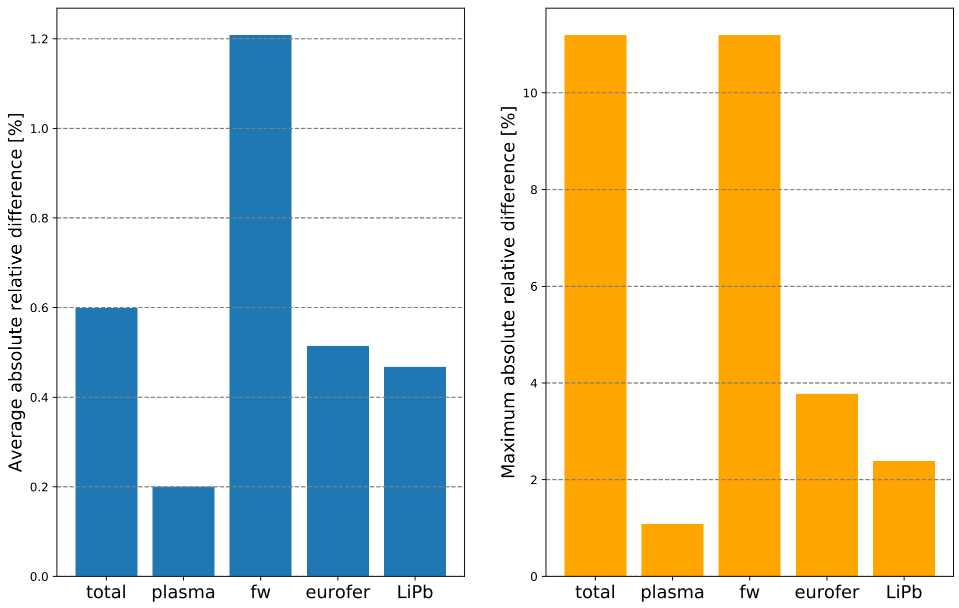

Figure 20. Average and maximum absolute relative differences in flux in the geometry layers of the 360° model.

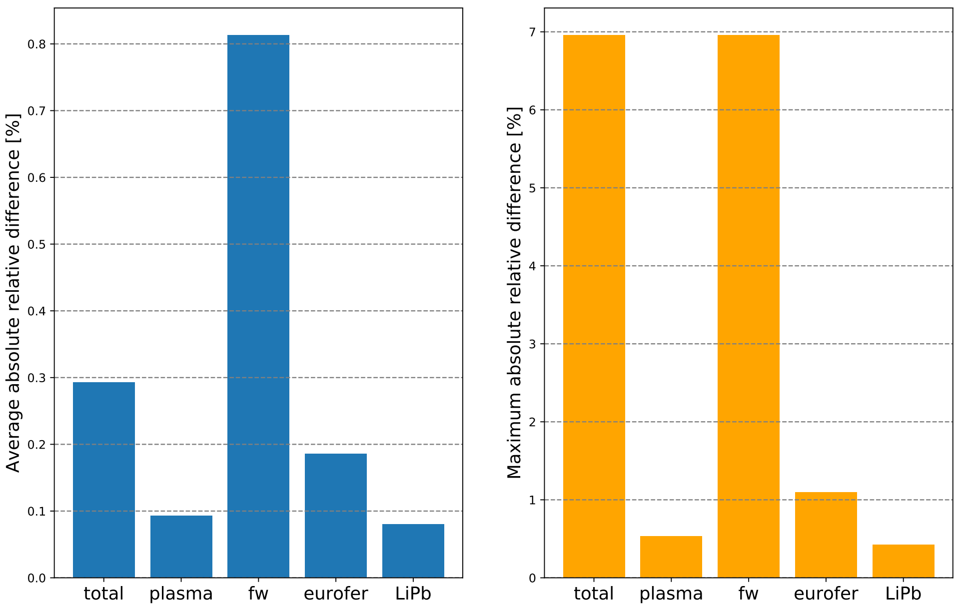

Figure 21. Average and maximum absolute relative differences of the Monte Carlo cell volume estimation in the geometry layers 360° model.

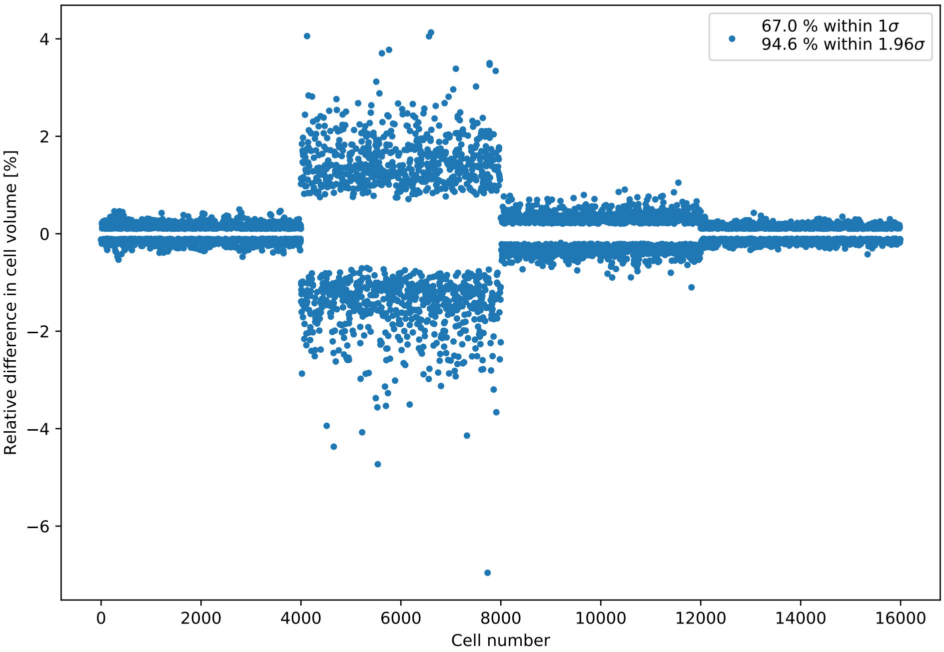

Figure 22. Relative differences in cell volumes between Serpent2 STL and MCNP6 CSG inputs of the 360°. Only the cells that exceed the 1σ error margin have been plotted.

Figure 23 shows the relative difference in flux as a function of the cells exceeding the statistical 1σ error margin. When no boundary conditions have been used in the simulation, the spike-like patterns have not been identified either, as in the 72° simulation. In each layer, the relative difference is concentrated in an interval with small fluctuations. The fluctuations in relative difference are highest in the FW layer, which was observed in the 72° model as well. As with the volume difference, the flux difference fits the expected confidence interval levels better than the 72° model. 68.3 % and 94.6 % of the flux values are within the 1σ and 1.96σ intervals.

The standardized distribution of the cell flux difference is shown in Figure 24. The probability density function fits the expected Gaussian distribution as the confidence intervals suggest. This is also seen from the parameters of the standardized distribution: $\mu = 0.02$ and $\sigma = 1.01$, which differ only in the second decimal place from the expected parameters.

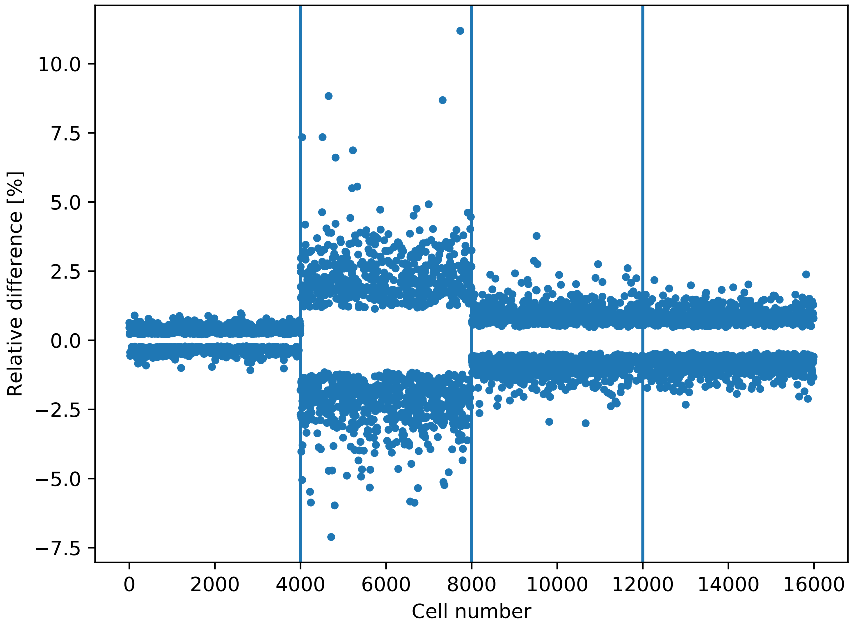

Figure 23. Relative neutron flux difference as a function of cells exceeding the 1σ error margin in the 360° model. 68.3 % and 94.6 % of the cells are within the 1σ and 1.96σ statistical error margin.

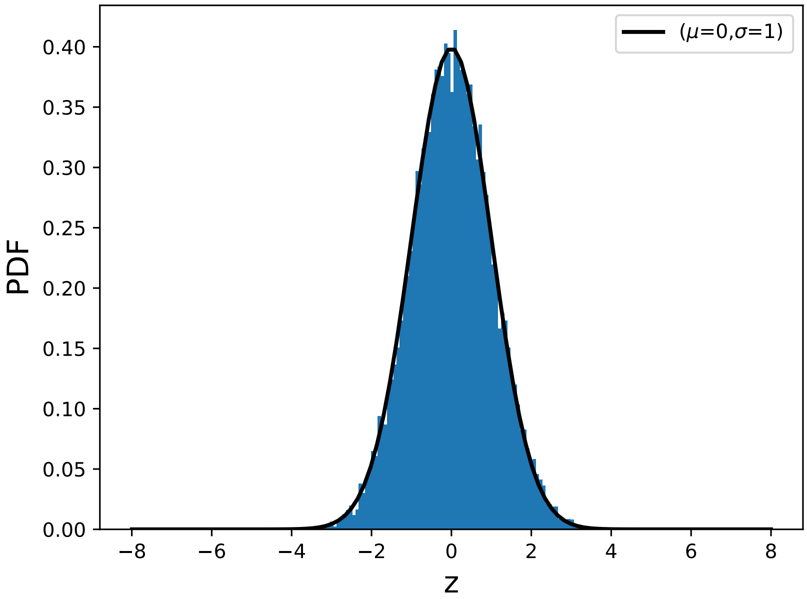

Figure 24. Histogram of the standardized neutron flux difference plotted in the 360° model together with the expected Gaussian probability density function ($\mu = 0, \sigma = 1$). Parameters of the standardized distribution: $\mu = 0.021, \sigma = 1.011$.

4.2 TBR with parameterized blanket thickness

TBR as a function of breeding zone thickness and volume using DCLL and HCPB blankets are shown in Figure 25 and 26. TBR target 1.15 was achieved with the 47.2 cm breeding zone thickness and with full module BZ volume of 1.1×10^9 cm^3 in the DCLL concept. The thickness and volume of the TBR target level were determined by linear interpolation between two nearest points of the target. HCPB blanket shows superior tritium breeding compared to DCLL, since the target TBR could be reached with a thickness of 26.4 cm and a BZ volume of 5.7×10^8 cm^3.

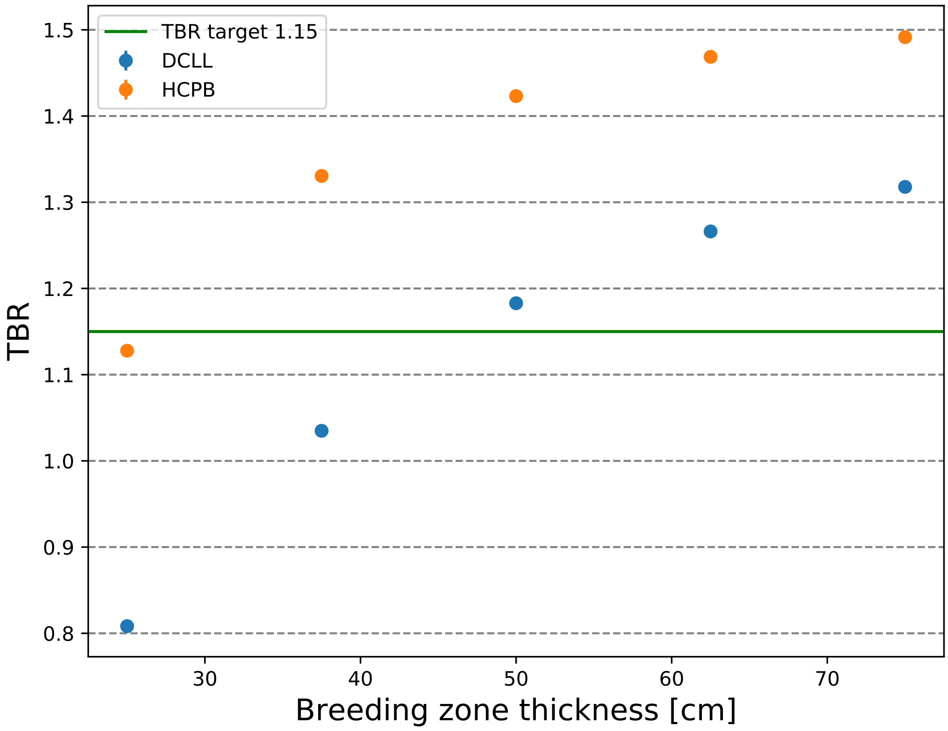

Figure 25. TBR as a function of breeding zone thickness using DCLL and HCPB blanket compositions.

The high TBR capability of the homogenized material composition of the HCPB blanket has been demonstrated in ref. [38] with MCNP. TBRs of 1.368 and 1.421–1.424 have been calculated with MCNP using models similar to those in this work. The corresponding TBR 1.423 with Serpent was obtained with a BZ thickness of 50 cm. Higher MCNP results were calculated with similar radial thicknesses and material compositions of the layers, excluding the BSS, which was 18 cm thicker. Furthermore, a simplified neutron source and reflective boundary condition were used together with a limited 4° simulation sector. Respectively, TBR 1.368 has been obtained with MCNP using a 36° sector with reflective boundary condition. In this calculation, the same neutron source routine was used for the 36° model, which was applied for the 72° model in Serpent2. Additionally, the MCNP model contained varying thicknesses of the BSS and divertor openings. According to the reference, the TBR difference between MCNP models is due to the divertor opening and different geometries. The divertor opening has a decreasing effect on BZ volume and TBR. As a similar neutron source, layer thicknesses, and material compositions have been studied with Serpent2, the TBR result is comparable to the MCNP results.

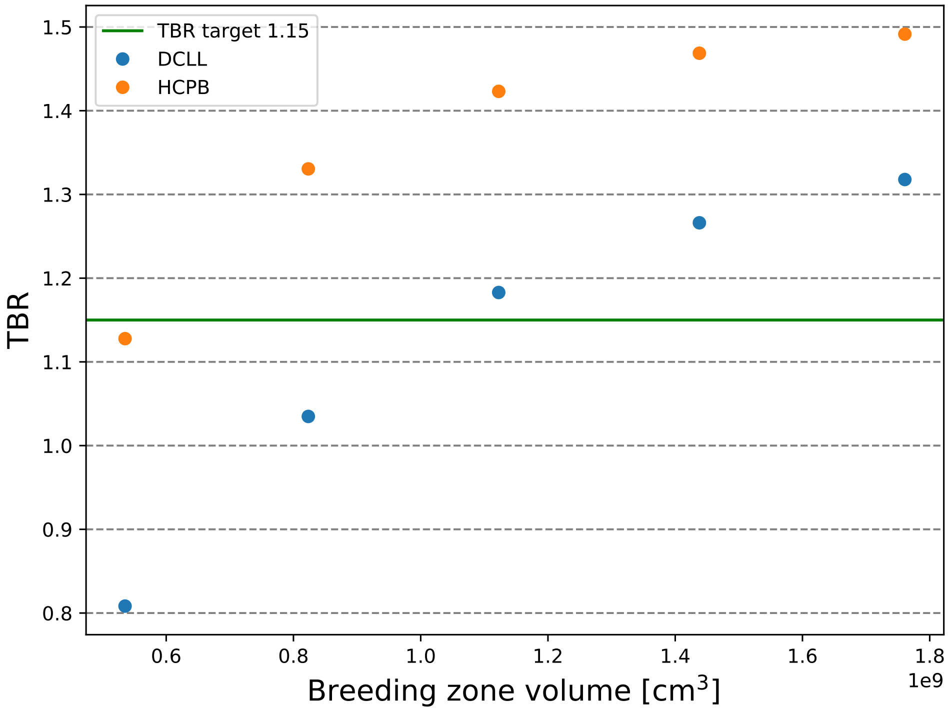

Figure 26. TBR as a function of breeding zone volume using DCLL and HCPB blanket compositions.

4.3 Neutron shielding with parameterized blanket thickness

Figures 27 and 28 show the fast neutron flux to coil winding packs with five BB thicknesses using DCLL and HCPB material compositions. The fast-flux limit 1×10^9 1/cm^{2}s [18] was exceeded with the five thicknesses of the BB in the HCBP model. In turn, the fast-flux was below the limit using the DCLL with the 75 cm thickness of the BB. With the HCPB, the fast-flux is higher by about a factor of 2 for all thicknesses. Therefore, the DCLL blanket shows better neutron shielding of the coils by varying the BZ thickness.

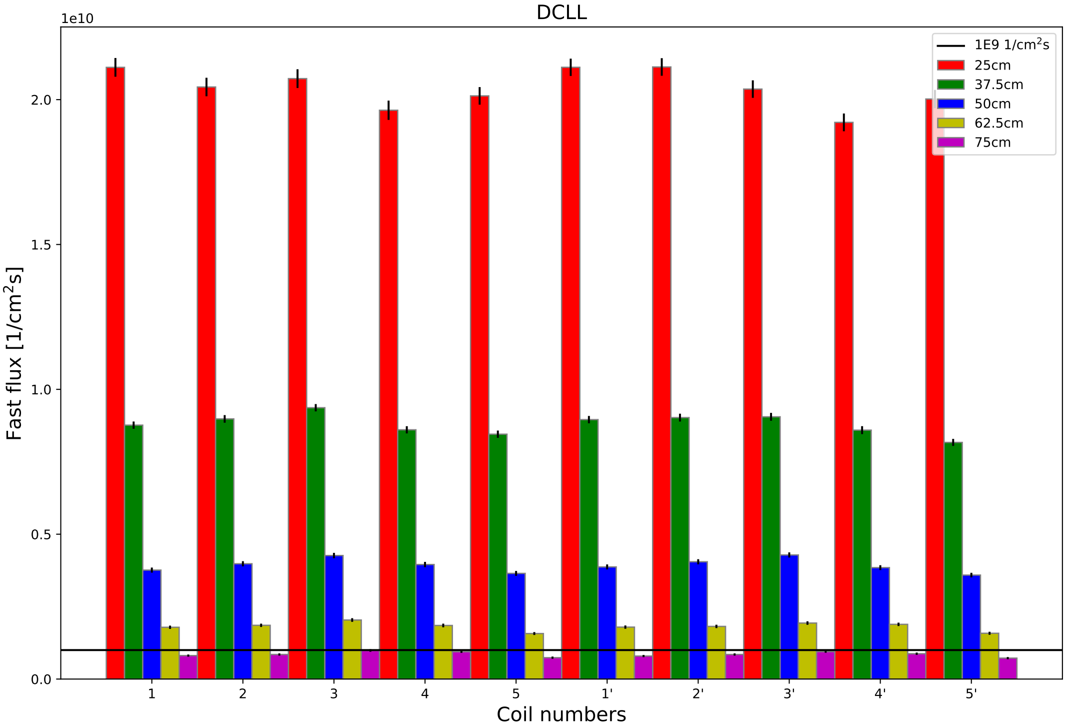

Figure 27. Fast neutron flux to the winding packs of the coils using DCLL blanket.

Figure 29 shows the radial fast neutron flux profiles between the DCLL and HCPB compositions with BZ and BSS thicknesses of 50 cm and 12 cm. The profile supports the better neutron shielding performance of the DCLL, as the fast-flux of the DCLL is lower at the end of the VV. However, this blanket configuration shows insufficient neutron shielding with both blanket compositions. The radial profiles between HCPB and DCLL show similar behavior with the profile calculated in ref. [18]. According to the ref. [18], LiPb-based blankets without water included

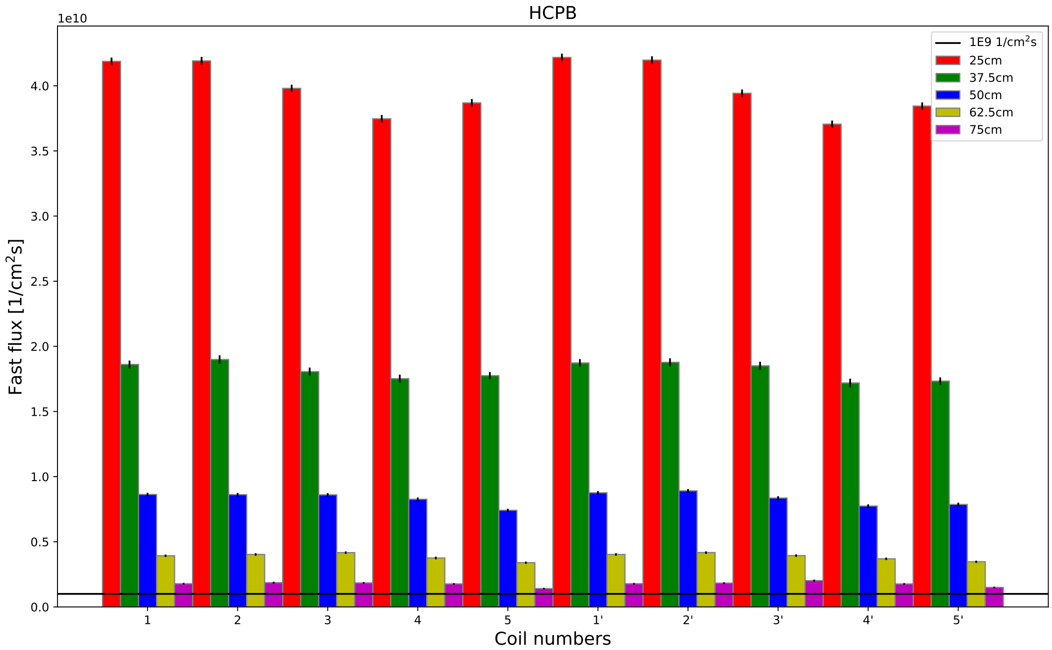

Figure 28. Fast neutron flux to the winding packs of the coils using HCPB blanket.

have 2-3 times higher fast neutron flux at the FW than HCPB. In Figure 29, the DCLL fast-flux is approximately 3 times higher than the HCPB. The differences between HCPB and DCLL profiles arise from neutron scattering and moderation characteristics of lead and beryllium. The higher fast-flux in the FW and blanket with DCLL composition indicates that lead causes more neutron multiplication than beryllium. Although the fast-flux is higher with the DCLL composition at the beginning of the profile, it is, nevertheless, lower at the end of the VV. This is due to the higher decrease in fast-flux in the BSS and VV layers of the DCLL.

The radial profile between HCPB and DCLL in Figure 29 shows that the largest decrease in the fast neutron flux occurs in the VV. This is supported by the radial profiles of HCPB composition with five BZ thicknesses from 25 cm to 75 cm in Figure 30. The profiles of the HCPB composition start at the end of the BZ. Thus, the fast-flux in the BZ and FW is shown on the negative x-axis. The positive x-axis shows the fast-flux at the corresponding positions of the BSS and VV layers at all thicknesses of the BZ. Variation in profile length according to the thicknesses of the BZ is seen on the negative x-axis. The highest decrease in fast-flux in the VV is due to the moderation of neutrons, especially in water but also in steel. Water is an

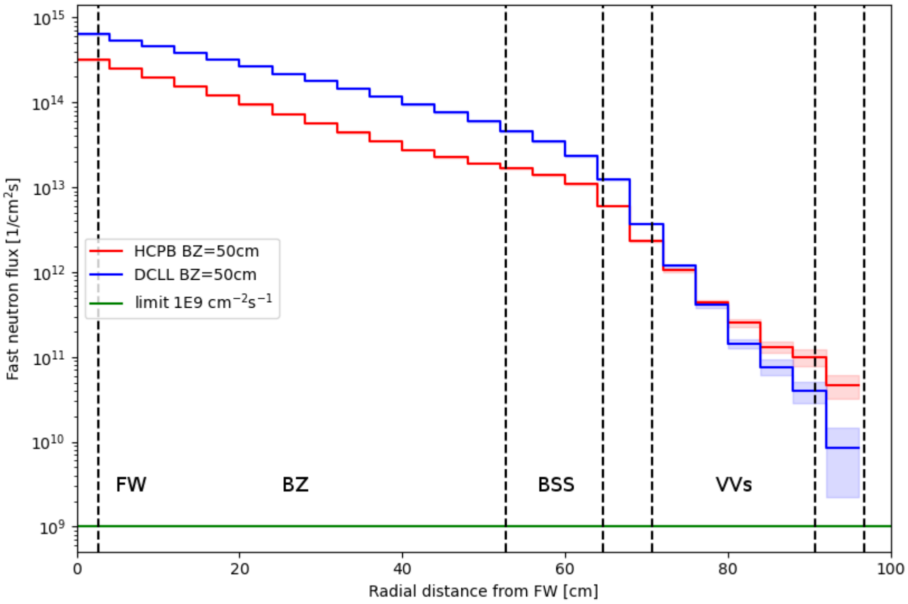

Figure 29. Radial profile of the fast neutron flux between HCPB and DCLL with the BZ thickness of 50 cm. The profile has 4 cm radial binning, perpendicular area A = 20 cm × 20 cm.

efficient neutron moderator because of its low mass. Therefore, the neutron energy can be attenuated and the fast-flux reduced by adding more water to the blanket or VVs. This favors the WCLL candidate in neutron shielding issues [18].

Figure 30 shows the fast-flux at the end of the BZ, BSS, VV inner, and VV shield as a function of the BZ thickness. The decrease in fast-flux as a function of BZ thickness is linear on a logarithmic scale. This means that the decrease in fast-flux is exponential on a linear scale. An exponential function $a \exp(bx)$ with free parameters a and b is fitted to the data.

Figures 31 and 32 show the fast neutron flux to coil winding packs with different BZ and BSS configurations of the DCLL and HCPB compositions. In Figure 31, the DCLL configurations: BZ = 50 cm, BSS = 42.5cm; BZ = 75 cm, BSS = 12 cm are compared. The first configuration resulted in lower flux to the coils with 5.5 cm thicker total thickness of the blanket system. The fast-flux is within the 1×10^9 1/cm^{2}s limit in all coils with both configurations in the DCLL. In Figure 32, the same blanket configurations are compared with the material composition of the HCPB. In addition, the fast-flux was calculated with the BZ thickness of 26.4 cm corresponding to the TBR target level, and BSS thickness of 42.5 cm. With the

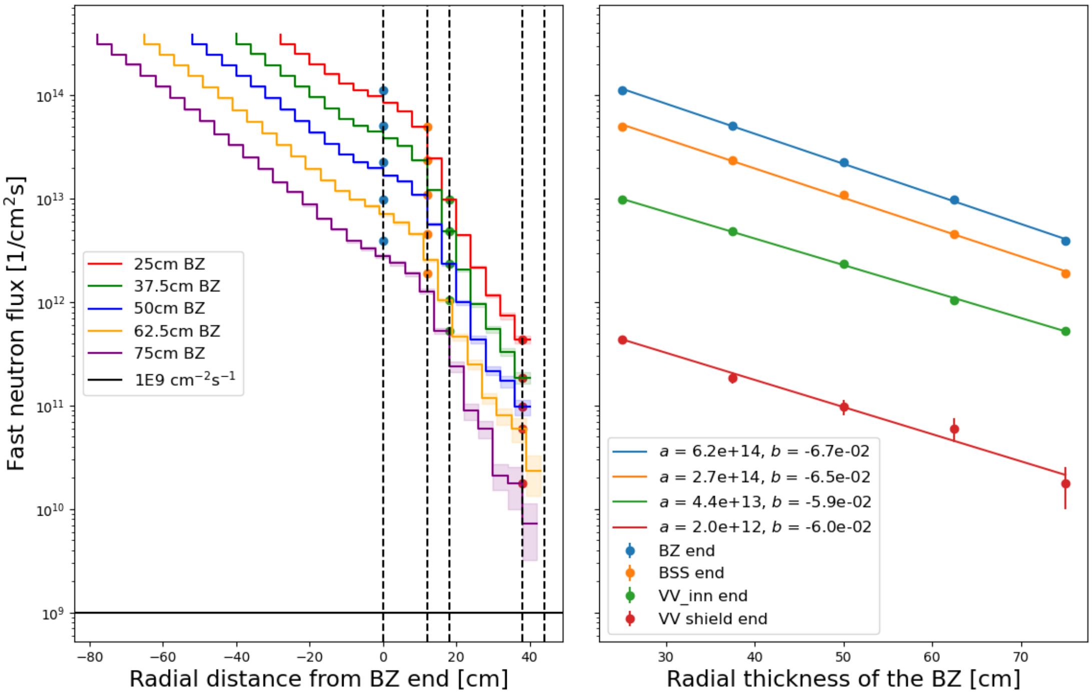

Figure 30. Radial profiles of HCPB with thicknesses of the BZ from 25 cm to 75 cm on the left. On the right, the fast-flux at the end of layers plotted as a function of BZ thickness. Exponential function $a \exp(bx)$ with parameters a and b fitted to the data.

HCPB composition, the error margins of the fast flux overlap with the limit only in coils 4, 4′, 5 and 5′ using the BZ = 50 cm and BSS = 42.5 cm configuration. The fast flux exceed the limit in all of the coils with BZ configurations of 26.4 cm and 75 cm. These results indicate a worse neutron shielding of the coils with the HCPB blanket composition.

With both blanket compositions, the magnitude of the fast flux is ordered according to the total thickness of the BZ and BSS layer. Lower total thickness of the blanket (BZ + BSS) yields higher fast flux. This is supported by the radial profile in Figure 29, which shows that the decrease rate of the fast-flux is nearly constant between BZ and BSS layers in logarithmic scale. However, there is a difference between DCLL and HCPB in the decrease of fast-flux in the BSS shown in Figure 29. The DCLL blanket has a higher decrease in fast flux in the BSS and VV layers. Therefore, the fast-flux of the DCLL is lower at the end of the VV.

Figure 33 shows the radial profiles of the DCLL with the blanket configurations: BZ = 75 cm, BSS = 12 cm; BZ = 50 cm, BSS = 42.5 cm. The statistical error

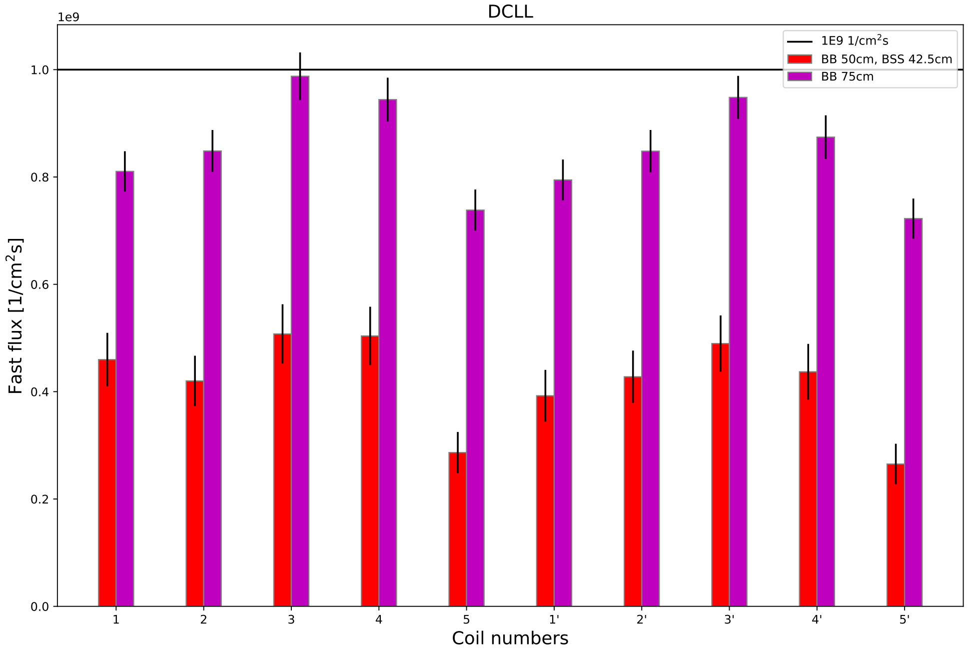

Figure 31. Fast neutron flux to the winding packs of the coils with the DCLL blanket configurations: BB (BZ) = 50 cm, BSS = 42.5 cm (red); BB (BZ) = 75 cm, BSS = 12 cm (magenta).

margin of the latter profile overlaps with the 1×10^9 $1/\text{cm}^2\text{s}$ fast flux limit that is seen as a black horizontal line in the figure. The profiles support the fact that the fast-flux below the limit can be reached, as shown in Figure 31, when the shielding of the coil jacket case is also taken into account.

Radial profiles of slow, fast, and total fluxes with the HCPB composition are shown in Figure 34. At the FW, fast-flux is roughly 2 orders of magnitude higher than slow flux. The slow flux passes the fast flux about 20 cm from the FW. In the VV shield layer, the slow flux is approximately equal to the total flux. The profile is in line with the profile calculated in ref. [38].

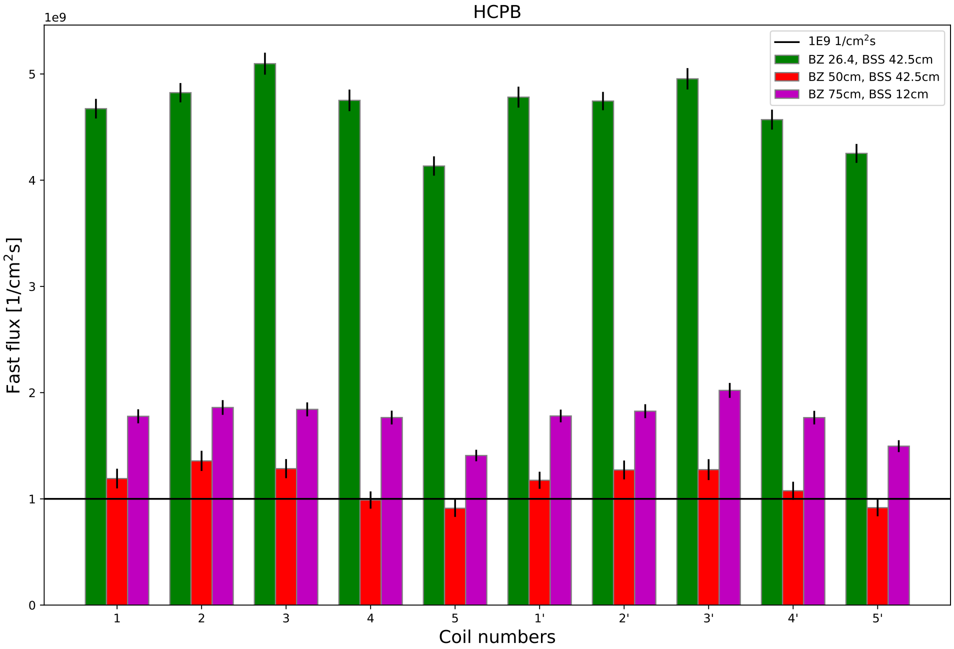

Figure 32. Fast neutron flux to the winding packs of the coils with the HCPB blanket configurations: BZ = 26.4 cm, BSS = 42.5 cm (green); BZ = 50 cm, BSS = 42.5 cm (red); BZ = 75 cm, BSS = 12 cm (magenta).

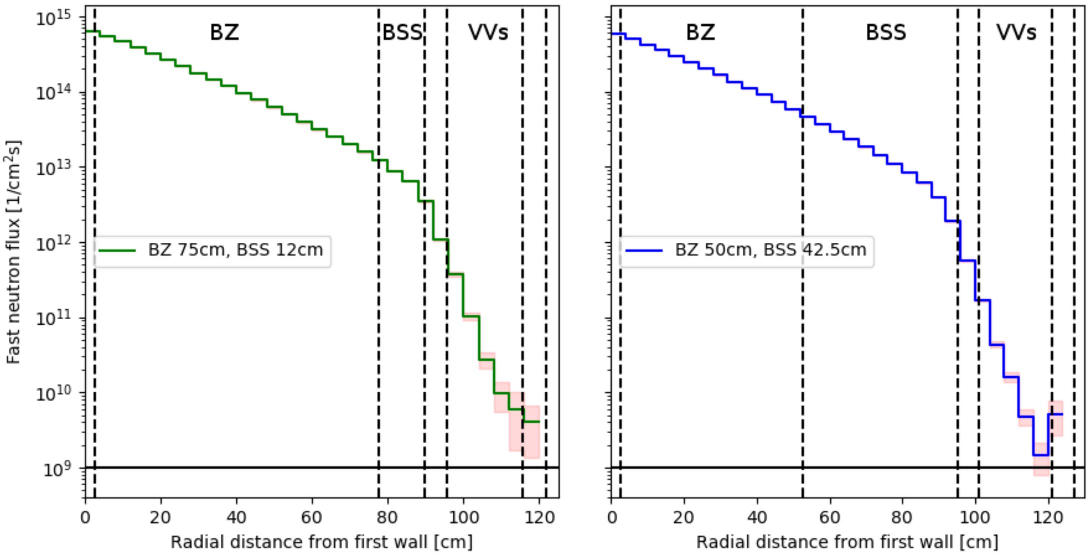

Figure 33. Radial profiles of the DCLL configurations: BZ = 75 cm, BSS = 12 cm; BZ = 50 cm, BSS = 42.5 cm. Profiles have 4 cm radial bins.

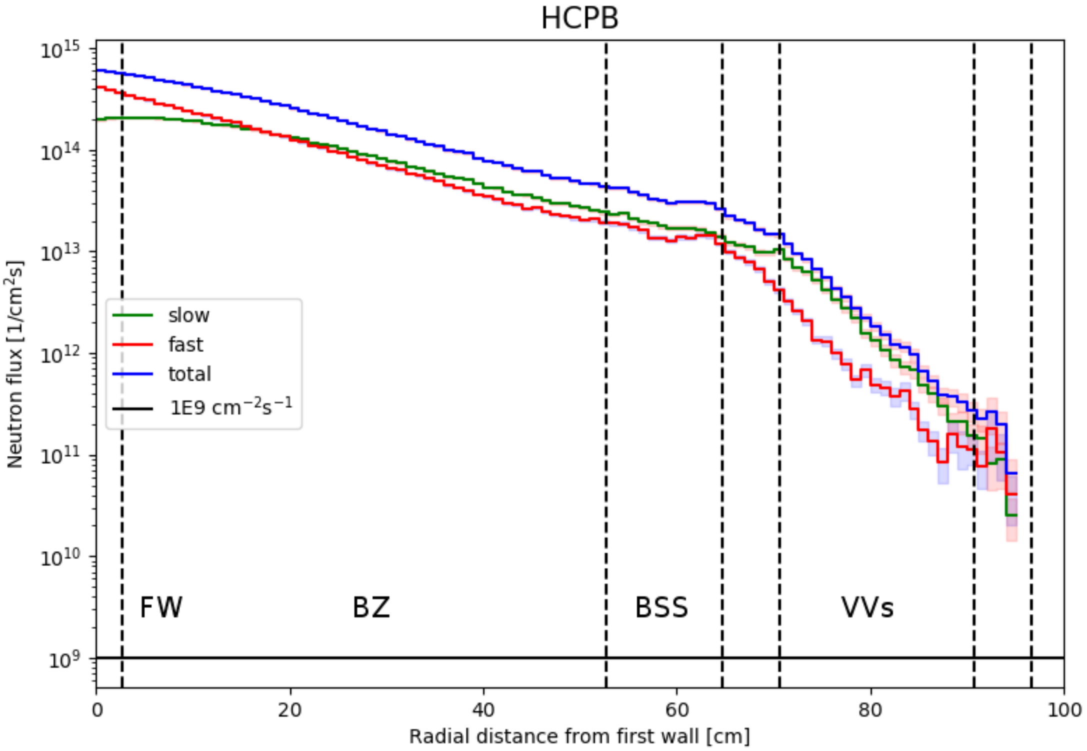

Figure 34. Radial profile of the slow ($E \in [1 \times 10^{-9}, 0.1]$ MeV), fast ($E \in [0.1, 20]$ MeV) and total flux with the HCPB blanket composition.

5 Summary, conclusions, and outlook

In this work, 72° and 360° STL models of HELIAS were constructed applying the parametric HeliasGeom tool. A neutron flux benchmark of the models was performed on the MCNP6 CSG models. Compatibility of models with an average relative neutron flux difference of less than 1 % was achieved. The 360° model performed better in the benchmark, as 67 % and 94.6 % of the neutron flux values were within 1σ and 1.96σ statistical error margins. With the 72° model, the corresponding percentages were 65.5 % and 93.3 % with approximately equivalent statistical uncertainty level. Worse agreement with the 72° model is due to a larger systematic volume difference and deviations in neutron flux at the boundaries of the simulation sector. In the 360° model, 94.6 % of the cell volumes were within 1.96σ, whereas in the 72° model only 81.2 %. This indicates that 72° and 360° STP CAD models were converted to STL and CSG formats with different accuracy. The deviations at the sector ends may be due to differences between the codes in handling the boundary conditions. Nevertheless, the benchmark results show that Serpent2 can be used for fusion neutron transport studies.

A parametric study of tritium breeding and neutron shielding of the full-module coil system was carried out for homogenized HCPB and DCLL blanket compositions. The HCPB blanket performed better in tritium breeding obtaining TBR = 1.423 with BZ thickness of 50 cm. The corresponding TBR with the DCLL composition was 1.266. TBR target 1.15 was reached with BZ thicknesses of 47.2 and 26.4 cm in the DCLL and HCPB applying linear interpolation. In neutron shielding of the coils, the DCLL composition performed better than the HCPB. The fast neutron flux was below the limit in all coils with blanket configurations (BZ = 75 cm, BSS = 12 cm and BZ = 50 cm, BSS = 42.5). With the HCPB composition, the error margin of the fast-flux overlapped the flux limit only in four of the coils with a BZ thickness of 50 cm, and a BSS thickness of 42.5 cm.

The neutron shielding results point out that with the DCLL blanket satisfactory shielding of the coils could potentially be achieved on the outboard side of the HELIAS design. However, approximations and idealizations of the model must be noted. Firstly, the material composition of the blanket is fully homogenized, so heterogeneous models would be required for a more detailed analysis. Secondly, there are no divertor openings or ports, which would reduce neutron shielding at least at specific locations. The results with inboard thickness configuration point out that the shielding of the coils must be improved. Materials with better neutron shielding capability should be added to the blanket system. With the high TBR of HCPB, it could be possible to reduce the thickness of the breeding zone for the use of shielding materials. However, the TBR capability itself needs to be verified with a more detailed blanket composition.

The next steps towards more comprehensive HELIAS neutron transport modeling would include creating a heterogeneous breeding blanket, a blanket with varying thickness between the inboard and outboard sides of the HELIAS, divertor openings, and ports. Comprehensive parametric modeling of different candidates would aim to find the most suitable configuration and composition for the blanket system of HELIAS. To perform parametric modeling efficiently with Serpent, geometry tools would have to be developed to directly generate STL geometries. With the STL geometry approach, the quality of the triangle meshes is a decisive factor when moving to more detailed calculations with more complex geometries.

References

[1] J. Wesson and D. Campbell. *Tokamaks*. International series of monographs on physics. Clarendon Press, 2004. ISBN: 9780198509226.

[2] U. Fischer et al. “Required, achievable and target TBR for the European DEMO”. In: *Fusion Engineering and Design* 155 (2020), p. 111553. ISSN: 0920-3796. DOI: `https://doi.org/10.1016/j.fusengdes.2020.111553`. URL: `https://www.sciencedirect.com/science/article/pii/S0920379620301010`.

[3] J. Leppänen et al. “The Serpent Monte Carlo code: Status, development and applications in 2013.” In: *Ann. Nucl. Energy* 82(8-14) (2015), pp. 142–150. DOI: `10.1016/j.anucene.2014.08.0241`. URL: `https://www.sciencedirect.com/science/article/pii/S0306454914004095` (visited on 08/24/2022).

[4] W. C. J. (editor). *MCNP Users Manual - Code Version 6.2*. LA-UR-17-29981. (2017). URL: `https://mcnp.lanl.gov/manual.html`.

[5] E. A. Azizov. “Tokamaks: from A D Sakharov to the present (the 60-year history of tokamaks)”. In: *Physics-Uspekhi* 55.2 (Feb. 2012), pp. 190–203. DOI: `10.3367/ufne.0182.201202j.0202`. URL: `https://doi.org/10.3367/ufne.0182.201202j.0202`.

[6] L. Spitzer. “The Stellarator Concept”. In: *The Physics of Fluids* 1.253 (1958). DOI: `10.1063/1.1705883`.

[7] Y. Wu. *Fusion Neutronics*. Hefei, China: Springer Singapore, 2017.

[8] *IAEA Nuclear Data Services*. URL: `https://www-nds.iaea.org/` (visited on 08/09/2022).

[9] C. Nordborg et al. “Gamma-Ray Production Cross Sections of Neutron-Induced Reactions in Oxygen”. In: *Nuclear Science and Engineering* 66.1 (1978), pp. 75–83. DOI: `10.13182/NSE78-A15189`. eprint: `https://doi.org/10.13182/NSE78-A15189`. URL: `https://doi.org/10.13182/NSE78-A15189`.

[10] F. Warmer et al. “From W7-X to a HELIAS fusion power plant: On engineering considerations for next-step stellarator devices”. In: *Fusion Engineering and Design* 123 (2017). Proceedings of the 29th Symposium on Fusion Technology (SOFT-29) Prague, Czech Republic, September 5-9, 2016, pp. 47–53. ISSN: 0920-3796. DOI: `https://doi.org/10.1016/j.fusengdes.2017.05.034`. URL: `https://www.sciencedirect.com/science/article/pii/S0920379617305781`.

[11] *NuDAT2-Nuclear Structure and Decay Data.* URL: `https://www.nndc.bnl.gov/nudat2/` (visited on 07/14/2021).

[12] F. Schauer, K. Egorov, and V. Bykov. “HELIAS 5-B magnet system structure and maintenance concept”. In: *Fusion Engineering and Design* 88.9 (2013). Proceedings of the 27th Symposium On Fusion Technology (SOFT-27); Liège, Belgium, September 24-28, 2012, pp. 1619–1622. ISSN: 0920-3796. DOI: `https://doi.org/10.1016/j.fusengdes.2013.01.035`. URL: `https://www.sciencedirect.com/science/article/pii/S0920379613000446`.

[13] C. Day and T. Giegerich. “The Direct Internal Recycling concept to simplify the fuel cycle of a fusion power plant”. In: *Fusion Engineering and Design* 88.6 (2013). Proceedings of the 27th Symposium On Fusion Technology (SOFT-27); Liège, Belgium, September 24-28, 2012, pp. 616–620. ISSN: 0920-3796. DOI: `https://doi.org/10.1016/j.fusengdes.2013.05.026`. URL: `https://www.sciencedirect.com/science/article/pii/S0920379613004663`.

[14] A. Del Nevo et al. “Recent progress in developing a feasible and integrated conceptual design of the WCLL BB in EUROfusion project”. In: *Fusion Engineering and Design* 146 (2019). SI:SOFT-30, pp. 1805–1809. ISSN: 0920-3796. DOI: `https://doi.org/10.1016/j.fusengdes.2019.03.040`. URL: `https://www.sciencedirect.com/science/article/pii/S0920379619303503`.

[15] F. A. Hernández et al. “An enhanced, near-term HCPB design as driver blanket for the EU DEMO”. In: *Fusion Engineering and Design* 146 (2019). SI:SOFT-30, pp. 1186–1191. ISSN: 0920-3796. DOI: `https://doi.org/10.1016/j.fusengdes.2019.02.037`. URL: `https://www.sciencedirect.com/science/article/pii/S0920379619302121`.

[16] J. Aubert et al. "Status of the EU DEMO HCLL breeding blanket design development". In: *Fusion Engineering and Design* 136 (2018). Special Issue: Proceedings of the 13th International Symposium on Fusion Nuclear Technology (ISFNT-13), pp. 1428–1432. ISSN: 0920-3796. DOI: `https://doi.org/10.1016/j.fusengdes.2018.04.133`. URL: `https://www.sciencedirect.com/science/article/pii/S092037961830423X`.

[17] D. Rapisarda et al. "Status of the engineering activities carried out on the European DCLL". In: *Fusion Engineering and Design* 124 (2017). Proceedings of the 29th Symposium on Fusion Technology (SOFT-29) Prague, Czech Republic, September 5-9, 2016, pp. 876–881. ISSN: 0920-3796. DOI: `https://doi.org/10.1016/j.fusengdes.2017.02.022`. URL: `https://www.sciencedirect.com/science/article/pii/S0920379617301059`.

[18] U. Fischer et al. "Neutronic performance issues of the breeding blanket options for the European DEMO fusion power plant". In: *Fusion Engineering and Design* 109-111 (2016), pp. 1458–1463. DOI: `10.1016/j.fusengdes.2015.11.051`.

[19] G. Federici et al. "An overview of the EU breeding blanket design strategy as an integral part of the DEMO design effort". In: *Fusion Engineering and Design* 141 (2019), pp. 30–42. ISSN: 0920-3796. DOI: `https://doi.org/10.1016/j.fusengdes.2019.01.141`. URL: `https://www.sciencedirect.com/science/article/pii/S0920379619301590`.

[20] J. J. Duderstadt and L. J. Hamilton. *Nuclear reactor analysis.* United States: John Wiley and Sons, Inc., 1976.

[21] L. I and K. L. *Monte Carlo Particle Transport Methods: Neutron and Photon Calculations (1st ed.)* Boca Raton: CRC Press, 1991. DOI: `https://doi.org/10.1201/9781351074834`.

[22] S. A. Dupree and S. K. Fraley. *A Monte Carlo Primer: A Practical Approach to Radiation Transport.* Springer, 2002. ISBN: 0-306-46748-8.

[23] J. Leppänen. "Performance of Woodcock delta-tracking in lattice physics applications using the Serpent Monte Carlo reactor physics burnup calculation code." In: *Annals of Nuclear Energy* 37.5 (2010), pp. 715–722. ISSN: 0306-4549. DOI: `https://doi.org/10.1016/j.anucene.2010.01.011`. URL: `https://www.sciencedirect.com/science/article/pii/S0306454910000320`.

[24] E. R. Woodcock et al. *Techniques Used in the GEM Code for Monte Carlo Neutronics Calculations in Reactors and Other Systems of Complex Geometry.* Argonne National Laboratory.: ANL-7050, 1965.

[25] J. Leppänen. "Development of a New Monte Carlo reactor physics code". English. Doctoral thesis. 2007, 228, [8]. ISBN: 978-951-38-7019-5. URL: `https://aaltodoc.aalto.fi/handle/123456789/2743` (visited on 08/25/2021).

[26] J. Leppänen. "On the use of delta-tracking and the collision flux estimator in the Serpent 2 Monte Carlo particle transport code". In: *Annals of Nuclear Energy* 105 (2017), pp. 161–167. ISSN: 0306-4549. DOI: `https://doi.org/10.1016/j.anucene.2017.03.006`. URL: `https://www.sciencedirect.com/science/article/pii/S0306454916311367`.

[27] *Serpent Wiki.* URL: `https://serpent.vtt.fi/mediawiki/index.php/Main_Page` (visited on 11/30/2022).

[28] C. D. Beidler et al. "Physics and Engineering Design for Wendelstein VII-X". In: *Fusion Technology* 17 (1990), pp. 148–168.

[29] G. Grieger et al. "Physics optimization of stellarators". In: *Physics of Fluids B: Plasma Physics* 4.7 (1992), pp. 2081–2091. DOI: `10.1063/1.860481`. eprint: `https://doi.org/10.1063/1.860481`. URL: `https://doi.org/10.1063/1.860481`.

[30] J. Leppänen. "Methodology, applications and performance of the CAD-based geometry type in the serpent 2 Monte Carlo code". In: *Annals of Nuclear Energy* 176 (2022), p. 109259. ISSN: 0306-4549. DOI: `https://doi.org/10.1016/j.anucene.2022.109259`. URL: `https://www.sciencedirect.com/science/article/pii/S0306454922002948`.

[31] N. E. Agency. *JEFF-3.3 nuclear data.* 2017. URL: `https://www.oecd-nea.org/dbdata/jeff/jeff33/index.html`.

[32] *The Message Passing Interface (MPI) Standard.* URL: `https://www.mcs.anl.gov/research/projects/mpi/` (visited on 08/29/2022).

[33] *OpenMP – The OpenMP API specification for parallel programming.* URL: `https://www.openmp.org/` (visited on 08/29/2022).

[34] G. Federici et al. “Overview of the DEMO staged design approach in Europe”. In: *Nuclear Fusion* 59.6 (Apr. 2019), p. 066013. DOI: `10.1088/1741-4326/ab1178`. URL: `https://dx.doi.org/10.1088/1741-4326/ab1178`.

[35] A. Häußler. *HELIAS_CAD_data.stp*. 2017.

[36] F. Warmer. *HELIAS_COIL_HM1.stp*. 2019.

[37] I. Palermo et al. “Development of a HELIAS-type fusion reactor with Dual Coolant Lithium Lead Breeding Blanket: Status and prospects”. In: *32nd Symposium on Fusion Technology (SOFT 2022)*. 2022.

[38] A. Häußler. *Computational approaches for nuclear design analyses of the stellarator power reactor HELIAS*. 2020. DOI: `10.5445/IR/1000124072`. URL: `http://inis.iaea.org/search/search.aspx?orig_q=RN:52073400`.

[39] I. Palermo, F. Warmer, and A. Häußler. “Nuclear design and assessments of helical-axis advanced stellarator with dual-coolant lithium-lead breeding blanket: adaptation from DEMO tokamak reactor”. In: *Nuclear Fusion* 61.7 (June 2021), p. 076019. DOI: `10.1088/1741-4326/abfd71`. URL: `https://dx.doi.org/10.1088/1741-4326/abfd71`.

[40] J. Hubbel and S. Seltzer. *Tables of X-Ray Mass Attenuation Coefficients and Mass Energy-Absorption Coefficients 1 keV to 20 MeV for Elements Z = 1 to 92 and 48 Additional Substances of Dosimetric Interest*. 2004. DOI: `https://dx.doi.org/10.18434/T4D01F`. URL: `https://www.nist.gov/pml/x-ray-mass-attenuation-coefficients`.

[41] *The materials Project*. DOI: `10.17188/1271095`. URL: `https://materialsproject.org/materials/mp-559848/` (visited on 11/30/2022).

A Benchmark material composition

Benchmark FW material (1002)					
Atom density 6.32089E-02 1/barn*cm					
Mass density 1.92500E+01 g/cm3					
Nuclide	a. weight	temp	a. dens	a. frac	m. frac
74180.03c	179.94674	294.0	7.56373E-05	1.19662E-03	1.17410E-03
74182.03c	181.94813	294.0	1.67032E-02	2.64254E-01	2.62164E-01
74183.03c	182.95024	294.0	9.01973E-03	1.42697E-01	1.42348E-01
74184.03c	183.95094	294.0	1.93127E-02	3.05538E-01	3.06458E-01
74186.03c	185.95435	294.0	1.79197E-02	2.83500E-01	2.87451E-01
47107.03c	106.90507	294.0	5.57092E-07	8.81350E-06	5.13748E-06
47109.03c	108.90455	294.0	5.17566E-07	8.18818E-06	4.86225E-06
33075.03c	74.92160	294.0	7.73603E-07	1.22388E-05	4.99978E-06
13027.03c	26.98154	294.0	6.44450E-06	1.01956E-04	1.49997E-05
56130.03c	129.90596	294.0	4.47389E-10	7.07794E-09	5.01348E-09
56132.03c	131.90514	294.0	4.26285E-10	6.74407E-09	4.85051E-09
56134.03c	133.90431	294.0	1.02013E-08	1.61391E-07	1.17836E-07
56135.03c	134.90591	294.0	2.78225E-08	4.40168E-07	3.23782E-07
56136.03c	135.90449	294.0	3.31490E-08	5.24435E-07	3.88624E-07
56137.03c	136.90610	294.0	4.74064E-08	7.49995E-07	5.59867E-07
56138.03c	137.90467	294.0	3.02612E-07	4.78750E-06	3.59990E-06
20040.03c	39.96259	294.0	1.40195E-06	2.21797E-05	4.83296E-06
20042.03c	41.95863	294.0	9.35688E-09	1.48031E-07	3.38671E-08
20043.03c	42.95877	294.0	1.95236E-09	3.08875E-08	7.23499E-09
20044.03c	43.95548	294.0	3.01676E-08	4.77269E-07	1.14388E-07
20046.03c	45.95370	294.0	5.78478E-11	9.15185E-10	2.29315E-10
20048.03c	47.95253	294.0	2.70439E-09	4.27849E-08	1.11868E-08
48106.03c	105.90982	294.0	6.44520E-09	1.01967E-07	5.88841E-08

48108.03c	107.90395	294.0	4.58896E-09	7.25999E-08	4.27147E-08
48110.03c	109.90313	294.0	6.44002E-08	1.01885E-06	6.10552E-07
48111.03c	110.90473	294.0	6.59987E-08	1.04414E-06	6.31409E-07
48112.03c	111.90331	294.0	1.24417E-07	1.96835E-06	1.20102E-06
48113.03c	112.89987	294.0	6.30080E-08	9.96822E-07	6.13641E-07
48114.03c	113.90349	294.0	1.48136E-07	2.34359E-06	1.45553E-06
48116.03c	115.90468	294.0	3.86195E-08	6.10982E-07	3.86129E-07
27059.03c	58.93317	294.0	1.96700E-06	3.11190E-05	9.99974E-06
24050.03c	49.94605	294.0	1.93737E-07	3.06503E-06	8.34717E-07
24052.03c	51.94051	294.0	3.73603E-06	5.91060E-05	1.67395E-05
24053.03c	52.94066	294.0	4.23635E-07	6.70214E-06	1.93467E-06
24054.03c	53.93889	294.0	1.05452E-07	1.66831E-06	4.90661E-07
29063.03c	62.92961	294.0	1.26144E-06	1.99567E-05	6.84775E-06
29065.03c	64.92780	294.0	5.62769E-07	8.90332E-06	3.15200E-06
26054.03c	53.93962	294.0	3.63985E-07	5.75845E-06	1.69363E-06
26056.03c	55.93491	294.0	5.71380E-06	9.03955E-05	2.75698E-05
26057.03c	56.93541	294.0	1.31956E-07	2.08762E-06	6.48094E-07
26058.03c	57.93329	294.0	1.75610E-08	2.77824E-07	8.77611E-08
19039.03c	38.96371	294.0	2.76498E-06	4.37435E-05	9.29346E-06
19040.03c	39.96400	294.0	3.46890E-10	5.48799E-09	1.19587E-09
19041.03c	40.96183	294.0	1.99542E-07	3.15686E-06	7.05079E-07
12024.03c	23.98504	294.0	1.88369E-06	2.98010E-05	3.89740E-06
12025.03c	24.98584	294.0	2.38472E-07	3.77276E-06	5.13992E-07
12026.03c	25.98260	294.0	2.62557E-07	4.15380E-06	5.88481E-07
25055.03c	54.93805	294.0	1.05502E-06	1.66910E-05	4.99987E-06
11023.03c	22.98977	294.0	5.04230E-06	7.97719E-05	9.99973E-06
41093.03c	92.90639	294.0	1.24772E-06	1.97396E-05	9.99973E-06
28058.03c	57.93570	294.0	6.72268E-07	1.06357E-05	3.35981E-06
28060.03c	59.93079	294.0	2.58956E-07	4.09683E-06	1.33875E-06
28061.03c	60.93143	294.0	1.12567E-08	1.78087E-07	5.91666E-08
28062.03c	61.92835	294.0	3.58921E-08	5.67833E-07	1.91741E-07
28064.03c	63.92818	294.0	9.13944E-09	1.44591E-07	5.04008E-08

82204.03c	203.97304	294.0	3.91594E-09	6.19524E-08	6.89024E-08
82206.03c	205.97443	294.0	6.74101E-08	1.06647E-06	1.19774E-06
82207.03c	206.97603	294.0	6.18160E-08	9.77963E-07	1.10369E-06
82208.03c	207.97663	294.0	1.46568E-07	2.31879E-06	2.62954E-06
73181.03c	180.94794	294.0	1.28127E-06	2.02703E-05	1.99995E-05
22046.03c	45.95264	294.0	9.98972E-08	1.58043E-06	3.95994E-07
22047.03c	46.95176	294.0	9.00892E-08	1.42526E-06	3.64880E-07
22048.03c	47.94795	294.0	8.92656E-07	1.41223E-05	3.69215E-06
22049.03c	48.94787	294.0	6.55082E-08	1.03638E-06	2.76602E-07
22050.03c	49.94479	294.0	6.27233E-08	9.92318E-07	2.70237E-07
30064.03c	63.92914	294.0	4.35917E-07	6.89645E-06	2.40396E-06
30066.03c	65.92604	294.0	2.45840E-07	3.88933E-06	1.39809E-06
30067.03c	66.92714	294.0	3.58167E-08	5.66639E-07	2.06782E-07
30068.03c	67.92485	294.0	1.63569E-07	2.58775E-06	9.58416E-07
30070.03c	69.92533	294.0	5.40795E-09	8.55569E-08	3.26207E-08
40090.03c	89.90472	294.0	3.26898E-07	5.17170E-06	2.53524E-06
40091.03c	90.90567	294.0	7.12886E-08	1.12783E-06	5.59031E-07
40092.03c	91.90506	294.0	1.08966E-07	1.72390E-06	8.63882E-07
40094.03c	93.90632	294.0	1.10427E-07	1.74702E-06	8.94531E-07
40096.03c	95.90827	294.0	1.77903E-08	2.81453E-07	1.47186E-07
42092.03c	91.90682	294.0	1.75526E-06	2.77691E-05	1.39160E-05
42094.03c	93.90510	294.0	1.10534E-06	1.74871E-05	8.95385E-06
42095.03c	94.90589	294.0	1.91350E-06	3.02727E-05	1.56656E-05
42096.03c	95.90468	294.0	2.01377E-06	3.18590E-05	1.66600E-05
42097.03c	96.90602	294.0	1.15970E-06	1.83471E-05	9.69440E-06
42098.03c	97.90541	294.0	2.94636E-06	4.66131E-05	2.48839E-05
42100.03c	99.90748	294.0	1.18628E-06	1.87676E-05	1.02237E-05
6000.03c	12.00110	294.0	2.89545E-05	4.58076E-04	2.99752E-05
1001.03c	1.00782	294.0	5.74975E-05	9.09642E-04	4.99872E-06
1002.03c	2.01410	294.0	6.61295E-09	1.04621E-07	1.14895E-09
7014.03c	14.00307	294.0	4.12300E-06	6.52281E-05	4.98037E-06
7015.03c	14.99986	294.0	1.50625E-08	2.38298E-07	1.94900E-08

8016.03c	15.99492	294.0	1.44555E-05	2.28694E-04	1.99453E-05
8017.03c	16.99913	294.0	5.50648E-09	8.71155E-08	8.07469E-09
8018.03c	17.99916	294.0	2.97060E-08	4.69966E-07	4.61235E-08
15031.03c	30.97376	294.0	7.48516E-06	1.18419E-04	1.99996E-05
16032.03c	31.97208	294.0	1.71705E-06	2.71647E-05	4.73565E-06
16033.03c	32.97146	294.0	1.35571E-08	2.14481E-07	3.85595E-08
16034.03c	33.96787	294.0	7.68237E-08	1.21539E-06	2.25107E-07
16036.03c	35.96709	294.0	1.80761E-10	2.85974E-09	5.60836E-10
14028.03c	27.97734	294.0	7.61278E-06	1.20438E-04	1.83728E-05
14029.03c	28.97693	294.0	3.86737E-07	6.11839E-06	9.66703E-07
14030.03c	29.97349	294.0	2.55238E-07	4.03801E-06	6.59945E-07
sum			6.32089E-02	1.00000E+00	1.00000E+00

Benchmark EUROFER steel (1001)					
Atom density 8.48229E-02 1/barn*cm					
Mass density 7.87000E+00 g/cm3					
Nuclide	a. weight	temp	a. dens	a. frac	m. frac
26054.03c	53.93962	294.0	4.40458E-03	5.19268E-02	5.01296E-02
26056.03c	55.93491	294.0	6.91426E-02	8.15141E-01	8.16037E-01
26057.03c	56.93541	294.0	1.59680E-03	1.88251E-02	1.91829E-02
26058.03c	57.93329	294.0	2.12505E-04	2.50528E-03	2.59764E-03
6000.03c	12.00110	294.0	4.34525E-06	5.12273E-05	1.10032E-05
25055.03c	54.93805	294.0	3.45445E-04	4.07254E-03	4.00436E-03
24050.03c	49.94605	294.0	3.56823E-04	4.20668E-03	3.76041E-03
24052.03c	51.94051	294.0	6.88098E-03	8.11217E-02	7.54115E-02
24053.03c	52.94066	294.0	7.80248E-04	9.19855E-03	8.71572E-03
24054.03c	53.93889	294.0	1.94220E-04	2.28972E-03	2.21044E-03
23050.03c	49.94716	294.0	4.65683E-07	5.49006E-06	4.90775E-06
23051.03c	50.94397	294.0	1.85807E-04	2.19053E-03	1.99727E-03
73181.03c	180.94794	294.0	3.14643E-05	3.70942E-04	1.20131E-03
74180.03c	179.94674	294.0	3.40660E-07	4.01613E-06	1.29344E-05
74182.03c	181.94813	294.0	7.52291E-05	8.86896E-04	2.88812E-03

74183.03c	182.95024	294.0	4.06237E-05	4.78923E-04	1.56817E-03
74184.03c	183.95094	294.0	8.69821E-05	1.02546E-03	3.37608E-03
74186.03c	185.95435	294.0	8.07081E-05	9.51489E-04	3.16668E-03
7014.03c	14.00307	294.0	1.01250E-04	1.19366E-03	2.99157E-04
7015.03c	14.99986	294.0	3.69894E-07	4.36078E-06	1.17070E-06
22046.03c	45.95264	294.0	1.63547E-06	1.92810E-05	1.58575E-05
22047.03c	46.95176	294.0	1.47489E-06	1.73879E-05	1.46115E-05
22048.03c	47.94795	294.0	1.46141E-05	1.72290E-04	1.47851E-04
22049.03c	48.94787	294.0	1.07247E-06	1.26436E-05	1.10764E-05
22050.03c	49.94479	294.0	1.02688E-06	1.21061E-05	1.08215E-05
15031.03c	30.97376	294.0	7.65891E-06	9.02930E-05	5.00544E-05
14028.03c	27.97734	294.0	7.78956E-05	9.18332E-04	4.59834E-04
14029.03c	28.97693	294.0	3.95715E-06	4.66519E-05	2.41945E-05
14030.03c	29.97349	294.0	2.61163E-06	3.07893E-05	1.65170E-05
16032.03c	31.97208	294.0	7.02767E-06	8.28511E-05	4.74093E-05
16033.03c	32.97146	294.0	5.54875E-08	6.54157E-07	3.86024E-07
16034.03c	33.96787	294.0	3.14429E-07	3.70688E-06	2.25357E-06
16036.03c	35.96709	294.0	7.39832E-10	8.72209E-09	5.61461E-09
28058.03c	57.93570	294.0	5.50303E-06	6.48767E-05	6.72712E-05
28060.03c	59.93079	294.0	2.11975E-06	2.49903E-05	2.68050E-05
28061.03c	60.93143	294.0	9.21439E-08	1.08631E-06	1.18465E-06
28062.03c	61.92835	294.0	2.93804E-07	3.46374E-06	3.83909E-06
28064.03c	63.92818	294.0	7.48130E-08	8.81991E-07	1.00914E-06
42092.03c	91.90682	294.0	3.59201E-07	4.23472E-06	6.96574E-06
42094.03c	93.90510	294.0	2.26201E-07	2.66674E-06	4.48192E-06
42095.03c	94.90589	294.0	3.91586E-07	4.61652E-06	7.84155E-06
42096.03c	95.90468	294.0	4.12105E-07	4.85842E-06	8.33929E-06
42097.03c	96.90602	294.0	2.37325E-07	2.79789E-06	4.85262E-06
42098.03c	97.90541	294.0	6.02954E-07	7.10839E-06	1.24558E-05
42100.03c	99.90748	294.0	2.42764E-07	2.86201E-06	5.11757E-06
29063.03c	62.92961	294.0	5.16292E-06	6.08670E-05	6.85538E-05
29065.03c	64.92780	294.0	2.30334E-06	2.71547E-05	3.15551E-05

41093.03c	92.90639	294.0	2.55339E-06	3.01026E-05	5.00545E-05
13027.03c	26.98154	294.0	1.75842E-05	2.07305E-04	1.00109E-04
5010.03c	10.01294	294.0	1.74666E-06	2.05919E-05	3.69022E-06
5011.03c	11.00928	294.0	7.03053E-06	8.28849E-05	1.63316E-05
27059.03c	58.93317	294.0	8.05067E-06	9.49115E-05	1.00109E-04
50112.03c	111.90533	294.0	1.93841E-07	2.28525E-06	4.57697E-06
50114.03c	113.90248	294.0	1.31892E-07	1.55491E-06	3.16981E-06
50115.03c	114.90308	294.0	6.79443E-08	8.01014E-07	1.64727E-06
50116.03c	115.90166	294.0	2.90561E-06	3.42551E-05	7.10574E-05
50117.03c	116.90326	294.0	1.53474E-06	1.80935E-05	3.78568E-05
50118.03c	117.90184	294.0	4.84003E-06	5.70604E-05	1.20406E-04
50119.03c	118.90344	294.0	1.71659E-06	2.02373E-05	4.30667E-05
50120.03c	119.90202	294.0	6.51066E-06	7.67559E-05	1.64715E-04
50122.03c	121.90341	294.0	9.25240E-07	1.09079E-05	2.37986E-05
50124.03c	123.90531	294.0	1.15705E-06	1.36408E-05	3.02499E-05
51121.03c	120.90363	294.0	1.11459E-05	1.31402E-04	2.84339E-04
51123.03c	122.90381	294.0	8.33658E-06	9.82822E-05	2.16189E-04
40090.03c	89.90472	294.0	1.33795E-05	1.57735E-04	2.53807E-04
40091.03c	90.90567	294.0	2.91774E-06	3.43980E-05	5.59653E-05
40092.03c	91.90506	294.0	4.45983E-06	5.25782E-05	8.64847E-05
40094.03c	93.90632	294.0	4.51964E-06	5.32833E-05	8.95530E-05
40096.03c	95.90827	294.0	7.28136E-07	8.58419E-06	1.47350E-05
8016.03c	15.99492	294.0	2.95823E-05	3.48754E-04	9.98379E-05
8017.03c	16.99913	294.0	1.12687E-08	1.32849E-07	4.04185E-08
8018.03c	17.99916	294.0	6.07914E-08	7.16686E-07	2.30874E-07
33075.03c	74.92160	294.0	3.16512E-05	3.73145E-04	5.00356E-04
sum			8.48229E-02	1.00000E+00	1.00000E+00

Benchmark LiPB (1003)					
Atom density 3.27202E-02 1/barn*cm					
Mass density 9.53377E+00 g/cm3					
Nuclide	a. weight	temp	a. dens	a. frac	m. frac
82206.03c	205.97443	294.0	7.02541E-03	2.14712E-01	2.52044E-01
82207.03c	206.97603	294.0	6.08869E-03	1.86084E-01	2.19500E-01
82208.03c	207.97663	294.0	1.44362E-02	4.41202E-01	5.22949E-01
3006.03c	6.01507	294.0	4.65287E-03	1.42202E-01	4.87476E-03
3007.03c	7.01600	294.0	5.16988E-04	1.58003E-02	6.31774E-04
sum			3.27202E-02	1.00000E+00	1.00000E+00

B DCLL and HCPB material compositions

Tungsten armor material					
Atom density 6.34563E-02 1/barn*cm					
Mass density 1.93000E+01 g/cm3					
Nuclide	a. weight	temp	a. dens	a. frac	m. frac
74182.03c	181.94813	294.0	3.37419E-02	5.31734E-01	5.28221E-01
74183.03c	182.95024	294.0	5.79148E-03	9.12672E-02	9.11636E-02
74184.03c	183.95094	294.0	1.24096E-02	1.95561E-01	1.96408E-01
74186.03c	185.95435	294.0	1.15134E-02	1.81437E-01	1.84207E-01
sum			6.34563E-02	1.00000E+00	1.00000E+00

FW material					
Atom density 5.54394E-02 1/barn*cm					
Mass density 5.11800E+00 g/cm3					
Nuclide	a. weight	temp	a. dens	a. frac	m. frac
6000.03c	12.00110	294.0	2.81574E-04	5.07896E-03	1.09640E-03
23051.03c	50.94397	294.0	1.20600E-04	2.17535E-03	1.99340E-03
24052.03c	51.94051	294.0	4.64931E-03	8.38630E-02	7.83521E-02
24053.03c	52.94066	294.0	5.27197E-04	9.50943E-03	9.05562E-03
24054.03c	53.93889	294.0	1.31229E-04	2.36706E-03	2.29660E-03
25055.03c	54.93805	294.0	2.23670E-04	4.03449E-03	3.98691E-03
26054.03c	53.93962	294.0	2.84904E-03	5.13901E-02	4.98611E-02
26056.03c	55.93491	294.0	4.50541E-02	8.12674E-01	8.17661E-01
26057.03c	56.93541	294.0	1.08066E-03	1.94926E-02	1.99630E-02
26058.03c	57.93329	294.0	1.37540E-04	2.48090E-03	2.58530E-03
74182.03c	181.94813	294.0	4.87718E-05	8.79733E-04	2.87921E-03
74183.03c	182.95024	294.0	2.63177E-05	4.74712E-04	1.56220E-03
74184.03c	183.95094	294.0	5.63904E-05	1.01715E-03	3.36561E-03
74186.03c	185.95435	294.0	5.23238E-05	9.43802E-04	3.15691E-03
73181.03c	180.94794	294.0	1.35817E-05	2.44983E-04	7.97378E-04

22048.03c	47.94795	294.0	4.73518E-06	8.54118E-05	7.36651E-05
22047.03c	46.95176	294.0	4.68381E-07	8.44852E-06	7.13521E-06
22046.03c	45.95264	294.0	5.13294E-07	9.25865E-06	7.65301E-06
22049.03c	48.94787	294.0	3.52891E-07	6.36534E-06	5.60441E-06
22050.03c	49.94479	294.0	3.46476E-07	6.24964E-06	5.61461E-06
8016.03c	15.99492	294.0	1.92060E-05	3.46432E-04	9.96722E-05
14028.03c	27.97734	294.0	5.04396E-05	9.09815E-04	4.57861E-04
14029.03c	28.97693	294.0	2.55400E-06	4.60683E-05	2.40120E-05
14030.03c	29.97349	294.0	1.69541E-06	3.05814E-05	1.64880E-05
7014.03c	14.00307	294.0	6.58145E-05	1.18714E-03	2.99021E-04
13027.03c	26.98154	294.0	1.13855E-05	2.05368E-04	9.96722E-05
16032.18c	31.97208	1800.0	4.80416E-06	8.66561E-05	4.98361E-05
15031.03c	30.97376	294.0	4.95900E-06	8.94491E-05	4.98361E-05
27059.03c	58.93317	294.0	2.60632E-06	4.70121E-05	4.98361E-05
28058.03c	57.93570	294.0	1.78151E-06	3.21344E-05	3.34881E-05
28060.03c	59.93079	294.0	6.86402E-07	1.23811E-05	1.33470E-05
28062.03c	61.92835	294.0	9.49933E-08	1.71346E-06	1.90870E-06
28061.03c	60.93143	294.0	2.98323E-08	5.38106E-07	5.89771E-07
28064.03c	63.92818	294.0	2.42327E-08	4.37102E-07	5.02631E-07
29063.03c	62.92961	294.0	1.67192E-06	3.01576E-05	3.41371E-05
29065.03c	64.92780	294.0	7.45223E-07	1.34421E-05	1.56990E-05
41093.03c	92.90639	294.0	3.30653E-07	5.96423E-06	9.96722E-06
42092.03c	91.90682	294.0	5.08859E-08	9.17865E-07	1.51740E-06
42094.03c	93.90510	294.0	3.06951E-08	5.53670E-07	9.35222E-07
42095.03c	94.90589	294.0	5.20253E-08	9.38417E-07	1.60200E-06
42096.03c	95.90468	294.0	5.36141E-08	9.67077E-07	1.66830E-06
42097.03c	96.90602	294.0	3.02423E-08	5.45503E-07	9.50872E-07
42098.03c	97.90541	294.0	7.52756E-08	1.35780E-06	2.39120E-06
42100.03c	99.90748	294.0	2.91058E-08	5.25002E-07	9.43482E-07
5010.03c	10.01294	294.0	5.65448E-07	1.01994E-05	1.83700E-06
5011.03c	11.00928	294.0	2.27608E-06	4.10553E-05	8.13021E-06
2004.03c	4.00258	294.0	8.62196E-06	1.55521E-04	1.11970E-05

sum			5.54394E-02	1.00000E+00	1.00000E+00

DCLL BZ material					
Atom density 4.47186E-02 1/barn*cm					
Mass density 8.68650E+00 g/cm3					
Nuclide	a. weight	temp	a. dens	a. frac	m. frac
82208.03c	207.97663	294.0	1.03285E-02	2.30966E-01	4.10641E-01
82207.03c	206.97603	294.0	4.28685E-03	9.58628E-02	1.69617E-01
82206.03c	205.97443	294.0	4.87155E-03	1.08938E-01	1.91819E-01
3006.03c	6.01507	294.0	3.70859E-03	8.29317E-02	4.26443E-03
3007.03c	7.01600	294.0	4.12053E-04	9.21437E-03	5.52655E-04
2003.03c	3.01603	294.0	1.21733E-12	2.72221E-11	7.01870E-13
2004.03c	4.00258	294.0	1.18471E-06	2.64926E-05	9.06491E-07
6000.03c	12.00110	294.0	1.06278E-04	2.37661E-03	2.43824E-04
23051.03c	50.94397	294.0	4.55237E-05	1.01800E-03	4.43344E-04
24052.03c	51.94051	294.0	1.75458E-03	3.92362E-02	1.74217E-02
24053.03c	52.94066	294.0	1.99023E-04	4.45056E-03	2.01420E-03
24054.03c	53.93889	294.0	4.95332E-05	1.10766E-03	5.10751E-04
25055.03c	54.93805	294.0	8.44280E-05	1.88799E-03	8.86689E-04
26054.03c	53.93962	294.0	1.07561E-03	2.40529E-02	1.10911E-02
26056.03c	55.93491	294.0	1.70037E-02	3.80238E-01	1.81818E-01
26057.03c	56.93541	294.0	4.07882E-04	9.12110E-03	4.43944E-03
26058.03c	57.93329	294.0	5.19154E-05	1.16094E-03	5.74958E-04
74182.03c	181.94813	294.0	1.84077E-05	4.11635E-04	6.40264E-04
74183.03c	182.95024	294.0	9.93411E-06	2.22147E-04	3.47435E-04
74184.03c	183.95094	294.0	2.12845E-05	4.75966E-04	7.48475E-04
74186.03c	185.95435	294.0	1.97498E-05	4.41647E-04	7.02070E-04
73181.03c	180.94794	294.0	5.12672E-06	1.14644E-04	1.77339E-04
22048.03c	47.94795	294.0	1.78721E-06	3.99658E-05	1.63816E-05
22047.03c	46.95176	294.0	1.76831E-07	3.95430E-06	1.58716E-06
22046.03c	45.95264	294.0	1.93768E-07	4.33305E-06	1.70217E-06
22049.03c	48.94787	294.0	1.33173E-07	2.97803E-06	1.24612E-06

22050.03c	49.94479	294.0	1.30724E-07	2.92327E-06	1.24813E-06
8016.03c	15.99492	294.0	1.20515E-04	2.69496E-03	3.68496E-04
14028.03c	27.97734	294.0	1.90359E-05	4.25682E-04	1.01810E-04
14029.03c	28.97693	294.0	9.64098E-07	2.15592E-05	5.34054E-06
14030.03c	29.97349	294.0	6.39864E-07	1.43087E-05	3.66637E-06
7014.03c	14.00307	294.0	2.48408E-05	5.55491E-04	6.64967E-05
13027.03c	26.98154	294.0	8.01289E-05	1.79185E-03	4.13301E-04
16032.18c	31.97208	1800	1.81301E-06	4.05428E-05	1.10811E-05
15031.03c	30.97376	294.0	1.87145E-06	4.18495E-05	1.10811E-05
27059.03c	58.93317	294.0	9.83586E-07	2.19950E-05	1.10811E-05
28058.03c	57.93570	294.0	6.72461E-07	1.50376E-05	7.44775E-06
28060.03c	59.93079	294.0	2.59087E-07	5.79373E-06	2.96830E-06
28062.03c	61.92835	294.0	3.58524E-08	8.01734E-07	4.24443E-07
28061.03c	60.93143	294.0	1.12648E-08	2.51905E-07	1.31213E-07
28064.03c	63.92818	294.0	9.14917E-09	2.04594E-07	1.11811E-07
29063.03c	62.92961	294.0	6.31068E-07	1.41120E-05	7.59176E-06
29065.03c	64.92780	294.0	2.81288E-07	6.29019E-06	3.49135E-06
41093.03c	92.90639	294.0	1.24783E-07	2.79041E-06	2.21622E-06
42092.03c	91.90682	294.0	1.92057E-08	4.29479E-07	3.37434E-07
42094.03c	93.90510	294.0	1.15879E-08	2.59131E-07	2.08021E-07
42095.03c	94.90589	294.0	1.96351E-08	4.39082E-07	3.56236E-07
42096.03c	95.90468	294.0	2.02379E-08	4.52562E-07	3.71037E-07
42097.03c	96.90602	294.0	1.14126E-08	2.55211E-07	2.11421E-07
42098.03c	97.90541	294.0	2.84114E-08	6.35337E-07	5.31753E-07
42100.03c	99.90748	294.0	1.09860E-08	2.45670E-07	2.09821E-07
5010.03c	10.01294	294.0	2.13434E-07	4.77282E-06	4.08541E-07
5011.03c	11.00928	294.0	8.59156E-07	1.92125E-05	1.80818E-06
8017.03c	16.99913	294.0	4.41937E-07	9.88262E-06	1.43614E-06
sum			4.47186E-02	1.00000E+00	1.00000E+00

HCPB BZ material
Atom density 6.87261E-02 1/barn*cm

Mass density 1.80000E+00 g/cm3					
Nuclide	a. weight	temp	a. dens	a. frac	m. frac
4009.03c	9.01220	294.0	4.51168E-02	6.56473E-01	3.75105E-01
2004.03c	4.00258	294.0	9.48125E-06	1.37957E-04	3.50098E-05
6000.03c	12.00110	294.0	4.26441E-05	6.20494E-04	4.72132E-04
23051.03c	50.94397	294.0	1.82656E-05	2.65774E-04	8.58441E-04
24052.03c	51.94051	294.0	7.04123E-04	1.02453E-02	3.37395E-02
24053.03c	52.94066	294.0	7.98345E-05	1.16163E-03	3.89909E-03
24054.03c	53.93889	294.0	1.98747E-05	2.89187E-04	9.88977E-04
25055.03c	54.93805	294.0	3.38674E-05	4.92788E-04	1.71648E-03
26054.03c	53.93962	294.0	4.31380E-04	6.27680E-03	2.14660E-02
26056.03c	55.93491	294.0	6.82335E-03	9.92833E-02	3.52099E-01
26057.03c	56.93541	294.0	1.63663E-04	2.38138E-03	8.59641E-03
26058.03c	57.93329	294.0	2.08308E-05	3.03098E-04	1.11331E-03
74182.03c	181.94813	294.0	7.38349E-06	1.07434E-04	1.23935E-03
74183.03c	182.95024	294.0	3.98563E-06	5.79930E-05	6.72689E-04
74184.03c	183.95094	294.0	8.54092E-06	1.24275E-04	1.44941E-03
74186.03c	185.95435	294.0	7.92412E-06	1.15300E-04	1.35938E-03
73181.03c	180.94794	294.0	2.05676E-06	2.99269E-05	3.43338E-04
22048.03c	47.94795	294.0	7.17075E-07	1.04338E-05	3.17189E-05
22047.03c	46.95176	294.0	7.09427E-08	1.03225E-06	3.07286E-06
22046.03c	45.95264	294.0	7.77469E-08	1.13126E-06	3.29592E-06
22049.03c	48.94787	294.0	5.34517E-08	7.77750E-07	2.41368E-06
22050.03c	49.94479	294.0	5.24716E-08	7.63489E-07	2.41768E-06
8016.03c	15.99492	294.0	7.08681E-03	1.03117E-01	1.04572E-01
14028.03c	27.97734	294.0	7.63868E-06	1.11147E-04	1.97155E-04
14029.03c	28.97693	294.0	3.86907E-07	5.62969E-06	1.03429E-05
14030.03c	29.97349	294.0	2.56766E-07	3.73607E-06	7.09999E-06
7014.03c	14.00307	294.0	9.96537E-06	1.45001E-04	1.28736E-04
13027.03c	26.98154	294.0	1.72437E-06	2.50904E-05	4.29220E-05
16032.18c	31.97208	1800.0	7.27436E-07	1.05846E-05	2.14560E-05
15031.03c	30.97376	294.0	7.50882E-07	1.09257E-05	2.14560E-05

27059.03c	58.93317	294.0	3.94644E-07	5.74227E-06	2.14560E-05
28058.03c	57.93570	294.0	2.69872E-07	3.92677E-06	1.44240E-05
28060.03c	59.93079	294.0	1.03957E-07	1.51263E-06	5.74761E-06
28062.03c	61.92835	294.0	1.43867E-08	2.09334E-07	8.21930E-07
28061.03c	60.93143	294.0	4.51814E-09	6.57412E-08	2.53971E-07
28064.03c	63.92818	294.0	3.67031E-09	5.34049E-08	2.16461E-07
29063.03c	62.92961	294.0	2.53280E-07	3.68535E-06	1.47041E-05
29065.03c	64.92780	294.0	1.12856E-07	1.64212E-06	6.75989E-06
41093.03c	92.90639	294.0	5.00785E-08	7.28667E-07	4.29220E-06
42092.03c	91.90682	294.0	7.70613E-09	1.12128E-07	6.53383E-07
42094.03c	93.90510	294.0	4.64861E-09	6.76396E-08	4.02713E-07
42095.03c	94.90589	294.0	7.87848E-09	1.14636E-07	6.89793E-07
42096.03c	95.90468	294.0	8.11977E-09	1.18147E-07	7.18401E-07
42097.03c	96.90602	294.0	4.57962E-09	6.66358E-08	4.09415E-07
42098.03c	97.90541	294.0	1.13959E-08	1.65815E-07	1.02929E-06
42100.03c	99.90748	294.0	4.40839E-09	6.41443E-08	4.06314E-07
5010.03c	10.01294	294.0	8.56334E-08	1.24601E-06	7.91022E-07
5011.03c	11.00928	294.0	3.44705E-07	5.01563E-06	3.50098E-06
3006.03c	6.01507	294.0	4.03780E-03	5.87521E-02	2.24063E-02
3007.03c	7.01600	294.0	2.30732E-03	3.35727E-02	1.49342E-02
16032.03c	31.97208	294.0	1.77603E-03	2.58421E-02	5.23847E-02
sum			6.87261E-02	1.00000E+00	1.00000E+00

DCLL BSS material					
Atom density 6.96809E-02 1/barn*cm					
Mass density 8.13150E+00 g/cm3					
Nuclide	a. weight	temp	a. dens	a. frac	m. frac
82208.03c	207.97663	294.0	3.83819E-03	5.50823E-02	1.63014E-01
82207.03c	206.97603	294.0	1.59321E-03	2.28644E-02	6.73408E-02
82206.03c	205.97443	294.0	1.81047E-03	2.59823E-02	7.61534E-02
3006.03c	6.01507	294.0	1.37815E-03	1.97781E-02	1.69287E-03
3007.03c	7.01600	294.0	1.53127E-04	2.19755E-03	2.19395E-04

2003.03c	3.01603	294.0	4.94204E-13	7.09239E-12	3.04388E-13
2004.03c	4.00258	294.0	4.80980E-07	6.90261E-06	3.93145E-07
6000.03c	12.00110	294.0	3.09392E-04	4.44012E-03	7.58254E-04
23051.03c	50.94397	294.0	1.32518E-04	1.90178E-03	1.37864E-03
24052.03c	51.94051	294.0	5.10870E-03	7.33157E-02	5.41879E-02
24053.03c	52.94066	294.0	5.79286E-04	8.31341E-03	6.26279E-03
24054.03c	53.93889	294.0	1.44197E-04	2.06939E-03	1.58834E-03
25055.03c	54.93805	294.0	2.45767E-04	3.52703E-03	2.75729E-03
26054.03c	53.93962	294.0	3.13053E-03	4.49267E-02	3.44835E-02
26056.03c	55.93491	294.0	4.95056E-02	7.10462E-01	5.65487E-01
26057.03c	56.93541	294.0	1.18744E-03	1.70411E-02	1.38064E-02
26058.03c	57.93329	294.0	1.51129E-04	2.16888E-03	1.78798E-03
74182.03c	181.94813	294.0	5.35902E-05	7.69081E-04	1.99122E-03
74183.03c	182.95024	294.0	2.89186E-05	4.15015E-04	1.08043E-03
74184.03c	183.95094	294.0	6.19623E-05	8.89230E-04	2.32764E-03
74186.03c	185.95435	294.0	5.74932E-05	8.25093E-04	2.18327E-03
73181.03c	180.94794	294.0	1.49236E-05	2.14170E-04	5.51458E-04
22048.03c	47.94795	294.0	5.20300E-06	7.46690E-05	5.09459E-05
22047.03c	46.95176	294.0	5.14660E-07	7.38595E-06	4.93466E-06
22046.03c	45.95264	294.0	5.64011E-07	8.09420E-06	5.29277E-06
22049.03c	48.94787	294.0	3.87757E-07	5.56475E-06	3.87596E-06
22050.03c	49.94479	294.0	3.80707E-07	5.46358E-06	3.88299E-06
8016.03c	15.99492	294.0	2.11035E-05	3.02860E-04	6.89322E-05
14028.03c	27.97734	294.0	5.54230E-05	7.95384E-04	3.16652E-04
14029.03c	28.97693	294.0	2.80630E-06	4.02736E-05	1.66063E-05
14030.03c	29.97349	294.0	1.86290E-06	2.67347E-05	1.14028E-05
7014.03c	14.00307	294.0	7.23160E-05	1.03782E-03	2.06796E-04
13027.03c	26.98154	294.0	1.25104E-05	1.79538E-04	6.89322E-05
16032.18c	31.97208	1800.0	5.27882E-06	7.57571E-05	3.44662E-05
15031.03c	30.97376	294.0	5.44896E-06	7.81988E-05	3.44662E-05
27059.03c	58.93317	294.0	2.86383E-06	4.10993E-05	3.44662E-05
28058.03c	57.93570	294.0	1.95751E-06	2.80925E-05	2.31598E-05

28060.03c	59.93079	294.0	7.54230E-07	1.08241E-05	9.23080E-06
28062.03c	61.92835	294.0	1.04378E-07	1.49795E-06	1.32004E-06
28061.03c	60.93143	294.0	3.27799E-08	4.70429E-07	4.07882E-07
28064.03c	63.92818	294.0	2.66265E-08	3.82121E-07	3.47610E-07
29063.03c	62.92961	294.0	1.83713E-06	2.63649E-05	2.36091E-05
29065.03c	64.92780	294.0	8.18834E-07	1.17512E-05	1.08571E-05
41093.03c	92.90639	294.0	3.63322E-07	5.21408E-06	6.89322E-06
42094.03c	93.90510	294.0	1.07643E-08	1.54479E-07	2.06423E-07
42095.03c	94.90589	294.0	1.82436E-08	2.61816E-07	3.53581E-07
42096.03c	95.90468	294.0	1.88014E-08	2.69822E-07	3.68227E-07
42097.03c	96.90602	294.0	1.06054E-08	1.52199E-07	2.09875E-07
42098.03c	97.90541	294.0	2.63967E-08	3.78823E-07	5.27767E-07
42100.03c	99.90748	294.0	1.02065E-08	1.46476E-07	2.08239E-07
5010.03c	10.01294	294.0	6.21332E-07	8.91682E-06	1.27049E-06
5011.03c	11.00928	294.0	2.50094E-06	3.58914E-05	5.62274E-06
sum			6.96809E-02	1.00000E+00	1.00000E+00

HCPB BSS material					
Atom density 5.17796E-02 1/barn*cm					
Mass density 4.78000E+00 g/cm3					
Nuclide	a. weight	temp	a. dens	a. frac	m. frac
6000.03c	12.00110	294.0	2.62978E-04	5.07880E-03	1.09640E-03
23051.03c	50.94397	294.0	1.12635E-04	2.17528E-03	1.99340E-03
24052.03c	51.94051	294.0	4.34226E-03	8.38604E-02	7.83520E-02
24053.03c	52.94066	294.0	4.92379E-04	9.50913E-03	9.05560E-03
24054.03c	53.93889	294.0	1.22562E-04	2.36699E-03	2.29660E-03
25055.03c	54.93805	294.0	2.08898E-04	4.03436E-03	3.98690E-03
26054.03c	53.93962	294.0	2.66088E-03	5.13885E-02	4.98610E-02
26056.03c	55.93491	294.0	4.20786E-02	8.12649E-01	8.17660E-01
26057.03c	56.93541	294.0	1.00929E-03	1.94920E-02	1.99630E-02
26058.03c	57.93329	294.0	1.28456E-04	2.48082E-03	2.58530E-03
74182.03c	181.94813	294.0	4.55508E-05	8.79705E-04	2.87920E-03

74183.03c	182.95024	294.0	2.45796E-05	4.74697E-04	1.56220E-03
74184.03c	183.95094	294.0	5.26662E-05	1.01712E-03	3.36560E-03
74186.03c	185.95435	294.0	4.88682E-05	9.43773E-04	3.15690E-03
73181.03c	180.94794	294.0	1.26847E-05	2.44975E-04	7.97376E-04
22048.03c	47.94795	294.0	4.42239E-06	8.54079E-05	7.36640E-05
22047.03c	46.95176	294.0	4.37447E-07	8.44826E-06	7.13520E-06
22046.03c	45.95264	294.0	4.79394E-07	9.25836E-06	7.65300E-06
22049.03c	48.94787	294.0	3.29585E-07	6.36515E-06	5.60440E-06
22050.03c	49.94479	294.0	3.23594E-07	6.24945E-06	5.61460E-06
8016.03c	15.99492	294.0	1.79375E-05	3.46421E-04	9.96720E-05
14028.03c	27.97734	294.0	4.71083E-05	9.09786E-04	4.57860E-04
14029.03c	28.97693	294.0	2.38533E-06	4.60669E-05	2.40120E-05
14030.03c	29.97349	294.0	1.58344E-06	3.05804E-05	1.64880E-05
7014.03c	14.00307	294.0	6.14659E-05	1.18707E-03	2.99010E-04
13027.03c	26.98154	294.0	1.06335E-05	2.05362E-04	9.96720E-05
16032.18c	31.97208	1800.0	4.48687E-06	8.66533E-05	4.98360E-05
15031.03c	30.97376	294.0	4.63149E-06	8.94463E-05	4.98360E-05
27059.03c	58.93317	294.0	2.43419E-06	4.70107E-05	4.98360E-05
28058.03c	57.93570	294.0	1.66385E-06	3.21333E-05	3.34880E-05
28060.03c	59.93079	294.0	6.41070E-07	1.23807E-05	1.33470E-05
28062.03c	61.92835	294.0	8.87196E-08	1.71341E-06	1.90870E-06
28061.03c	60.93143	294.0	2.78620E-08	5.38089E-07	5.89770E-07
28064.03c	63.92818	294.0	2.26318E-08	4.37079E-07	5.02620E-07
29063.03c	62.92961	294.0	1.56150E-06	3.01567E-05	3.41370E-05
29065.03c	64.92780	294.0	6.96006E-07	1.34417E-05	1.56990E-05
41093.03c	92.90639	294.0	3.08816E-07	5.96404E-06	9.96720E-06
42092.03c	91.90682	294.0	4.75252E-08	9.17836E-07	1.51740E-06
42094.03c	93.90510	294.0	2.86679E-08	5.53653E-07	9.35220E-07
42095.03c	94.90589	294.0	4.85893E-08	9.38388E-07	1.60200E-06
42096.03c	95.90468	294.0	5.00733E-08	9.67046E-07	1.66830E-06
42097.03c	96.90602	294.0	2.82450E-08	5.45486E-07	9.50870E-07
42098.03c	97.90541	294.0	7.03012E-08	1.35770E-06	2.39110E-06

42100.03c	99.90748	294.0	2.71836E-08	5.24986E-07	9.43480E-07
5010.03c	10.01294	294.0	5.28104E-07	1.01991E-05	1.83700E-06
5011.03c	11.00928	294.0	2.12573E-06	4.10535E-05	8.13010E-06
2004.03c	4.00258	294.0	9.68002E-06	1.86947E-04	1.34600E-05
sum			5.17796E-02	1.00000E+00	1.00000E+00

Inner and outer vacuum vessel material					
Atom density 8.58301E-02 1/barn*cm					
Mass density 7.92089E+00 g/cm3					
Nuclide	a. weight	temp	a. dens	a. frac	m. frac
26054.03c	53.93962	294.0	3.29181E-03	3.83527E-02	3.72242E-02
26056.03c	55.93491	294.0	4.98289E-02	5.80553E-01	5.84315E-01
26057.03c	56.93541	294.0	1.13058E-03	1.31723E-02	1.34948E-02
26058.03c	57.93329	294.0	1.47865E-04	1.72277E-03	1.79587E-03
6000.03c	12.00110	294.0	1.19277E-04	1.38969E-03	3.00096E-04
25055.03c	54.93805	294.0	1.73653E-03	2.02322E-02	2.00004E-02
14028.03c	27.97734	294.0	7.86497E-04	9.16341E-03	4.61302E-03
14029.03c	28.97693	294.0	3.85593E-05	4.49252E-04	2.34242E-04
14030.03c	29.97349	294.0	2.45713E-05	2.86279E-04	1.54400E-04
15031.03c	30.97376	294.0	3.85117E-05	4.48697E-04	2.50074E-04
16032.03c	31.97208	294.0	1.41667E-05	1.65055E-04	9.49559E-05
16033.03c	32.97146	294.0	1.09980E-07	1.28137E-06	7.60211E-07
16034.03c	33.96787	294.0	6.02550E-07	7.02026E-06	4.29085E-06
16036.03c	35.96709	294.0	2.65303E-09	3.09103E-08	2.00046E-08
24050.03c	49.94605	294.0	7.46976E-04	8.70296E-03	7.82149E-03
24052.03c	51.94051	294.0	1.38506E-02	1.61372E-01	1.50819E-01
24053.03c	52.94066	294.0	1.54092E-03	1.79532E-02	1.71022E-02
24054.03c	53.93889	294.0	3.76464E-04	4.38616E-03	4.25704E-03
28058.03c	57.93570	294.0	7.00642E-03	8.16312E-02	8.50990E-02
28060.03c	59.93079	294.0	2.60890E-03	3.03961E-02	3.27786E-02
28061.03c	60.93143	294.0	1.11548E-04	1.29964E-03	1.42490E-03
28062.03c	61.92835	294.0	3.49927E-04	4.07698E-03	4.54307E-03

28064.03c	63.92818	294.0	8.63312E-05	1.00584E-03	1.15702E-03
42092.03c	91.90682	294.0	2.07981E-04	2.42317E-03	4.00732E-03
42094.03c	93.90510	294.0	1.26880E-04	1.47827E-03	2.49784E-03
42095.03c	94.90589	294.0	2.16071E-04	2.51743E-03	4.29905E-03
42096.03c	95.90468	294.0	2.24028E-04	2.61014E-03	4.50427E-03
42097.03c	96.90602	294.0	1.26943E-04	1.47900E-03	2.57894E-03
42098.03c	97.90541	294.0	3.17475E-04	3.69888E-03	6.51626E-03
42100.03c	99.90748	294.0	1.24166E-04	1.44665E-03	2.60066E-03
7014.03c	14.00307	294.0	2.71878E-04	3.16763E-03	7.98142E-04
7015.03c	14.99986	294.0	9.37262E-07	1.09200E-05	2.94734E-06
5010.03c	10.01294	294.0	9.50315E-07	1.10720E-05	1.99485E-06
5011.03c	11.00928	294.0	3.47739E-06	4.05148E-05	8.02592E-06
29063.03c	62.92961	294.0	1.57294E-04	1.83262E-03	2.07515E-03
29065.03c	64.92780	294.0	6.79510E-05	7.91692E-04	9.24929E-04
27059.03c	58.93317	294.0	4.04699E-05	4.71512E-04	5.00005E-04
41093.03c	92.90639	294.0	5.13489E-06	5.98263E-05	1.00014E-04
22046.03c	45.95264	294.0	8.56467E-06	9.97863E-05	8.25093E-05
22047.03c	46.95176	294.0	7.55944E-06	8.80744E-05	7.44086E-05
22048.03c	47.94795	294.0	7.33430E-05	8.54513E-04	7.37243E-04
22049.03c	48.94787	294.0	5.27248E-06	6.14293E-05	5.41042E-05
22050.03c	49.94479	294.0	4.94736E-06	5.76414E-05	5.18020E-05
73181.03c	180.94794	294.0	2.63837E-06	3.07395E-05	1.00086E-04
sum			8.58301E-02	1.00000E+00	1.00000E+00

Shield vacuum vessel material composition					
Atom density 9.16106E-02 1/barn*cm					
Mass density 5.15190E+00 g/cm3					
Nuclide	a. weight	temp	a. dens	a. frac	m. frac
26054.03c	53.93962	294.0	1.97509E-03	2.15596E-02	3.43387E-02
26056.03c	55.93491	294.0	2.98973E-02	3.26352E-01	5.39019E-01
26057.03c	56.93541	294.0	6.78346E-04	7.40466E-03	1.24487E-02
26058.03c	57.93329	294.0	8.87190E-05	9.68435E-04	1.65666E-03

6000.03c	12.00110	294.0	7.15661E-05	7.81198E-04	2.76833E-04
25055.03c	54.93805	294.0	1.04192E-03	1.13734E-02	1.84500E-02
14028.03c	27.97734	294.0	4.71898E-04	5.15113E-03	4.25543E-03
14029.03c	28.97693	294.0	2.31355E-05	2.52542E-04	2.16083E-04
14030.03c	29.97349	294.0	1.47428E-05	1.60929E-04	1.42432E-04
15031.03c	30.97376	294.0	2.31070E-05	2.52231E-04	2.30689E-04
16032.03c	31.97208	294.0	8.49999E-06	9.27839E-05	8.75948E-05
16033.03c	32.97146	294.0	6.59880E-08	7.20309E-07	7.01281E-07
16034.03c	33.96787	294.0	3.61529E-07	3.94636E-06	3.95822E-06
16036.03c	35.96709	294.0	1.59182E-09	1.73759E-08	1.84539E-08
24050.03c	49.94605	294.0	4.48185E-04	4.89228E-03	7.21518E-03
24052.03c	51.94051	294.0	8.31039E-03	9.07142E-02	1.39129E-01
24053.03c	52.94066	294.0	9.24551E-04	1.00922E-02	1.57764E-02
24054.03c	53.93889	294.0	2.25879E-04	2.46564E-03	3.92705E-03
28058.03c	57.93570	294.0	4.20385E-03	4.58882E-02	7.85023E-02
28060.03c	59.93079	294.0	1.56534E-03	1.70869E-02	3.02376E-02
28061.03c	60.93143	294.0	6.69286E-05	7.30577E-04	1.31444E-03
28062.03c	61.92835	294.0	2.09956E-04	2.29183E-03	4.19089E-03
28064.03c	63.92818	294.0	5.17987E-05	5.65422E-04	1.06733E-03
42092.03c	91.90682	294.0	1.24789E-04	1.36217E-03	3.69669E-03
42094.03c	93.90510	294.0	7.61277E-05	8.30992E-04	2.30420E-03
42095.03c	94.90589	294.0	1.29643E-04	1.41515E-03	3.96580E-03
42096.03c	95.90468	294.0	1.34417E-04	1.46726E-03	4.15511E-03
42097.03c	96.90602	294.0	7.61659E-05	8.31409E-04	2.37903E-03
42098.03c	97.90541	294.0	1.90485E-04	2.07929E-03	6.01113E-03
42100.03c	99.90748	294.0	7.44998E-05	8.13222E-04	2.39906E-03
7014.03c	14.00307	294.0	1.63127E-04	1.78066E-03	7.36272E-04
7015.03c	14.99986	294.0	5.62356E-07	6.13854E-06	2.71886E-06
5010.03c	10.01294	294.0	5.70188E-07	6.22404E-06	1.84021E-06
5011.03c	11.00928	294.0	2.08644E-06	2.27751E-05	7.40378E-06
29063.03c	62.92961	294.0	9.43765E-05	1.03019E-03	1.91429E-03
29065.03c	64.92780	294.0	4.07706E-05	4.45042E-04	8.53231E-04

27059.03c	58.93317	294.0	2.42819E-05	2.65055E-04	4.61245E-04
41093.03c	92.90639	294.0	3.08093E-06	3.36307E-05	9.22606E-05
22046.03c	45.95264	294.0	5.13879E-06	5.60938E-05	7.61132E-05
22047.03c	46.95176	294.0	4.53566E-06	4.95102E-05	6.86406E-05
22048.03c	47.94795	294.0	4.40057E-05	4.80356E-04	6.80092E-04
22049.03c	48.94787	294.0	3.16349E-06	3.45319E-05	4.99102E-05
22050.03c	49.94479	294.0	2.96842E-06	3.24026E-05	4.77864E-05
73181.03c	180.94794	294.0	1.58302E-06	1.72799E-05	9.23270E-05
1001.03c	1.00782	294.0	2.67614E-02	2.92121E-01	8.69326E-03
1002.03c	2.01410	294.0	1.53896E-06	1.67989E-05	9.99074E-07
8016.03c	15.99492	294.0	1.33497E-02	1.45722E-01	6.88244E-02
sum			9.16106E-02	1.00000E+00	1.00000E+00

Coils Jacket case material					
Atom density 8.58301E-02 1/barn*cm					
Mass density 7.92089E+00 g/cm3					
Nuclide	a. weight	temp	a. dens	a. frac	m. frac
26054.03c	53.93962	294.0	3.29181E-03	3.83527E-02	3.72242E-02
26056.03c	55.93491	294.0	4.98289E-02	5.80553E-01	5.84315E-01
26057.03c	56.93541	294.0	1.13058E-03	1.31723E-02	1.34948E-02
26058.03c	57.93329	294.0	1.47865E-04	1.72277E-03	1.79587E-03
6000.03c	12.00110	294.0	1.19277E-04	1.38969E-03	3.00096E-04
25055.03c	54.93805	294.0	1.73653E-03	2.02322E-02	2.00004E-02
14028.03c	27.97734	294.0	7.86497E-04	9.16341E-03	4.61302E-03
14029.03c	28.97693	294.0	3.85593E-05	4.49252E-04	2.34242E-04
14030.03c	29.97349	294.0	2.45713E-05	2.86279E-04	1.54400E-04
15031.03c	30.97376	294.0	3.85117E-05	4.48697E-04	2.50074E-04
16032.03c	31.97208	294.0	1.41667E-05	1.65055E-04	9.49559E-05
16033.03c	32.97146	294.0	1.09980E-07	1.28137E-06	7.60211E-07
16034.03c	33.96787	294.0	6.02550E-07	7.02026E-06	4.29085E-06
16036.03c	35.96709	294.0	2.65303E-09	3.09103E-08	2.00046E-08
24050.03c	49.94605	294.0	7.46976E-04	8.70296E-03	7.82149E-03

24052.03c	51.94051	294.0	1.38506E-02	1.61372E-01	1.50819E-01
24053.03c	52.94066	294.0	1.54092E-03	1.79532E-02	1.71022E-02
24054.03c	53.93889	294.0	3.76464E-04	4.38616E-03	4.25704E-03
28058.03c	57.93570	294.0	7.00642E-03	8.16312E-02	8.50990E-02
28060.03c	59.93079	294.0	2.60890E-03	3.03961E-02	3.27786E-02
28061.03c	60.93143	294.0	1.11548E-04	1.29964E-03	1.42490E-03
28062.03c	61.92835	294.0	3.49927E-04	4.07698E-03	4.54307E-03
28064.03c	63.92818	294.0	8.63312E-05	1.00584E-03	1.15702E-03
42092.03c	91.90682	294.0	2.07981E-04	2.42317E-03	4.00732E-03
42094.03c	93.90510	294.0	1.26880E-04	1.47827E-03	2.49784E-03
42095.03c	94.90589	294.0	2.16071E-04	2.51743E-03	4.29905E-03
42096.03c	95.90468	294.0	2.24028E-04	2.61014E-03	4.50427E-03
42097.03c	96.90602	294.0	1.26943E-04	1.47900E-03	2.57894E-03
42098.03c	97.90541	294.0	3.17475E-04	3.69888E-03	6.51626E-03
42100.03c	99.90748	294.0	1.24166E-04	1.44665E-03	2.60066E-03
7014.03c	14.00307	294.0	2.71878E-04	3.16763E-03	7.98142E-04
7015.03c	14.99986	294.0	9.37262E-07	1.09200E-05	2.94734E-06
5010.03c	10.01294	294.0	9.50315E-07	1.10720E-05	1.99485E-06
5011.03c	11.00928	294.0	3.47739E-06	4.05148E-05	8.02592E-06
29063.03c	62.92961	294.0	1.57294E-04	1.83262E-03	2.07515E-03
29065.03c	64.92780	294.0	6.79510E-05	7.91692E-04	9.24929E-04
27059.03c	58.93317	294.0	4.04699E-05	4.71512E-04	5.00005E-04
41093.03c	92.90639	294.0	5.13489E-06	5.98263E-05	1.00014E-04
22046.03c	45.95264	294.0	8.56467E-06	9.97863E-05	8.25093E-05
22047.03c	46.95176	294.0	7.55944E-06	8.80744E-05	7.44086E-05
22048.03c	47.94795	294.0	7.33430E-05	8.54513E-04	7.37243E-04
22049.03c	48.94787	294.0	5.27248E-06	6.14293E-05	5.41042E-05
22050.03c	49.94479	294.0	4.94736E-06	5.76414E-05	5.18020E-05
73181.03c	180.94794	294.0	2.63837E-06	3.07395E-05	1.00086E-04
sum			8.58301E-02	1.00000E+00	1.00000E+00

Coils winding pack material

Atom density 7.19439E-02 1/barn*cm					
Mass density 5.50820E+00 g/cm3					
Nuclide	a. weight	temp	a. dens	a. frac	m. frac
1001.03c	1.00782	294.0	3.67608E-03	5.10965E-02	1.11691E-03
6000.03c	12.00110	294.0	3.37621E-03	4.69284E-02	1.22151E-02
7014.03c	14.00307	294.0	6.12002E-04	8.50666E-03	2.58358E-03
8016.03c	15.99492	294.0	4.60134E-03	6.39573E-02	2.21877E-02
12024.03c	23.98504	294.0	1.59753E-04	2.22052E-03	1.15514E-03
12025.03c	24.98584	294.0	2.02244E-05	2.81113E-04	1.52341E-04
12026.03c	25.98260	294.0	2.22670E-05	3.09506E-04	1.74418E-04
13027.03c	26.98154	294.0	8.82529E-04	1.22669E-02	7.17864E-03
14028.03c	27.97734	294.0	1.32260E-03	1.83838E-02	1.11553E-02
14029.03c	28.97693	294.0	6.34491E-05	8.81924E-04	5.54273E-04
14030.03c	29.97349	294.0	4.21105E-03	5.85325E-02	3.80517E-02
16032.03c	31.97208	294.0	8.30815E-05	1.15481E-03	8.00795E-04
16033.03c	32.97146	294.0	6.65142E-07	9.24529E-06	6.61148E-06
16034.03c	33.96787	294.0	3.75455E-06	5.21872E-05	3.84479E-05
16036.03c	35.96709	294.0	1.75037E-08	2.43297E-07	1.89794E-07
29063.03c	62.92961	294.0	9.67543E-03	1.34486E-01	1.83557E-01
29065.03c	64.92780	294.0	4.32635E-03	6.01350E-02	8.46834E-02
41093.03c	92.90639	294.0	1.12971E-03	1.57026E-02	3.16415E-02
50112.03c	111.90533	294.0	6.02344E-06	8.37241E-05	2.03208E-04
50114.03c	113.90248	294.0	4.09843E-06	5.69670E-05	1.40733E-04
50115.03c	114.90308	294.0	2.11131E-06	2.93466E-05	7.31357E-05
50116.03c	115.90166	294.0	9.02895E-05	1.25500E-03	3.15481E-03
50117.03c	116.90326	294.0	4.76907E-05	6.62887E-04	1.68076E-03
50118.03c	117.90184	294.0	1.50400E-04	2.09051E-03	5.34581E-03
50119.03c	118.90344	294.0	5.33417E-05	7.41434E-04	1.91209E-03
50120.03c	119.90202	294.0	2.02313E-04	2.81210E-03	7.31302E-03
50122.03c	121.90341	294.0	2.87511E-05	3.99632E-04	1.05661E-03
50124.03c	123.90531	294.0	3.59543E-05	4.99755E-04	1.34303E-03
2004.03c	4.00258	294.0	2.91647E-03	4.05381E-02	3.51920E-03

5010.03c	10.01294	294.0	3.83616E-07	5.33215E-06	1.15799E-06
5011.03c	11.00928	294.0	1.40436E-06	1.95202E-05	4.66104E-06
15031.03c	30.97376	294.0	1.55794E-05	2.16549E-04	1.45476E-04
19039.03c	38.96371	294.0	2.30198E-07	3.19969E-06	2.70401E-06
19040.03c	39.96400	294.0	2.88804E-11	4.01429E-10	3.47951E-10
19041.03c	40.96183	294.0	1.66129E-08	2.30915E-07	2.05150E-07
22046.03c	45.95264	294.0	1.33039E-06	1.84921E-05	1.84304E-05
22047.03c	46.95176	294.0	1.19977E-06	1.66765E-05	1.69823E-05
22048.03c	47.94795	294.0	1.18881E-05	1.65241E-04	1.71841E-04
22049.03c	48.94787	294.0	8.72415E-07	1.21263E-05	1.28737E-05
22050.03c	49.94479	294.0	8.35326E-07	1.16108E-05	1.25774E-05
23051.03c	50.94397	294.0	1.51563E-06	2.10668E-05	2.32773E-05
24050.03c	49.94605	294.0	2.86490E-04	3.98214E-03	4.31378E-03
24052.03c	51.94051	294.0	5.35394E-03	7.44183E-02	8.38351E-02
24053.03c	52.94066	294.0	5.98889E-04	8.32439E-03	9.55833E-03
24054.03c	53.93889	294.0	1.46490E-04	2.03617E-03	2.38208E-03
25055.03c	54.93805	294.0	5.27013E-04	7.32534E-03	8.72853E-03
26054.03c	53.93962	294.0	1.38397E-03	1.92368E-02	2.25051E-02
26056.03c	55.93491	294.0	2.09513E-02	2.91217E-01	3.53297E-01
26057.03c	56.93541	294.0	4.87202E-04	6.77197E-03	8.36253E-03
26058.03c	57.93329	294.0	6.83980E-05	9.50713E-04	1.19459E-03
27059.03c	58.93317	294.0	1.63763E-05	2.27626E-04	2.90952E-04
28058.03c	57.93570	294.0	2.73203E-03	3.79744E-02	4.77175E-02
28060.03c	59.93079	294.0	1.01949E-03	1.41706E-02	1.84196E-02
28061.03c	60.93143	294.0	4.79138E-05	6.65988E-04	8.80132E-04
28062.03c	61.92835	294.0	1.38033E-04	1.91862E-03	2.57702E-03
28064.03c	63.92818	294.0	4.23797E-05	5.89066E-04	8.16764E-04
40090.03c	89.90472	294.0	2.17644E-07	3.02518E-06	5.89895E-06
40091.03c	90.90567	294.0	4.74627E-08	6.59719E-07	1.30074E-06
40092.03c	91.90506	294.0	7.25478E-08	1.00839E-06	2.01006E-06
40094.03c	93.90632	294.0	7.35208E-08	1.02192E-06	2.08138E-06
40096.03c	95.90827	294.0	1.18446E-08	1.64636E-07	3.42470E-07

42092.03c	91.90682	294.0	5.97184E-05	8.30069E-04	1.65463E-03
42094.03c	93.90510	294.0	3.72235E-05	5.17396E-04	1.05378E-03
42095.03c	94.90589	294.0	6.40645E-05	8.90478E-04	1.83298E-03
42096.03c	95.90468	294.0	6.71229E-05	9.32989E-04	1.94069E-03
42097.03c	96.90602	294.0	4.00403E-05	5.56549E-04	1.16975E-03
42098.03c	97.90541	294.0	9.71026E-05	1.34970E-03	2.86605E-03
42100.03c	99.90748	294.0	3.87526E-05	5.38650E-04	1.16720E-03
73181.03c	180.94794	294.0	5.33360E-08	7.41356E-07	2.90951E-06
74182.03c	181.94813	294.0	2.80066E-08	3.89284E-07	1.53622E-06
74183.03c	182.95024	294.0	1.51927E-08	2.11174E-07	8.37940E-07
74184.03c	183.95094	294.0	3.21088E-08	4.46304E-07	1.78062E-06
74186.03c	185.95435	294.0	2.94793E-08	4.09754E-07	1.65261E-06
82206.03c	205.97443	294.0	1.68756E-08	2.34566E-07	1.04789E-06
82207.03c	206.97603	294.0	1.68610E-08	2.34363E-07	1.05208E-06
82208.03c	207.97663	294.0	3.96034E-08	5.50476E-07	2.48309E-06
83209.06c	208.98025	600.0	7.38907E-08	1.02706E-06	4.65523E-06
sum			7.19439E-02	1.00000E+00	1.00000E+00

C Process to convert CAD based geometry into STL format using FreeCAD program

A) Conversion to mesh geometry (STL) in FreeCAD:

1. Select Mesh Design Workbench.
2. Meshes -> Create mesh from shape.
3. Select shapes.
4. Mesher and meshing parameters (Netgen, Fineness: Fine) (Standard, LinDef: 0.1, AngDef: 0.25) -> OK.
5. Export the meshes by a loop:

   ```
   doc = App.getDocument("Document name")
   meshid = ["Mesh{0 : 03}".format(i) for i in range(N)]
   meshid[0] = "Mesh"
   for i,id in enumerate(meshid):
       obj = doc.getObject("Mesh"+id)
       Mesh.export([obj], ’/PATH/name’+str(i)+’.stl’)
   ```

B) Create the full module from the half module (coils):

1. Select part/mesh.
2. Make a copy of the object that will be the counterpart.
3. Rotate the counterpart: Edit -> Placement.
4. Choose Euler coordinates -> Roll = 180° -> OK.
5. Join the modules together by, e.g. rotating the original part by 72° around the z-axis.